2012-06-11

Chemical Potential Perturbation: A Method to Predict Chemical Potential Using Molecular Simulations

Stan G. Moore
Brigham Young University - Provo

Chemical Potential Perturbation: A Method to

Predict Chemical Potential Using

Molecular Simulations

Stan G. Moore

A dissertation submitted to the faculty of
Brigham Young University
in partial fulfillment of the requirements for the degree of

Doctor of Philosophy

Dean R. Wheeler, Chair
W. Vincent Wilding
Thomas A. Knotts
David O. Lignell
Kenneth A. Solen

Department of Chemical Engineering

Brigham Young University

June 2012

ABSTRACT

Chemical Potential Perturbation: A Method to
Predict Chemical Potential Using
Molecular Simulations

Stan G. Moore
Department of Chemical Engineering, BYU
Doctor of Philosophy

A new method, called chemical potential perturbation (CPP), has been developed to predict the chemical potential as a function of composition in molecular simulations. The CPP method applies a spatially varying external potential to the simulation, causing the composition to depend upon position in the simulation cell. Following equilibration, the homogeneous chemical potential as a function of composition can be determined relative to some reference state after correcting for the effects of the inhomogeneity of the system. The CPP method allows one to predict chemical potential for a wide range of composition points using a single simulation and works for dense fluids where other prediction methods become inefficient.

For pure-component systems, three different methods of approximating the inhomogeneous correction are compared. The first method uses the van der Waals density gradient theory, the second method uses the local pressure tensor, and the third method uses the Triezenberg-Zwanzig definition of surface tension. If desired, the binodal and spinodal densities of a two-phase fluid region can also be predicted by the new method. The CPP method is tested for pure-component systems using a Lennard-Jones (LJ) fluid at supercritical and subcritical conditions. The CPP method is also compared to Widom's method. In particular, the new method works well for dense fluids where Widom's method starts to fail.

The CPP method is also extended to an Ewald lattice sum treatment of intermolecular potentials. When computing the inhomogeneous correction term, one can use the Irving-Kirkwood (IK) or Harasima (H) contours of distributing the pressure. We show that the chemical potential can be approximated with the CPP method using either contour, though with the lattice sum method the H contour has much greater computational efficiency. Results are shown for the LJ fluid and extended simple point-charge (SPC/E) water. We also show preliminary results for solid systems and for a new LJ lattice sum method, which is more efficient than a full lattice sum when the average density varies only in one direction.

The CPP method is also extended to activity coefficient prediction of multi-component fluids. For multi-component systems, a separate external potential is applied to each species, and constant normal component pressure is maintained by adjusting the external field of one of the species. Preliminary results are presented for five different binary LJ mixtures. Results from the CPP method show the correct trend but some CPP results show a systematic bias, and we discuss a few possible ways to improve the method.

Keywords: surface tension, molecular dynamics, pressure tensor, inhomogeneous fluid

ACKNOWLEDGMENTS

Table of Contents

List of Tables

List of Figures

List of Symbols

Roman

a, **b**   arbitrary vectors

A Area

A, F Helmholtz energy

A, B, S, U, F, N, T, K Fourier coefficients (Chapter 6)

A, B, C, D, E, F empirical constants (Chapter 7)

B, B asymmetric force

c, k, k' influence parameter

C direct correlation function

d number of dimensions

f force

f   intermolecular force

g pure-component Gibbs energy

$g^{(2)}$ radial distribution function

h Planck's constant

h, h reciprocal lattice vectors

i	imaginary number
$\mathbf{I}$	unit tensor
k_{B}	Boltzmann's constant
K_T	isothermal bulk modulus
L	length
m	mass
n	amount of species
$N,\ N_{\mathrm{p}}$	total number of particles
N_{A}	Avogadro's number
N_{c}	number of components
P	pressure
$\mathbf{P}$	pressure tensor
q	charge
r	radius
$r_{12},\ s$	pair-wise distance
$\mathbf{r},\ \mathbf{s}$	position
S	structure factor
R_{g}	universal gas constant
t	time
T	temperature

T	isotropic tensor
u	intermolecular potential
U	energy
V	volume
$\overline{V}$	partial molar volume
x	mole fraction
x, y, z	direction
Z	canonical partition function

Greek

α	Ewald splitting constant
β	thermodynamic beta
$\beta, \theta, \nu, \gamma$	scaling exponents (Chapter 7)
γ	surface tension, activity coefficient (Chapter 5)
Γ	Fourier coefficients
δ	Dirac delta function
Δ_{ij}	periodic boundary function
ϵ	Lennard-Jones energy parameter
ε	relative error
ε_0	vacuum permittivity

ζ	entropy density
η	enthalpy density
θ	azimuthal angle
Θ	Heaviside step-function
μ	chemical potential
ρ	number density
$\rho^{(2)}$	pair correlation function
ρ_{v}, ρ_{l}	coexisting (binodal) densities
ρ_{sv}, ρ_{sl}	spinodal densities
σ	Lennard-Jones size parameter
τ	contour function
ϕ	internal energy density
2ϕ	two-phase
χ	double structure factor
ψ	Helmholtz energy density
Ω	grand potential

Subscripts

A	side A
app	apparent

avg   average

B   side B

c   critical

cut   cutoff

EOS   equation of state

f   flotsam

$i,\ j,\ k,\ n,\ m$ index variables

$i,\ j,\ \alpha,\ \beta$ species types

ijn nearest image convention

IK   Irving-Kirkwood

LJ   Lennard-Jones

max   maximum

min   minimum

N   normal

ref   reference

T   tangential

TZ   Triezenberg-Zwanzig

VdW   van der Waals

Superscripts

ex	excess of ideal mixture
ext	external
H	Harasima
ig	ideal gas
IH	inhomogeneous
int	intrinsic
IK	Irving-Kirkwood
LR	long-range
r	residual (excess of ideal gas)
recip	reciprocal space
SR	short-range
T	matrix transpose
tot	total
0	homogeneous
*	hydrostatic, LJ reduced unit

Chapter 1
Introduction

1.1 Motivation

The chemical potential is a very useful and important property. The chemical potential can be defined as a rigorous driving force toward equilibrium and is the basis of chemical fugacity and activity. It can be related to many different phenomena such as phase equilibria, transport processes such as diffusion, and chemical reaction rates [1, 2]. These phenomena are important in the design of many industrial applications, such as separation systems. Theoretical methods to predict chemical potentials are particularly useful as performing experiments involving these phenomena are often difficult, dangerous, or expensive.

The chemical potential can be related to the change in Helmholtz energy due to a change in amount of a substance while holding the system temperature T and volume V constant. This can be expressed mathematically as

$$\mu_i = \left(\frac{\partial A}{\partial n_i} \right)_{T,V,n_{j \neq i}} , \tag{1.1}$$

where A is the total Helmholtz energy of the system, μ_i is the chemical potential, and n_i is the amount of species i. Chemical potential can also be related to Gibbs energy for systems of constant pressure and temperature, but using Helmholtz energy is usually more convenient for molecular simulations as they frequently use constant volume.

Atomic-level computer simulations can be used to predict chemical potentials; however, existing methods are inefficient and may even fail for dense liquids. Several methods for

predicting chemical potentials rely on inserting particles into or removing particles from a simulation, in effect performing the derivative in Eq. 1.1 one molecule at a time. Inserted particles should not overlap with neighboring particles. However, as the density of the fluid is increased, "holes" in the fluid structure become rare, and the efficiency of insertion methods decreases. The purpose of this work is to create a better method to predict chemical potentials that doesn't require particle insertions.

1.2   Scope of work

A new method, called the *chemical potential perturbation* (CPP) method, has been developed to help overcome the limitations of existing chemical potential prediction methods. The CPP method doesn't require difficult particle insertions. Instead, a spatially varying external potential is applied to the simulation, causing the density or composition to depend upon position in the simulation cell. Because the system is allowed to equilibrate, the chemical potential (relative to some reference state) as a function of composition can then be determined from the applied field, after accounting for effects due to inhomogeneity.

Normally, homogeneous (uniform average density) simulations are used to obtain chemical potentials. However, in the CPP method, instead of performing several simulations at different densities, the CPP method allows one to predict chemical potential for a wide range of composition points using a single simulation, effectively combining many simulations into one. The CPP method also works for dense fluids and structured molecules where other prediction methods become inefficient.

In this work, the CPP method is developed for both pure-component and multi-component fluids. For pure-component fluids, the CPP method is developed for supercritical, single-phase, and two-phase (liquid-vapor) simulations. The CPP method even allows one to predict spinodal densities and properties for metastable and unstable fluid regions not easily accessible by experiment. This also provides a unique way to approach and detect the critical

point of a fluid. Preliminary results are also shown for calculating the chemical potential of solid systems.

The CPP method is further extended to long-range interactions using the lattice sum method, and the proposed methods are validated by calculating the chemical potentials of the Lennard-Jones (LJ) fluid and extended simple point-charge (SPC/E) water. A more efficient lattice sum is also developed for the LJ fluid, which has application to commonly performed simulations of vapor-liquid interfaces, surface tension, and inhomogeneous systems in general.

For multi-component systems, methods for inhomogeneous correction, fast equilibration, and correction for pressure variations are given, along with preliminary results for binary LJ mixtures. However, a full exploration of the CPP method for multi-component fluids was beyond the scope of this project.

This work focuses on the development of a new, general simulation method to predict chemical potential. This work does not focus on the development of new intermolecular potentials or the modeling of new chemical systems, but rather uses the well-characterized chemical models of the LJ fluid and water using the extended simple point-charge (SPC/E) model (for which accurate equations of state already exist) to test and validate the new method.

1.3 Outline

The remainder of this document is organized as follows.

Background. Chapter 2 is a brief description of the existing methods used to obtain chemical potentials and some inherent problems that arise when these methods are applied to dense systems.

Pure-component systems. Chapter 3 describes the development of the CPP method for pure-component systems. In order to obtain homogeneous properties from an inhomogeneous

system, it is necessary to account for the effects due to the inhomogeneity of the system, which we refer to as applying an inhomogeneous correction term. Three different methods of approximating this term are given, and results for the LJ fluid are presented and are compared to an equation of state for the LJ fluid. Parts of this chapter have been published previously in 2011 in the Journal of Chemical Physics [3].

Extension to lattice sum treatment of intermolecular potentials. Chapter 4 explains how to extend the CPP method to the lattice sum treatment of intermolecular potentials. When computing the inhomogeneous correction term, one can use two different contour functions of distributing the pressure. It is shown that both of these contours can be used with the CPP method, which allows one to obtain homogeneous properties using the lattice sum method. Results are given for the LJ fluid and SPC/E water. Preliminary results are also given for LJ solids. Parts of this chapter have been published previously in 2012 in the Journal of Chemical Physics [4].

Multi-component systems. Chapter 5 describes how to extend the CPP method to multi-component systems. Methods for inhomogeneous correction, fast equilibration, and correction for pressure variations are presented and preliminary results are given for several binary LJ mixtures.

A New Lattice Sum Method for the LJ Fluid. Chapter 6 presents a new lattice sum method for the LJ fluid which is more efficient when the average density varies only in one direction. Preliminary results are given for the LJ fluid.

Critical point prediction. Chapter 7 reviews existing methods to predict critical parameters using molecular simulations and includes some suggestions on how the CPP method could be used to predict fluid critical parameters. Preliminary results are given for the LJ fluid.

Conclusions. Chapter 8 presents the conclusions drawn from this work as well as some possible future extensions and applications of the CPP method.

Chapter 2
Background

2.1 Molecular simulations

Two types of computer simulations are commonly used to predict chemical potentials. *Molecular dynamics* (MD) simulations work by using intermolecular potentials to calculate pairwise forces between particles. Intermolecular potentials commonly have both attractive and repulsive portions. At long distances, molecules are frequently attracted to each other, while at short distances, molecules commonly repel each other, such as when two molecules collide. Using the calculated forces, the resulting accelerations and velocities are numerically integrated with respect to time (following Newton's first law) to obtain positions. Thus the individual motions of an ensemble of molecules can be predicted over time. Many properties can be predicted from MD simulations, including pressures, temperatures, diffusivities, viscosities, and chemical potentials [5, 6].

Monte-Carlo (MC) simulations work by generating likely configurations of molecules. Random configurations of molecules are generated and are accepted or rejected following the Boltzmann probability distribution based on the change in potential energy of the system. For example, if a trial move causes two molecules to significantly overlap, the move will likely be rejected due to the high increase in potential energy of the system. MC simulations can be more efficient than MD simulations in predicting equilibrium properties such as pressures, temperatures, and chemical potentials, but cannot predict time-related transport properties such as viscosities or diffusivities [5, 6]. MC simulations become less efficient as the density

of the system increases because the probability of a favorable trial move decreases. Special methods are needed to simulate large, structured molecules such as polymers using the MC method [5].

2.2 Predicting chemical potential using particle insertions

2.2.1 Free energy perturbation methods

Free energy perturbation (FEP) methods sample in one system while perturbing the system into another in order to measure a Helmholtz energy difference. For example, *Widom's* method is a simple and elegant FEP method that uses random particle insertions to calculate the chemical potential [5, 7–9]. For constant T and V and as $N \rightarrow \infty$, Eq. 1.1 is equivalent to

$$\mu_i = A_{i,N+1} - A_{i,N} \,, \tag{2.1}$$

where $A_{i,N}$ is the Helmholtz energy of species i for the N particle system and $A_{i,N+1}$ is the Helmholtz energy of the $N + 1$ system.

The chemical potential can also be partitioned into ideal gas and excess parts as

$$\mu = \mu^{\mathrm{ig}} + \mu^{\mathrm{r}} \,, \tag{2.2}$$

where μ^{ig} is the ideal gas chemical potential (which is calculated analytically or determined from experimental data) and μ^{r} is the residual chemical potential in excess of an ideal gas.

In essence, Widom's method calculates the chemical potential of a system in excess of an ideal gas by measuring the Helmholtz energy required to turn an ideal gas particle into a real particle. Particles are not actually inserted into the system, but the hypothetical energy of interaction if the particles were inserted is calculated. This information is used to generate

6

a probability distribution function for the full range of possible insertion energies, which can be used to calculate the chemical potential.

For homogeneous, pure-component NVT systems, Widom showed that

$$
\begin{aligned}
e^{-\beta\mu^{\mathrm{r}}} &= \frac{Z_{N+1}}{V\,Z_N}, \\
&= \frac{\int d\mathbf{r}^{N+1} e^{-\beta U_{N+1}}}{\int d\mathbf{r} \int d\mathbf{r}^N e^{-\beta U_N}} \\
&= \frac{\int d\mathbf{r}^N e^{-\beta U_N} e^{-\beta\Delta U}}{\int d\mathbf{r}^N e^{-\beta U_N}} \\
&= \left\langle e^{-\beta\Delta U} \right\rangle_N
\end{aligned}
\tag{2.3}
$$

where $\mathbf{r}$ is position, where $\beta = 1/(k_{\mathrm{B}}\,T)$, T is the system temperature, k_{B} is Boltzmann's constant, Z is the canonical partition function, $\triangle U$ is the hypothetical energy of insertion of a test-particle ($\triangle U = U_{N+1} - U_N$), and $\langle\ldots\rangle$ denotes the canonical average.

Because the test particles do not interact with the real particles or with each other, multiple test particles can be inserted simultaneously, and the simulation is unaffected by the insertions, so other equilibrium properties can be determined from the same simulation.

A similar but more robust FEP method is *Bennett's* method, also called the *overlapping distribution* method. This method uses random particle insertions (similar to Widom's method), as well as particle deletions [5, 10]. We note that particle deletions cannot be used alone as this leads to biased results due to inefficient sampling of the high-energy configurations [11], which in this case contribute most to the chemical potential calculation, unless special techniques [12] are used. Both Widom's and Bennett's methods become less efficient for high densities because the probability of favorable insertions (little or no overlap with neighboring particles) is low. Favorable insertions contribute most to the calculation of the chemical potential, so Widom's and Bennett's methods will not converge to an accurate result without a significant number of favorable insertions.

2.2.2   Increasing the efficiency of Widom's and Bennett's methods

Several methods have been proposed to increase the efficiency of Widom's and Bennett's methods. Particle insertions are computationally expensive because the energy of interaction between the inserted particle and all other particles in the system must be calculated. If the sampling is limited to areas where the chances of favorable insertions are high, the efficiency of the method may be increased. In essence, it may be less expensive to search for areas of favorable insertions and sample only in these locations than to randomly insert particles everywhere in the simulation.

The *cavity insertion Widom* method seeks to find holes greater than a certain radius, and then randomly inserts test particles only in those locations. As shown in Figure 2.1, to find holes and correct for the bias introduced by only sampling in the holes, the simulation cell is divided into a grid. A search for a hole is made at each grid point, and the probability of finding a hole from this search is used to correct for the bias [13, 14].
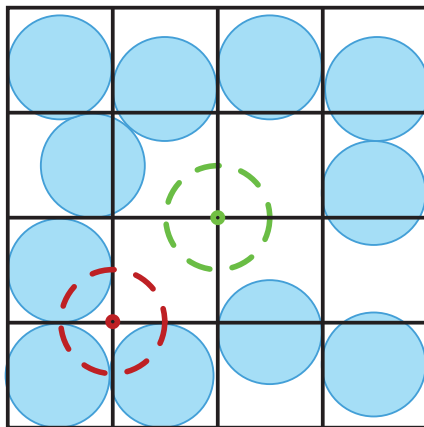
Figure 2.1: Illustration of the cavity insertion Widom method. The simulation cell is divided into a grid, and a search for a hole is made at each grid point. In this figure, a hole is found only at the center grid point.

The *excluded volume-map sampling* method excludes a certain portion of space beyond each molecule, and then samples only in the non-excluded volume region. This is also

accomplished using a grid [15, 16]. The *energy-biased* method calculates areas where the energy of insertion is below some limit, and then randomly samples only in these areas [17].

Other methods also seek to overcome the limitations of Widom's method, including staged-insertion [18], umbrella sampling [19, 20], expanded ensembles [21, 22], and histogram-distribution methods [11]. These methods can be much more efficient and accurate than Widom's method, but may likewise become less computationally efficient with structured molecules or as the density of the system is increased. Many of these methods are reviewed in Ref. [23].

2.2.3   Flotsam insertion method

Before developing the CPP method, we attempted to develop a new insertion method called the *flotsam* method. As described above, randomly inserting test particles into the simulation may be inefficient. Instead, flotsam test particles are allowed to move around in the simulation, similar to real particles. Flotsam test particles are "ghost-like" in that flotsam particles can "feel" real particles, but the real particles cannot "feel" flotsam particles. Flotsam particles also do not "feel" other flotsam particles. In this manner, the simulation is not affected by the presence of the flotsam particles and multiple flotsam particles can be inserted at the same time. This allows flotsam particles to move out of the way of real particles in order to find areas of lower potential energy (*i.e.*, holes in the simulation). For an equilibrium system, one can obtain μ^{ex} using the flotsam particles as

$$
\begin{aligned}
e^{-\beta\mu^{\mathrm{ex}}} &= \frac{\int d\mathbf{r}^{N+1} e^{-\beta\, U_N - \beta_{\mathrm{f}}\, U_{\mathrm{f}}} e^{\beta\, U_{\mathrm{f}} - \beta_{\mathrm{f}}\, \Delta U}}{\int d\mathbf{r}^{N+1} e^{-\beta\, U_N - \beta_{\mathrm{f}}\, U_{\mathrm{f}}} e^{\beta_{\mathrm{f}}\, U_{\mathrm{f}}}} \\
&= \frac{\left\langle e^{\beta_{\mathrm{f}}\, U_{\mathrm{f}} - \beta\, \Delta U} \right\rangle_{N+1}}{\left\langle e^{\beta_{\mathrm{f}}\, U_{\mathrm{f}}} \right\rangle_{N+1}} ,
\end{aligned}
\tag{2.4}
$$

where $\beta_{\mathrm{f}} = 1/\left(k_{\mathrm{B}}\, T_{\mathrm{f}}\right)$ and T_{f} is the temperature of the flotsam particles. Separate thermostats were used to control the temperatures of the real and flotsam particles.

However, some challenges were encountered with this method. First, to the flotsam particles the real particles appear to have infinite mass. Because of this, the flotsam particles experience rough dynamics when they collide with real particles, and energy and momentum are not conserved for the flotsam particles. An aggressive thermostat was necessary to remove the constantly accumulating energy of the flotsam particles. We also tried using a softer potential than the LJ potential for the flotsam interactions, which helped improve the dynamics. Another problem was that the flotsam particles tended to bunch together. We lightly tethered the flotsam particles to specific locations using a harmonic (spring-like) potential, which helped. Flotsam particles were successful in finding areas of lower energy— *i.e.*, the holes in the system. However, the main issue with the flotsam method was how to correct for the bias in the results due to non-random sampling. Eq. 2.4 didn't seem to work properly, probably because momentum wasn't conserved and constant perturbation of the flotsam particles from equilibrium makes the Boltzmann distribution inaccurate. In the end, we were unable to remove the bias in the results and the flotsam method was abandoned.

2.2.4   Thermodynamic integration method

In the *thermodynamic integration* method, a real molecule is gradually inserted into the system. This gradual insertion allows the inserted particle to push away other overlapping particles as the system is allowed to equilibrate at each step [5]. Thermodynamic integration can be used to predict chemical potentials at very high densities. However, unlike Widom's and Bennett's method, several simulations for each state point are necessary because the particle is inserted gradually, and only one particle can be inserted at a time because the inserted particle interacts with the real particles, which may cause the thermodynamic integration method to be less efficient than Widom's method.

2.2.5 Monte-Carlo methods

Two Monte-Carlo (MC) methods are directly related to this work. *Grand Canonical Monte-Carlo* (GCMC) imposes constant chemical potential, temperature, and volume on the system and measures the resulting composition [5]. The chemical potential of an ideal gas reservoir, which can be calculated analytically, is set, and the simulation cell is equilibrated with the reservoir by changing the number of molecules in the simulation cell. After equilibration, the chemical potential of the simulation cell is equal to the known chemical potential of the reservoir. In this manner, one can determine the chemical potential of the equilibrated system.

Gibbs Ensemble Monte-Carlo (GEMC) allows one to simulate phase equilibria without the formation of an interface between the two phases [5, 24, 25]. The temperature, volume, and total number of molecules of the system remain fixed, but molecules and volume are exchanged between two simulation cells. After equilibration, the chemical potentials of the two cells are equal (but the absolute value of the chemical potentials is not given by this method). For pure-component fluids, each cell contains either the liquid or vapor phase, and the coexisting densities of the fluid can be determined. Like all MC methods, GCMC and GEMC rely on particle insertions and deletions and become increasingly inefficient as the density of the system increases.

2.3 Molecular dynamics methods

An alternative to insertion-based methods is *osmotic molecular dynamics* (OMD), developed by Rowley and coworkers [26–30]. OMD uses a semi-permeable membrane to achieve chemical equilibrium between two compartments on either side of the membrane, similar to GEMC. OMD is also quite similar to the *chemical potential perturbation* (CPP) method (the topic of this dissertation), so the OMD method will be described in more detail than previous methods.
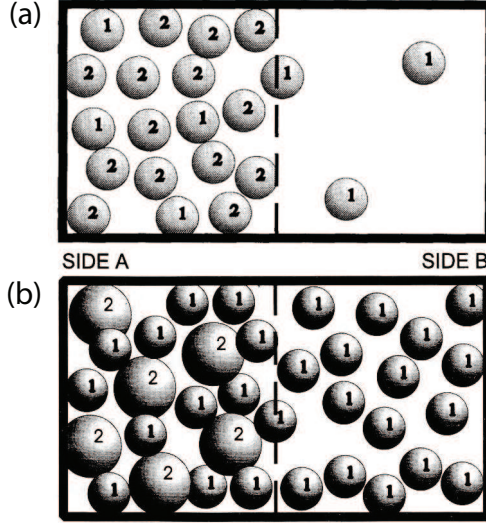
Figure 2.2: Set-up of OMD simulations for (a) pure-component and (b) multi-component systems. Type 1 molecules are allowed to pass freely through the membrane while type 2 are restricted. In (a), type 1 particles are chemically identical to type 2, while in (b) they are chemically different (from Refs. [26] and [30] with permission).

For pure-component systems, the respective compartments contain the fluid at the desired density and the same fluid at a very low density to serve as an ideal gas reference [26, 27]. As shown in Fig. 2.2a, a certain number of the particles are designated as type 1 and are allowed to freely pass through the membrane, while the other particles are designated as type 2. Type 2 particles are restricted from passing through the membrane by a Lennard-Jones potential truncated and shifted upward to include only soft, repulsive interactions. This membrane is similar to that proposed by Weeks *et al.* [31]. Side B, which includes only type 1 particles, is designated as the ideal gas side, while side A includes both type 1 and 2 particles. In this example, all the particles are chemically identical, so the residual chemical potential of the state of interest μ_1^r can be found from

$$\mu_1^r = -k_B T \ln x_{1,A} + k_B T \ln \left(\frac{\rho_B}{\rho_A} \right) , \qquad (2.5)$$

where $x_{1,A}$ is the mole fraction of type 1 particles on side A, ρ_A is the density of side A, and ρ_B is the density of side B.

12

For liquid mixtures, the respective compartments contain the mixture at the desired composition and the pure liquid as a reference [29, 30]. As shown in Figure 2.2b, to predict chemical potentials from binary LJ mixtures using OMD, type 1 particles are allowed to pass freely through the membrane, while type 2 particles (chemically different from type 1 particles) are restricted. The chemical potential (in excess of an ideal mixture) of type 1 particles on side A μ_1^{ex} is determined using the equilibrium mole fraction of type 1 particles on side A, as well as the osmotic pressure difference across the membrane. This is determined by integrating the pure-component molar volume of type 1 particles from the pressure on side A to that on side B. Mathematically, this can be expressed as

$$\mu_1^{\text{ex}} = -k_{\text{B}} T \ln x_{1,\text{A}} + \int_{P_{\text{B}}}^{P_{\text{A}}} \frac{dP}{\rho_1}, \tag{2.6}$$

where $x_{1,\text{A}}$ is the mole fraction of type 1 particles on side A, and P is the pressure. We note that for mixtures, OMD gives differences in chemical potentials in excess of an ideal mixture and not absolute values.

Close to the membrane, the structure of the fluid is affected by the membrane, so to get properties of the bulk fluid on side A, a slab that excludes the volume next to the membrane is used for density sampling. In addition, to minimize the effects of the membrane on the structure of the fluid, the simulation cell is elongated in the direction orthogonal to the membrane.

One of the main problems with the OMD method is that it is necessary to achieve equilibrium by particle diffusion, which can be very slow. However, a fast equilibrium method has been developed, which constantly applies the correct osmotic pressure by changing the volume of the cell instead of letting the system equilibrate by particle diffusion [29]. This greatly reduces the equilibration time because mechanical equilibrium is established much more quickly than diffusional chemical equilibrium.

Because no particle insertions or deletions are necessary, OMD can be used to predict chemical potentials at any reasonable density, and is also convenient for large and structured

molecules [27]. However, OMD requires a unique geometry with a membrane to predict chemical potentials (as shown in Figure 2.2), making the determination of other equilibrium properties from the same simulation more difficult because the composition of the system is not uniform and properties are position dependent and cannot simply be averaged over the entire system volume.

Similar to OMD, Powles *et al.* also used a MD simulation with a step-like external potential to create a low-density fluid pocket surrounded by a high-density fluid region [32]. The chemical potential was then measured in the low-density region using Widom's method, allowing for the prediction of the chemical potential of the high-density region after removing the effects of the external field [9].

2.4 CPP method

The *chemical potential perturbation* (CPP) method proposed here can be thought of as a generalization of OMD and the method of Powles *et al.*, which both use a step-like external potential. In contrast, the CPP method uses a finite external potential which varies periodically in one direction, matching the periodic boundary conditions of the simulation cell. Under the action of this field, the density similarly varies throughout the cell in a periodic fashion. For example, Figure 2.3a shows a snapshot of a CPP simulation produced using the VMD software program [33]. Figure 2.3b shows the external potential $U^{\text{ext}}(z)$ and resulting density profile $\rho(z)$ of this simulation *vs* position z.

In OMD, homogeneous (uniform or bulk) properties are obtained by excluding inhomogeneous portions of the simulation close to the membrane region. For the method of Powles *et al.*, no correction due to the inhomogeneity of the system was necessary because the high-density region was virtually homogeneous. However, in the CPP method, it is necessary to account for effects due to the inhomogeneity of the system to obtain homogeneous properties as described in Chapter 3.
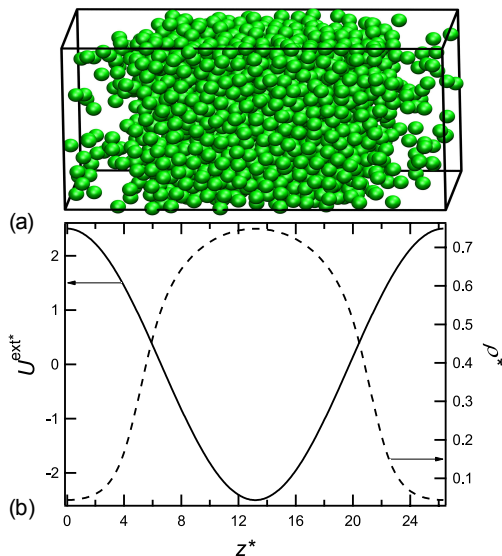
Figure 2.3: (a) Snapshot of a CPP simulation. (b) The applied external field $U^{\text{ext}}(z)$ and the resulting density profile $\rho(z)$ *vs* position z.

The CPP method is also related to GCMC and GEMC. In the CPP method, the external field and resulting density profile vary only in the z direction. Molecules in each differential slice (at some fixed z value) of the CPP simulation are naturally exchanged between neighboring slices to equilibrate the system, much like a GEMC simulation. In GCMC, the chemical potential of the system is fixed and the density of the simulation cell is measured after equilibration. In CPP, the external potential is fixed and the density at each location z is then measured after equilibration.

2.5   Conclusion

This chapter reviews current simulation methods used to predict chemical potential. Several of these methods rely on particle insertions and become increasingly inefficient for dense fluids and structured molecules. A new method called *chemical potential perturbation* (CPP) has been introduced. Some advantages of the CPP method are it predicts chemical potential differences without relying on the use of insertions and deletions, allowing the method to work at high densities where other methods fail. The CPP method also gives a whole curve

of chemical potentials corresponding to all the densities contained in the CPP simulation, in contrast to other methods that require one or more separate simulations for each state point. The following chapter describes the use of the CPP method for pure-component fluids in more detail.

Chapter 3

Pure-component systems

3.1 Introduction

In this chapter, we develop the CPP method for pure-component systems and present results for the Lennard-Jones fluid at vapor, liquid, two-phase, and supercritical conditions.

When one performs an inhomogeneous molecular simulation, it is normally with the intention to obtain phase equilibria properties such as coexisting liquid-vapor densities or interfacial properties such as surface tension. In contrast, with CPP a single inhomogeneous simulation is used to obtain homogeneous (uniform or bulk) properties for the whole range of densities found in the inhomogeneous simulation. Homogeneous properties (denoted with a superscript 0) mean properties that would be given in an uniform density equilibrium simulation or by an equation of state. A simulated fluid may be inhomogeneous due to spontaneous phase splitting, or may be inhomogeneous due to the effects of an external potential acting on the system, or both. In any case, it is necessary to correct for the effects resulting from the inhomogeneity of the system to obtain homogeneous properties.

According to concepts found in density functional theory [34], one can divide the properties of inhomogeneous fluids into both local and nonlocal terms. Local, or homogeneous, terms depend only on the condition of the fluid at position $\mathbf{r}$ in the simulation cell. Because molecules interact over a finite distance, however, the condition at one location affects that of other locations. Nonlocal, or inhomogeneous, terms capture this effect and depend upon the condition of the fluid in the vicinity of position $\mathbf{r}$. For example, surface tension is a

manifestation of nonlocal effects. We describe below how to obtain homogeneous properties using three different methods.

3.2 Van der Waals density gradient theory

Van der Waals (VdW) developed a density gradient theory that can be used to predict the surface tension and density profile of an inhomogeneous fluid if the density profile is sufficiently slowly varying [35–37]. Van der Waals proposed that the local Helmholtz energy density consists of two terms: the homogeneous Helmholtz energy density and the inhomogeneous Helmholtz energy density, which depends on the density gradient squared. This theory was later rediscovered by Cahn and Hilliard [38], and Yang *et al.* obtained a similar result from a rigorous expansion in powers of density derivatives [39].

Using density gradient theory, an analytical equation of state can be used to predict the surface tension and density profile of an inhomogeneous fluid [36, 40]. In other words, information about a homogeneous system is used to predict inhomogeneous or interfacial properties. In the CPP method, the reverse is used: the density profile and other information pertaining to a simulated inhomogeneous system is used to obtain homogeneous properties.

We follow the work of Yang *et al.* and define the total Helmholtz energy F^{tot} of the system as the volume integral of the Helmholtz energy density $\psi^{\text{tot}}(\mathbf{r})$, or

$$F^{\text{tot}} = \int \psi^{\text{tot}}(\mathbf{r}) \, d\mathbf{r} \,. \tag{3.1}$$

For an inhomogeneous system with an external potential $U^{\text{ext}}(\mathbf{r})$, the Helmholtz energy density can be partitioned into multiple contributions:

$$\psi^{\text{tot}}(\mathbf{r}) = U^{\text{ext}}(\mathbf{r}) \, \rho(\mathbf{r}) + \psi^{0}(\mathbf{r}) + \psi^{\text{IH}}(\mathbf{r}) \,, \tag{3.2}$$

where ρ is the molecular number density. ψ^0 is the Helmholtz energy density of a homogeneous fluid with temperature and density the same as the inhomogeneous fluid at position $\mathbf{r}$ and is a local term. ψ^{IH} is the excess Helmholtz energy density due to the inhomogeneity of the system and is a nonlocal term. Throughout this work we assume the density varies only in the z direction. Eq. 3.2 then becomes

$$\psi^{\mathrm{tot}}(z) = U^{\mathrm{ext}}(z)\,\rho(z) + \psi^0(z) + \psi^{\mathrm{IH}}(z)\,. \tag{3.3}$$

Yang *et al.* rigorously showed that a density gradient term can be used to approximate $\psi^{\mathrm{IH}}(\mathbf{r})$ as

$$\psi^{\mathrm{IH}}(z) = \frac{1}{2}c(\rho)\,\rho'(z)^2 + \mathcal{O}\left(\nabla^4 \rho\right)\,, \tag{3.4}$$

where $\rho'(z) = d\rho/dz$ and $c(\rho)$ is called the influence parameter and is given as

$$c\left(\rho\right) = \frac{2}{3}\pi\,k_{\mathrm{B}}\,T \int dr_{12}\,r_{12}^4\,C^0(r_{12}, \rho)\,, \tag{3.5}$$

where r_{12} is the molecular pair-wise distance and $C^0(r_{12}, \rho)$ is the direct correlation function of a homogeneous fluid. The influence parameter c may be also taken to be an empirical constant (independent of temperature and density) [40], as is the case in this chapter unless otherwise noted. In Eq. 3.4, the notation $\mathcal{O}\left(\nabla^4\rho\right)$ refers to the order of the truncation error, meaning that the neglected terms are proportional to products of density derivatives whose orders sum to 4 or greater. We include this term as a reminder that higher order terms have been neglected in gradient theory.

Eqs. 3.2 and 3.3 do not necessarily describe a system at equilibrium. If we assume equilibrium, then F^{tot} will be minimized subject to the constraints of constant volume V and a fixed number of molecules N. One can use the solution to the Euler-Lagrange equation to minimize F^{tot} with these constraints [39]. This leads to

$$\mu^{\text{tot}} = U^{\text{ext}}(z) + \mu^0(z) + \mu^{\text{IH}}(z), \tag{3.6}$$

where μ^{tot} is the total chemical potential, which is constant at all locations inside the simulation cell. μ^0 is the desired homogeneous chemical potential, and μ^{IH} is the inhomogeneous chemical potential. The intrinsic chemical potential μ^{int} is defined as $\mu^{\text{int}}(z) = \mu^0(z) + \mu^{\text{IH}}(z)$. We note that Widom's method when applied to an inhomogeneous system gives μ^{int}, not μ^0 [9, 37].

Using the Euler-Lagrange equation and the approximation for ψ^{IH} given in Eqs. 3.4 and 3.5 gives [39]

$$\mu^{\text{IH}}(z) = -\frac{1}{2}\frac{\partial c(\rho)}{\partial \rho}\,\rho'(z)^2 - c(\rho)\,\rho''(z) + \mathcal{O}\left(\nabla^4 \rho\right), \tag{3.7}$$

where $\rho''(z) = d^2\rho/dz^2$.

Rearranging Eq. 3.6 yields

$$\mu^0(z) = -U^{\text{ext}}(z) - \mu^{\text{IH}}(z) + \mu^{\text{tot}}. \tag{3.8}$$

In the CPP method, U^{ext} is fixed. Given $\mu^{\text{IH}}(z)$ and μ^{tot}, the desired $\mu^0(z)$ curve can be obtained for the entire range of densities found in the simulation. In this work, the combination of Eqs. 3.7 and 3.8 with c taken to be an empirical constant constitute the *VdW method*. Methods of obtaining μ^{tot} and $\mu^{\text{IH}}(z)$ are given below.

For pure-component systems at constant temperature [37], the homogeneous Helmholtz energy density is

$$\psi^0(\rho) = \int \mu^0(\rho)\,d\rho - P^*, \tag{3.9}$$

where P^* is a constant of integration. In the absence of an external field, P^* is equal to the hydrostatic pressure of the system. If desired, the Helmholtz energy density ψ^0 can be

obtained from the VdW method by multiplying Eq. 3.8 by $d\rho/dz$ according to Eq. 3.9 and integrating with respect to z:

$$
\begin{aligned}
\psi^0(z) &= -\int U^{\text{ext}}(z)\frac{d\rho(z)}{dz}dz + \psi^{\text{IH}}(z) + \mu^{\text{tot}}\,\rho(z) \\
&\quad - P^* + \mathcal{O}\left(\nabla^4\rho\right),
\end{aligned} \tag{3.10}
$$

where we have used Eqs. 3.4 and 3.7 as well. From the relationship between Gibbs and Helmholtz energies, the homogeneous pressure P^0 of a pure-component fluid can be defined as

$$
P^0(z) = \mu^0(z)\,\rho(z) - \psi^0(z). \tag{3.11}
$$

The system constants μ^{tot} and P^* can be determined in two ways. First, if the density is low enough at some position in the CPP simulation, they can be determined from the ideal gas chemical potential and pressure. Otherwise, an additional homogeneous simulation using Widom's method or an equation of state (EOS) can be used to determine the chemical potential and pressure at one density found in the CPP simulation. Alternatively, one could determine μ^{tot} by performing Widom insertions at one location in the CPP simulation (generally the planar slice with the lowest density).

In summary, $\mu^0(\rho)$ is obtained using the VdW method as follows:

1. Run an NVT simulation with $U^{\text{ext}}(z)$ to measure the resulting $\rho(z)$

2. Approximate $\mu^{\text{IH}}(z)$ using Eq. 3.7 with c taken to be an empirical constant

3. Determine μ^{tot} as described above

4. Obtain $\mu^0(z)$ using Eq. 3.8

5. Plot $\mu^0(z)$ *vs* $\rho(z)$ to obtain the desired $\mu^0(\rho)$

3.3 Pressure tensor method

In this section, we describe how to calculate the inhomogeneous pressure tensor $\mathbf{P}(z)$ using the virial equation and show how to approximate corresponding homogeneous properties.

3.3.1 Calculation of the pressure tensor

In this work, we assume an inhomogeneous system confined to a rectangular box in which average fluid properties vary only in the z direction. Assuming thermal equilibrium, the local pressure tensor $\mathbf{P}(z)$ can be expressed as [41]

$$\mathbf{P}(z) = k_{\mathrm{B}} \, T \, \rho(z) \, \mathbf{I} + \frac{1}{V} \sum_i \sum_{j<i} \mathbf{f}_{ijn} \, \mathbf{r}_{ijn}^{\mathrm{T}} \tau_{ijn}(z) \,, \tag{3.12}$$

where k_{B} is Boltzmann's constant, T is the system temperature, $\rho(z)$ is the density at position z, $\mathbf{I}$ is the identity matrix, V is the system volume, the notation ijn means that the nearest-image convention is used in conjunction with periodic boundary conditions between molecules i and j, $\mathbf{r}_{ijn}$ is the molecular pair-wise distance, and $\mathbf{f}_{ijn}$ is the intermolecular force. The superscript T refers to the matrix transpose, in this case turning a column vector into a row vector (*i.e.* Eq. 3.12 contains the outer product of two vectors). The double sum is over all unique molecular pairs in the system subject to a spherical cutoff based on distance $\mathbf{r}_{ijn}$. For our equilibrium system, there are two independent components of the pressure tensor: one normal to the interface, $P_{\mathrm{N}}(z) = P_{zz}(z)$, and one tangential to the interface, $P_{\mathrm{T}}(z) = P_{xx}(z) = P_{yy}(z)$.

$\tau_{ijn}(z)$ is the contour function that controls how the pressure is distributed spatially with respect to each interacting pair of molecules. The pressure tensor has a well known ambiguity on this issue. As stated by Schofield and Henderson, for a planar interface, the tangential component of the pressure is not uniquely defined, so one can express the non-unique nature of the tangential component of the pressure tensor in terms of a contour connecting the two interacting molecules [42]. In essence one must decide how to spatially distribute the
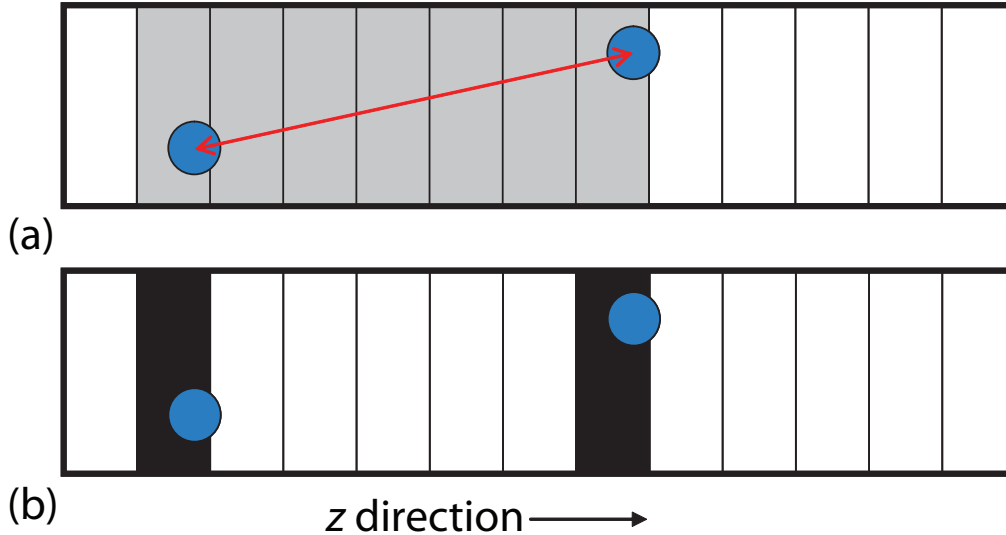
Figure 3.1: Conceptual representation of (a) the IK contour and (b) the H contour showing how pairwise contributions to pressure are spatially distributed.

contribution to the pressure, energy, *etc.* due to a pair of interacting molecules. The contours given by Irving and Kirkwood (IK) [41] and Harasima (H) [43] (see also Ref. [44]), are most commonly used. The IK contour distributes the pair-wise contribution uniformly along a straight line connecting the interacting pair of molecules (in the nearest-image sense), while the H contour distributes the pair-wise contribution equally between the two point locations of the molecules of the interacting pair. In practice, the pressure is calculated with the IK or H contour using a finite number of slabs normal to the z direction as shown in Figure 3.1. Some properties depend on choice of contour and others do not. For example, the total amount of surface tension is independent of contour, but how the predicted surface tension is distributed locally throughout the interface is affected by which contour is used. In contrast, the normal component of the pressure tensor is well-defined (to within a constant) as given by mechanical equilibrium [42] as described below.

In this chapter, we use the IK contour which, as stated above, distributes the pairwise pressure uniformly along a straight line connecting the interacting pair of molecules. There are multiple ways to express this mathematically [45, 46], and in many works periodic

boundary conditions are neglected. In order to account for the periodic boundary conditions of the system, we use

$$\tau_{ijn}^{\mathrm{IK}}(z) = \frac{L_z}{z_{ijn}} \left[\Theta\left(z - z_i\right) - \Theta\left(z - z_j\right) \right] + \frac{\Delta_{ij}}{z_{ijn}}, \tag{3.13}$$

where Θ is the Heaviside step function, L_z is the length in the z direction,

$$\Delta_{ij} = -L_z \operatorname{trunc}\left[2\left(z_j - z_i\right)/L_z \right], \tag{3.14}$$

where $\operatorname{trunc}(x)$ is the truncation function that removes the fractional part of x, and

$$z_{ijn} = z_j - z_i + \Delta_{ij}. \tag{3.15}$$

In practice, $\mathbf{P}(z)$ is calculated with the IK contour using a finite number of slabs normal to the z direction. The N_{s} slabs that contain any part of the line connecting the two molecular centers of mass are determined, and each of these slabs is assigned $1/N_{\mathrm{s}}$ of the total contribution of pressure from a given pair interaction. (For example, see Ref. [47].)

3.3.2 Restrictions on the normal pressure

For a fluid at equilibrium, mechanical stability introduces a restriction on the normal pressure. In the case of our system,

$$\frac{dP_{\mathrm{N}}(z)}{dz} = \rho(z)\, f^{\mathrm{ext}}(z), \tag{3.16}$$

where $f^{\mathrm{ext}}(z) = -dU^{\mathrm{ext}}(z)/dz$ is the external force acting on the particles in the system [37].

Eq. 3.16 can be integrated to obtain

$$P_{\mathrm{N}}(z) = \int \rho(z)\, f^{\mathrm{ext}}(z)\, dz + P^*. \tag{3.17}$$

For a system at equilibrium, ψ^0 is given by Eq. 3.10. We can eliminate the integral in Eq. 3.10 using integration by parts with the help of Eq. 3.17, giving

$$
\begin{aligned}
\psi^0(z) \;=\;& -U^{\text{ext}}(z)\,\rho(z) - P_{\text{N}}(z) + \psi^{\text{IH}}(z) \\
& +\mu^{\text{tot}}\,\rho(z) \,+\, \mathcal{O}\left(\nabla^4\rho\right)\,.
\end{aligned}
\tag{3.18}
$$

Combining Eqs. 3.8, 3.11, and 3.18 and rearranging yields

$$
P_{\text{N}}(z) = P^0(z) + \psi^{\text{IH}}(z) + \mu^{\text{IH}}(z)\,\rho(z) \,+\, \mathcal{O}\left(\nabla^4\rho\right).
\tag{3.19}
$$

Like Eq. 3.16, Eq. 3.19 can also be used to verify that the system is at mechanical equilibrium.

3.3.3   Obtaining homogeneous properties

One can expand the local pressure tensor (Eq. 3.12) using a Taylor series in density gradient to obtain a combination of homogeneous and inhomogeneous terms. This allows one to obtain an expression for the homogeneous pressure using a linear combination of P_{N} and P_{T}. Such an expansion using the IK contour predicts that [34, 48, 49]

$$
P_{\text{N}}^{\text{IK}}(z) = P^0(z) + k\left[\tfrac{1}{2}\rho'(z)^2 - \rho''(z)\,\rho(z)\right] + \mathcal{O}\left(\nabla^4\rho\right)\,,
\tag{3.20}
$$

and

$$
P_{\text{T}}^{\text{IK}}(z) = P^0(z) + \tfrac{1}{3}k\left[\tfrac{1}{2}\rho'(z)^2 - \rho''(z)\,\rho(z)\right] + \mathcal{O}\left(\nabla^4\rho\right)\,,
\tag{3.21}
$$

where k is the influence parameter and is a system constant equal to

$$
k = \tfrac{1}{30}\int s^3 u'(s)\,g^{(2)}\left(s,\rho_{\text{avg}}\right)\,d\mathbf{s}\,,
\tag{3.22}
$$

where s is the molecular pair-wise distance, $-u'(s)$ is the intermolecular force, and $g^{(2)}(s, \rho_{\text{avg}})$ is the radial distribution function of the homogeneous fluid at the average density ρ_{avg} of the system. k can be calculated from c (Eq. 3.5) used in VdW gradient theory with the use of certain approximations [34].

In gradient theory, other approximations can also used for k. Some assume that k depends only on the intermolecular potential and not on the structure of the fluid, while others use the direct correlation function of the homogeneous fluid at the local density [34, 37]. Some even assume that k is independent of density and temperature [40]. Furthermore, the calculation of k in Eq. 3.22 assumes a spherically symmetric force, which is usually not the case for structured molecules. (For non-spherical molecules, one can average over all orientations of the molecule.) However, in the CPP method, this point is less important because the constant k is never actually calculated. One can eliminate k by combining Eqs. 3.20 and 3.21 and solving for $P^0(z)$:

$$P^0(z) = \tfrac{3}{2} P_{\text{T}}(z) - \tfrac{1}{2} P_{\text{N}}(z) + \mathcal{O}\left(\nabla^4 \rho\right) . \tag{3.23}$$

Eq. 3.23 allows one to relate an inhomogeneous system to a homogeneous one and even allows one to predict spinodal densities of a fluid [50, 51].

If $U^{\text{ext}}(z) = 0$, then P_{N} is constant at all locations in the system, even if there are two phases and an interface present, as shown by Eq. 3.16. The chemical potential μ^{int} given by Widom's method is also constant in the absence of an external field as shown by Eq. 3.6. However, if two phases are present, P_{T}, P^0, and μ^0 may vary throughout the interface, and P^0 and μ^0 will furthermore exhibit a van der Waals loop.

Once we have determined P^0, we can obtain the homogeneous chemical potential μ^0 using the definition of Gibbs energy (at constant temperature):

$$\mu^0(z) = \int \frac{dP^0(z)}{dz} \frac{1}{\rho(z)} dz + \mu^{\text{tot}} , \tag{3.24}$$

where the constant μ^{tot} is the total chemical potential. We refer to the use of Eqs. 3.23 and 3.24 as the *pressure tensor method* of obtaining μ^0. If desired, the Helmholtz energy density can be obtained from the pressure tensor method by rearranging Eq. 3.11.

In summary, $\mu^0(\rho)$ is obtained using the pressure tensor method as follows:

1. Run an NVT simulation with $U^{\text{ext}}(z)$ to measure the resulting $\rho(z)$, $P_{\text{N}}(z)$, and $P_{\text{T}}(z)$

2. Obtain $P^0(z)$ using Eq. 3.23

3. Determine μ^{tot} as described above

4. Obtain $\mu^0(z)$ using Eq. 3.24

5. Plot $\mu^0(z)$ *vs* $\rho(z)$ to obtain the desired $\mu^0(\rho)$

3.4   TZ method

Here we show a third method to obtain homogeneous properties using a relation between the surface tension γ and ψ^{IH}. Working equations for surface tension often include a factor of $1/2$ to account for the fact that two interfaces are formed in periodic molecular simulations. However, for simplicity, the equations in this section assume a single interface. For a non-periodic system, the integrals over system length range between $\pm\infty$, and for a periodic system, they range between 0 and L_z.

3.4.1   Surface tension

The surface tension is related to the pressure tensor according to [41]

$$\gamma = \int \left[P_{\text{N}}(z) - P_{\text{T}}(z)\right] dz\,. \tag{3.25}$$

The total grand potential Ω^{tot} can be defined as

$$\Omega^{\text{tot}} = A \int \left[\psi^{\text{tot}}(z) - \mu^{\text{tot}} \rho(z) \right] dz \,. \tag{3.26}$$

Ω^{tot} is also related to P_{T} as [52, 53]

$$\Omega^{\text{tot}} = -A \int P_{\text{T}}(z) dz \,. \tag{3.27}$$

Combining Eqs. 3.25-3.27 gives

$$\gamma = \int \left[P_{\text{N}}(z) - \psi^{\text{tot}}(z) - \mu^{\text{tot}} \rho(z) \right] dz \,. \tag{3.28}$$

Combining Eqs. 3.3, 3.18, and 3.28 gives

$$\gamma = 2 \int \psi^{\text{IH}}(z) \, dz + \mathcal{O}\left(\nabla^4 \rho\right) . \tag{3.29}$$

Eq. 3.29 can also be derived in a more familiar manner for a system without an external potential [34, 39]. Combining Eqs. 3.1, 3.3, and 3.18 gives

$$F^{\text{tot}} = 2A \int \psi^{\text{IH}}(z) \, dz - PV + \mu^{\text{tot}} N + \mathcal{O}\left(\nabla^4 \rho\right) . \tag{3.30}$$

A definition of surface tension in the absence of an external potential is

$$\gamma = \left(\frac{\partial F^{\text{tot}}}{\partial A} \right)_{T,N,V} . \tag{3.31}$$

Combining Eqs. 3.30 and 3.31 gives Eq. 3.29.

3.4.2 Obtaining homogeneous properties

It is tempting to assume that the integrands in Eqs. 3.28 and 3.29 are equal locally, allowing one to obtain $2\psi^{\text{IH}}(z)$ from $P_{\text{N}}(z) - P_{\text{T}}(z)$. This is true of the form of the pressure tensor first proposed by Lovett [39, 54, 55]. Lovett's form furthermore satisfies the mechanical stability

restriction placed on P_{N} given in Eq. 3.19. However, no contour (such as the IK contour given in Eq. 3.13) or virial-type expression was given to calculate this form of $\mathbf{P}(\mathbf{r})$ in a discrete-particle system. Simulations show that the integrands in Eqs. 3.28 and 3.29 are not equal locally for the IK pressure tensor (see Fig. 3.5 below). This is because $P_{\mathrm{N}}(z) - P_{\mathrm{T}}(z)$ calculated using the IK contour and $2\psi^{\mathrm{IH}}(z)$ differ by some function that integrates to zero over the length of the system in the z direction.

Another expression for γ was obtained by Triezenberg and Zwanzig [56] (TZ). (See also Ref. [57] for an independent derivation.) For our system,

$$\gamma = \frac{1}{2}\pi \, k_{\mathrm{B}} \, T \int dz \, \rho'(z) \int dz_2 \, \rho'(z_2) \int ds \, s^3 \, C(z, z_2, s) \ , \tag{3.32}$$

where $s = \sqrt{x_{12}^2 + y_{12}^2}$ and $C(z, z_2, s)$ is the inhomogeneous direct correlation function.

Combining Eqs. 3.29 and 3.32 without integrating over dz yields

$$
\begin{aligned}
\psi^{\mathrm{IH}}(z) \;=\; & \frac{1}{4}\pi \, k_{\mathrm{B}} \, T \, \rho'(z) \int dz_2 \, \rho'(z_2) \int ds \, s^3 \, C(z, z_2, s) \\
+ \; & \Delta_{\mathrm{TZ}}(z) + \mathcal{O}\left(\nabla^4 \rho\right) \ ,
\end{aligned}
\tag{3.33}
$$

where $\int \Delta_{\mathrm{TZ}}(z)\, dz = 0$.

The expressions for ψ^{IH} given by Eq. 3.33 and the VdW method are closely related: If we approximate $C(z, z_2, s)$ as the homogeneous direct correlation function $C^0(r_{12}, \rho(z))$ and expand $\rho'(z_2)$ around $\rho'(z)$ using a Taylor series, then the resulting first term of the series is equal to Eq. 3.4 with $c(\rho)$ given by Eq. 3.5 [37, 58]. Furthermore, with these approximations, $\Delta_{\mathrm{TZ}}(z) = \mathcal{O}(\nabla^4\rho)$. As a practical matter, we assume $\Delta_{\mathrm{TZ}}(z) = 0$ in Eq. 3.33. Simulation results (below) confirm this as reasonable.

The use of Eq. 3.33 requires the inhomogeneous direct correlation function. Obtaining inhomogeneous direct correlation functions directly from simulations [59–61] and integral

equation theory [62, 63] has been discussed previously, but this was beyond the scope of this project.

Instead, we used the homogeneous direct correlation function at an average density to approximate the inhomogeneous direct correlation function as

$$C(z_1, z_2, s) = C^0(r_{12}, \bar{\rho}) , \tag{3.34}$$

where $\bar{\rho} = [\rho(z_1) + \rho(z_2)]/2$. This approximation has been used previously for the LJ fluid [64].

We furthermore estimated the homogeneous direct correlation function using the homogeneous Ornstein-Zernicke (OZ) equation [65] with the Percus-Yevick (PY) closure relation [66]. A solution was effected by the method of Gillian [67] and a computer code adapted from Lee [68] with a grid spacing of $\triangle \rho^* = 0.01$ and $\triangle r^* = 0.05$ (quantities defined below). The double integral in Eq. 3.33 was evaluated numerically for 250 points in the z direction. The ψ^{IH} values at these points were then fit vs density using a polynomial with 15 coefficients.

Given ψ^{IH} from Eq. 3.33 and the approximation in Eq. 3.34, one can calculate ψ^0 using Eq. 3.18 and μ^0 using Eq. 3.9. We refer to this as the *TZ method* of obtaining μ^0. If desired, one can use the TZ method to calculate P^0 using Eq. 3.11.

In summary, $\mu^0(\rho)$ is obtained using the TZ method as follows:

1. Run an NVT simulation with $U^{\text{ext}}(z)$ to measure the resulting $\rho(z)$ and $P_{\text{N}}(z)$

2. Approximate $\psi^{\text{IH}}(z)$ using Eqs. 3.33 and 3.34

3. Determine μ^{tot} as described above

4. Calculate ψ^0 using Eq. 3.18

5. Obtain $\mu^0(z)$ using Eq. 3.9

6. Plot $\mu^0(z)$ vs $\rho(z)$ to obtain the desired $\mu^0(\rho)$

3.5 Long-range corrections

When simulating homogeneous systems of Lennard Jones (LJ) particles using MD simulations, the intermolecular force is usually truncated at some radial distance r_{cut}, and standard long-range corrections (LRCs), which assume the radial distribution function is unity for $r \geq r_{\text{cut}}$, are applied to the energy and pressure terms at the end of the simulation [69]. For a homogeneous or isotropic system, long-range forces cancel by symmetry, so there is no LRC applied to the forces in this case.

However, for an inhomogeneous simulation, the corrections of energy, force, and pressure tensor are nonlocal terms which depend on the condition of the surrounding fluid. Long-range forces no longer cancel, and a correction to the forces may need be applied at every timestep to obtain the correct density profile. For homogeneous LJ simulations, $r_{\text{cut}} = 2.5\sigma$ is considered reasonable, where σ is the LJ distance parameter. However, the phase behavior, including the critical point, of an inhomogeneous LJ fluid depends highly upon the cutoff distance (at least for $r_{\text{cut}} < 5.5\sigma$) if proper long-range corrections are neglected [70].

In this work, we use $r_{\text{cut}} = 5.5\sigma$ to account for the inhomogeneity of the system. To account for interactions beyond this cutoff, a local standard homogeneous LRC to pressure [71], evaluated at $\rho(z)$, is also applied to $P^0(z)$. More accurate alternatives exist and are described in Chapters 4 and 5.

3.6 Simulation details

In order to test the results of the proposed methods, we selected and simulated supercritical, two-phase, vapor, and liquid conditions for a pure-component Lennard-Jones (LJ) fluid. We use the LJ fluid because accurate equations of state exist for this fluid [72, 73] which can be used to validate results from the CPP method. Additionally, the LJ fluid is computationally efficient and simple to implement, yet contains essential physics for a nonpolar spherical molecule and is well-accepted as a benchmark system. The LJ potential $u_{\text{LJ}}(r)$ is given as

$$u_{\text{LJ}}(r) = 4\,\varepsilon \left[\left(\frac{\sigma}{r} \right)^{12} - \left(\frac{\sigma}{r} \right)^{6} \right] , \tag{3.35}$$

where ε and σ are the respective LJ energy and distance parameters. Results in this chapter are given in reduced LJ units as $z^* = z/\sigma$, $T^* = k_{\text{B}}\,T/\varepsilon$, $\rho^* = \rho\,\sigma^3$, $\psi^* = \psi\,\sigma^3/\varepsilon$, $\gamma^* = \gamma\,\sigma^2/\varepsilon$, $\mu^* = \mu/\varepsilon$, $c^* = c/\left(\varepsilon\,\sigma^5\right)$ and $t^* = t/\sqrt{\sigma^2\,m/\varepsilon}$, where m is the particle mass.

The molecular dynamics method was used. The equations of motion included an integral-control (Nosé-Hoover) thermostat and were integrated using a 4th-order Gear predictor-corrector scheme [69]. The size of the time step was selected for each simulation to generate a root-mean-square displacement of molecules of 0.003σ per timestep. A Verlet neighbor list was used to speed up computations [69].

The external potential was of the following form consistent with periodic boundary conditions:

$$U^{\text{ext}}(z) = \frac{\triangle U_{\text{max}}}{2} \, \cos \left(\frac{2\pi\,z}{L_z} \right) , \tag{3.36}$$

where $\triangle U_{\text{max}}$ is an adjustable parameter corresponding to the maximum difference in external potential. $\triangle U_{\text{max}}$ also corresponds to maximum difference in μ^{int} as shown by Eq. 3.6. Changing $\triangle U_{\text{max}}$ and the average density of the system ρ_{avg} allows one to control the range of densities obtained in a CPP simulation. In this work, we used an iterative process or an equation of state to determine $\triangle U_{\text{max}}$ and ρ_{avg} which give a desired range of densities. Though not done here, one could use an NPT ensemble to control the average density of the system and a feedback control system for the external field to achieve a desired density profile.

The CPP method applies a continuous, spatially varying external field to the system. This causes a continuous change in the density profile. Therefore, the CPP method essentially gives the density profile and resulting chemical potential as continuous curves. Any discretization used is for convenience in post-processing the results. Samples for density and
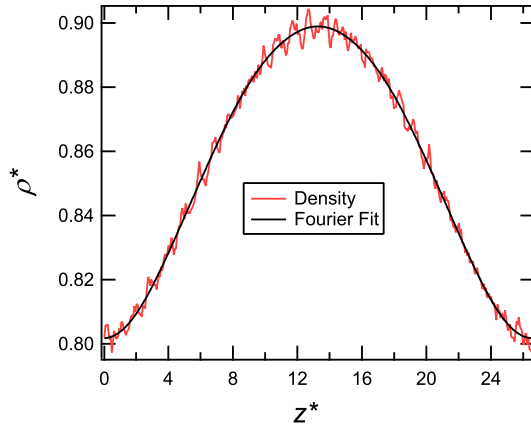
Figure 3.2: An example of a Fourier fit used to smooth the density profile.

pressure profiles were taken every 8 timesteps and were collected using 401 equally spaced slabs normal to the z direction.

Resulting pressure and density profiles were each fit using a Fourier cosine series, as this automatically satisfies the periodicity and symmetry of the system. Additionally, limiting the number of terms in the Fourier cosine series worked well to screen out noise and smooth the data. Figure 3.2 shows an example of a Fourier cosine series used to fit the data. Using too few Fourier coefficients results in a poor fit of the data or oscillations near sharp changes in the profiles (such as the change in density at an interface between two phases), which biases the results. Using too many Fourier coefficients increases the random noise in the results. Using both a slab-based histogram and a Fourier fit allowed us to check the reasonableness of the fit while smoothing out random error. In order to check that our results were independent of the number of slabs used, we increased the number of slabs from 401 to 701 for the CPP 2 and 3L simulations (described below). These simulations contain relatively sharp changes in density profile, and yet increasing the number of slabs did not significantly alter the $\mu^0(z)$ curves.

When assessing the results of a method, it is important to consider both random errors and systematic bias. Sources of random errors in the CPP method include noise in the measured density and pressure tensor profiles. Sources of biases in the CPP method include

33

truncation errors in the Fourier series used to fit the profiles and truncation errors in the Taylor series expansions used to approximate μ^{IH}.

Random errors were estimated using the block method. Each simulation was divided into 10 blocks, which were used to calculate 95% confidence intervals of the data using the Student's t-distribution. In the CPP method, both the measured density and chemical potential vary at a given position. The variation in chemical potential is due to the correction for the inhomogeneity of the system. Thus a plot of μ vs ρ requires error bars in both directions. We plotted these error bars for several points along the curves in order to give the reader a sense of the random errors in the simulations.

In order to estimate the bias in the CPP method, we used an equation of state (EOS) for the LJ fluid proposed by Kolafa and Nezbeda [72], as well as Widom's method (see Eq. 2.3). This LJ EOS and Widom's method both give the chemical potential in excess of an ideal gas. In order to obtain the full chemical potential, it is necessary to include the ideal gas chemical potential μ^{ig} given in reduced LJ units as

$$\mu^{\mathrm{ig}\,*}(z) = T^* \ln\left[\left(\frac{h^{*\,2}}{2\,\pi\,T^*}\right)^{3/2} \rho^*(z)\right], \tag{3.37}$$

where $h^* = h/\sqrt{\sigma^2 \varepsilon\, m}$ and h is Planck's constant. For purposes of presentation we used $h^* = 0.183$, obtained by using typical LJ parameters for argon: $\varepsilon/k_{\mathrm{B}} = 121.85\,\mathrm{K}$, $\sigma = 0.3429\,\mathrm{nm}$, and $m\,N_{\mathrm{A}} = 39.948\,\mathrm{g/mol}$, where N_{A} is Avogadro's number.

The CPP method gives differences in chemical potentials as a function of density. Another method such as Widom's or an EOS is needed to determine the unknown constant (or reference) μ^{tot}. In this work, μ^{tot} was determined by shifting the $\mu^0(z)$ curve vertically until it matched the LJ EOS at ρ_{avg} (unless otherwise noted). Because μ^0 is fixed at this point, the apparent error at this point will be zero. Alternatively, we could have determined μ^{tot} by performing Widom insertions in one slice of the CPP simulation or in a separate homogeneous simulation at one density contained in the CPP simulation. It was not necessary to determine P^* because the IK method was used to calculate the pressure tensor.

Table 3.1: Parameters for the pure-component CPP fluid simulations shown in this chapter. Type SC refers to supercritical, 2ϕ refers to two-phase, Vap refers to vapor, and Liq refers to liquid.

Name	Type	N	$\frac{L_z}{L_x = L_y}$	T^*	$\rho^*_{\min}$	ρ^*_{avg}	$\rho^*_{\max}$	$\triangle U^*_{\max}$	timesteps
1	SC	2×10^3	2	1.5	0.043	0.437	0.749	5.0	5×10^6
1L	SC	10^4	10	1.5	0.044	0.437	0.751	5.0	10^6
2	SC	4×10^3	4	2.0	0.011	0.632	1.05	28.5	10^6
3	2ϕ	10^3	1	0.8	0.00168	0.403	0.847	2.0	2×10^6
3L	2ϕ	4×10^3	4	0.8	0.00149	0.403	0.848	2.0	2×10^6
4	Vap	10^3	1	0.8	0.000835	0.00244	0.00498	1.39	5×10^6
5	Liq	4×10^3	2	0.8	8.02	8.54	8.99	2.15	2×10^6

3.7 Simulation results and discussion

Table 3.1 shows the parameters for the CPP simulations of the LJ fluid presented in this chapter. For reference, the critical temperature of the LJ fluid is around $T^* = 1.326$ [74]. In order to illustrate the range of densities in the CPP 1, 2, and 3 simulations, Figure 3.3 shows the range of densities superimposed on LJ phase boundaries [73, 75].

3.7.1 Supercritical simulations

In the absence of an external field, a pure-component fluid at temperatures above its critical temperature will not spontaneously split into different phases. However, the addition of a spatially varying external potential produces equilibrium density gradients (and therefore surface tension as predicted by density gradient theory).

A snapshot, as well as the external potential and density profile *vs* position z, of CPP simulation 1 are shown above in Figure 2.3. If no external field were present, this simulation would have the uniform density ρ^*_{avg} shown in Table 3.1. We used Eq. 3.16 to verify the
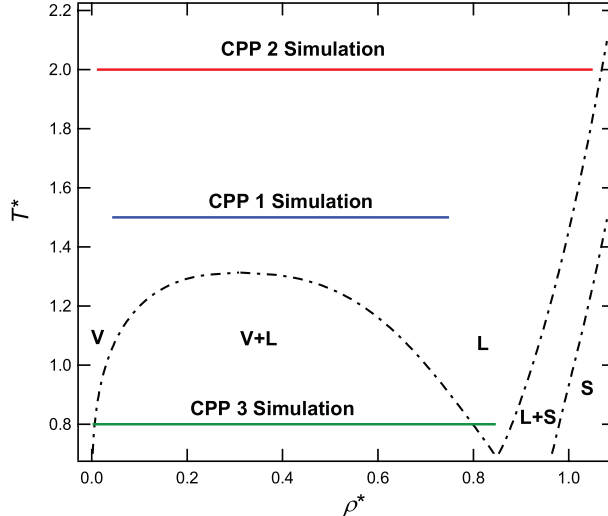
Figure 3.3: Density range in the CPP 1, 2, and 3 simulations (solid lines) along with LJ phase boundaries (dotted lines). The CPP method allows one to predict chemical potentials for a wide range of densities simultaneously using a single simulation.

system was at mechanical equilibrium and that P_N was calculated accurately using Eqs. 3.12 and 3.13. Agreement between left-hand and right-hand sides of Eq. 3.16 was essentially exact.

Figure 3.4 shows the resulting homogeneous chemical potential using the three different approximations of μ^{IH}, as well as the μ^{IH} curves themselves. Results are validated by comparing to those for the LJ EOS. The curve labeled as LJ EOS in Figure 3.4b is estimated using Eq. 3.8 with μ^0 given by the LJ EOS. For this system, the most accurate method of approximating μ^{IH} is the pressure tensor method. For the pressure tensor method, the magnitude of maximum deviation in μ^{IH} from the LJ EOS was 0.023 (reduced units), while for the TZ method it was 0.055 (2.4 times as high as the pressure tensor method), and for the VdW method it was 0.11 (4.9 times as high as the pressure tensor method).

Figure 3.5 shows profiles of inhomogeneous Helmholtz energy density *vs* position for CPP simulation 1 predicted using the VdW and TZ methods. For the VdW method, we used a value of $c^* = 4.4$ (constant with respect to density) [40]. Figure 3.5 also shows $[P_N(z) - P_T(z)]/2$ calculated using the IK contour is not equivalent to the predicted $\psi^{IH}(z)$.
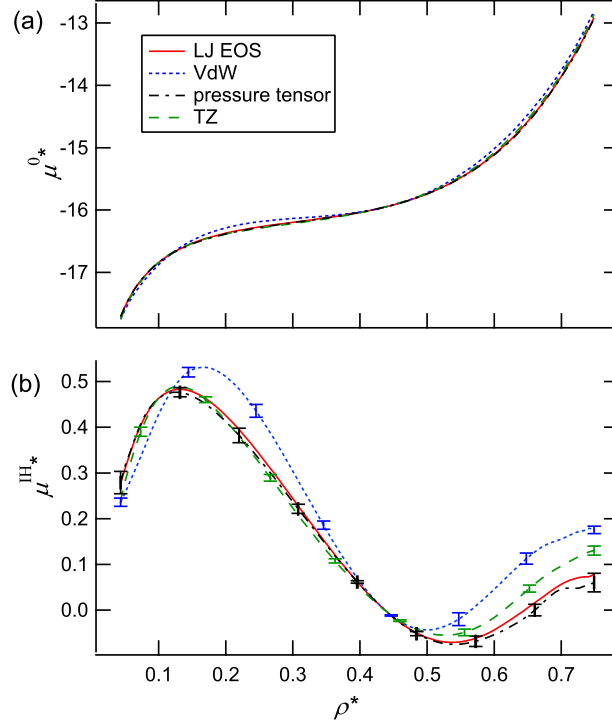
Figure 3.4: (a) Homogeneous chemical potential *vs* density for CPP simulation 1 using three different approximations of $\mu^{\text{IH}}(z)$. (b) Comparison of the different approximations of $\mu^{\text{IH}}(z)$ *vs* density. Density error bars are not shown for the VdW and TZ curves, but are identical to those shown for the pressure tensor curve.

Even though there isn't a well-defined surface in simulation 1, one can still calculate the apparent (induced) surface tension using the TZ equation (Eqs. 3.32 and the approximation given in Eq. 3.34), which gave $\gamma_{\text{TZ}}^* = 0.357 \pm 0.001$. One can also use the pressure tensor (Eq. 3.28) to calculate the surface tension, which gave $\gamma_{\text{IK}}^* = 0.311 \pm 0.015$. When an inhomogeneous long-range correction [76] was included with the pressure tensor, $\gamma_{\text{IK}}^* = 0.362 \pm 0.015$, producing better agreement between the two methods and further validating the approximation given in Eq. 3.34. The VdW method predicted a surface tension of $\gamma_{\text{VdW}}^* = 0.319 \pm 0.001$.

In order to test the influence of simulation cell length, we repeated CPP simulation 1 with length in the z direction increased by a factor of 5 (see Table 3.1). We refer to this simulation as 1L (where L stands for *long*). Figure 3.6 shows that increasing L_z decreases μ^{IH} as expected from gradient theory. The maximum deviation in μ^0 from the LJ EOS of
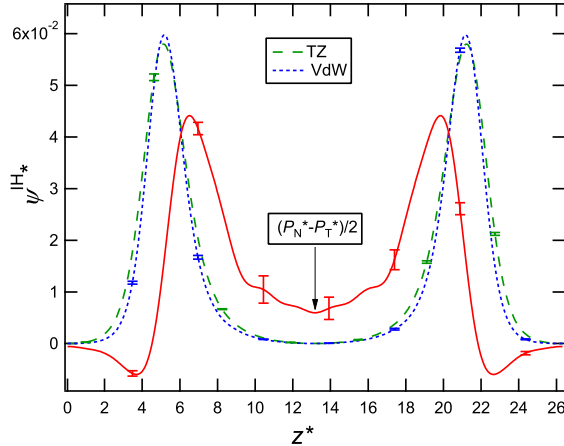
Figure 3.5: Plot of inhomogeneous Helmholtz energy density *vs* position for CPP simulation 1 predicted using the VdW and TZ methods. The quantity $[P_N(z) - P_T(z)]/2$ (calculated using the IK contour) is also shown, which does not match the predicted $\psi^{IH}(z)$.

the CPP 1 simulation *with* pressure tensor method correction was 0.023, while for the CPP 1 simulation *without* a correction method it was 0.483 (21 times as high as CPP simulation 1 with the correction), and for the CPP 1L simulation without a correction method it was 0.18 (7.8 times as high as CPP simulation 1 with the correction). In theory, one could increase the length of the simulation cell until μ^{IH} becomes negligible. However, Figure 3.6 also shows that if an appropriate gradient correction for μ^{IH} is used, one can obtain less error using a much shorter simulation cell. Obviously, if the simulation cell is too short, the correction becomes less reliable due to large density gradients. Furthermore, the use of large external field gradients can produce anomalous layering structures in the fluid.

The TZ and VdW methods take the derivative of ψ^0 to get μ^0, which tends to magnify noise in the data. The pressure tensor method integrates P^0 to get μ^0, which tends to smooth out noise in the data. Also, the pressure tensor is relatively easy to calculate. Therefore, the pressure tensor method to obtain μ^0 is the preferred method in this work and is used exclusively in the following results.

Figure 3.7 shows the results of supercritical CPP simulation 2 using a higher temperature and field strength than simulation 1. The highest density in this simulation was essentially at

38
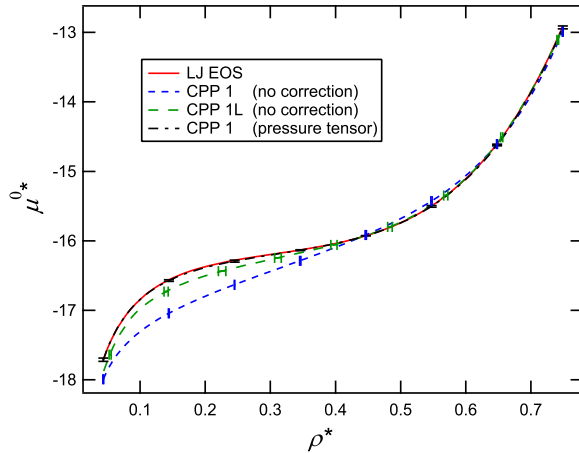
Figure 3.6: Comparison of homogeneous chemical potential *vs* density for CPP simulations 1 and 1L. Simulation 1L is 5 times longer in the z direction than simulation 1. Density error bars for the CPP1 curve with the pressure tensor correction are not shown but are identical to those shown for the CPP1 curve without a correction.

the liquid-solid coexistence point of liquid $\rho^* = 1.06$ [75]. Figure 3.7 also shows the results of homogeneous simulations using Widom's method (Eq. 2.3) for 12 discrete densities. These simulations included 10^3 particles and were run for 10^6 timesteps after equilibration. 10^3 insertions at random locations were performed every 8 timesteps. Each simulation was broken into 10 blocks, which were used to calculate 95% confidence intervals (using the Student's t-distribution) shown as error bars in Figure 3.7. The simulations used $r_c = 2.5\sigma$, and the standard LRC for chemical potential [5] was included. Relative error $\varepsilon = (\mu^0 - \mu^0_{\text{LJ EOS}}) / \triangle U^*_{\text{max}}$ is also shown for the CPP and Widom's methods in Figure 3.7b.

The CPP method and Widom's method have different convergence properties. Widom's method converges rapidly for lower densities but converges more slowly as the density of the system is increased. For this system, Widom's method starts to become inefficient around $\rho^* = 0.9$, where the probability of a favorable insertion is comparatively low. For Widom's method, the deviation from the EOS exceeds the uncertainty of the method at the highest density, showing a bias in the results. For the CPP method, the magnitude of the maximum relative error over the entire density range was 0.17%, while for Widom's method it was 9.3% (56 times as high as CPP). The total CPU time (after equilibration) used in the 12

39
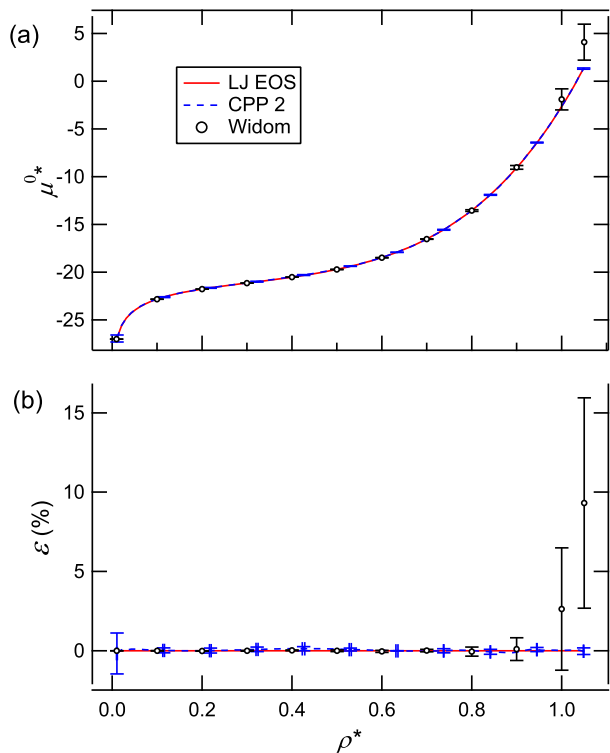
Figure 3.7: (a) Homogeneous chemical potential *vs* density for CPP simulation 2. Results from Widom's method are also shown. (b) Relative error as compared to the LJ EOS. The error bar visible at the lowest density is for the CPP method. Density error bars for the CPP method are not shown in (a) but are identical to those shown in (b).

Widom simulations was close to that of CPP simulation 2. One could further optimize the efficiency of Widom's method by sampling less at lower densities and more at higher densities. However, the spherical LJ model represents a best-case scenario for Widom's method; Widom's method converges even more slowly for large or structured molecules. The CPP method seems to converge both for low and high densities. The CPP method also gives a whole curve in a single simulation, while several simulations at different densities using Widom's method are necessary to obtain comparable results. However, because the CPP method uses one simulation for a wide composition range, it may be necessary to run the CPP simulation longer than a typical homogeneous simulation in order to obtain error bars of similar size. Using a Fourier series to smooth the data from the CPP method helps decrease noise.

40
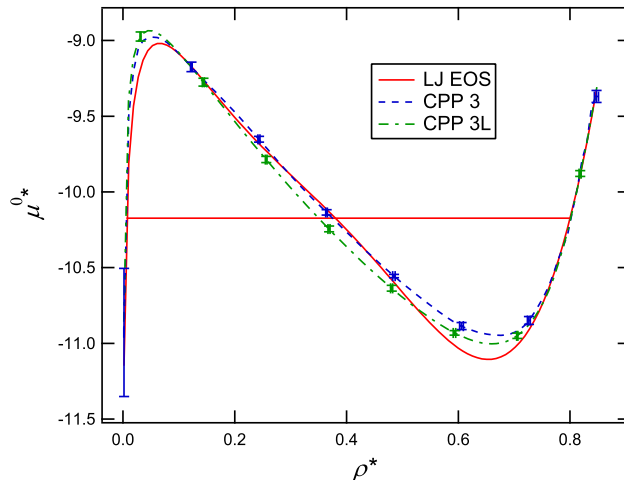
Figure 3.8: Homogeneous chemical potential *vs* density for two-phase CPP simulations 3 and 3L. The liquid-vapor tie line calculated using the LJ EOS is shown for reference.

3.7.2 Subcritical simulations

3.7.2.1 Two-phase systems

In simulations below the critical temperature, the fluid can spontaneously split into two phases. The addition of an external field merely increases the inhomogeneity of a two-phase system.

Figure 3.8 shows results of subcritical CPP simulations 3 and 3L, which included vapor, liquid, and two-phase regions. The constant μ^{tot} was determined by fitting the μ^0 curve to the LJ EOS at one liquid density ($\rho^* = 0.83$) at which the EOS is expected to be accurate. Figure 3.8 also shows that μ^0 exhibits a van der Waals loop in the two-phase region. The liquid-vapor tie line calculated using the LJ EOS is shown for reference in Figure 3.8. The μ^0 curves given by simulations 3 and 3L were fit using a Fourier cosine series. For CPP simulation 3, the magnitude of the maximum deviation in μ^0 from the LJ EOS was 0.32, while for CPP simulation 3L, it was 0.43.

Normally, two-phase molecular simulations predict coexisting densities by ignoring the interface and measuring average bulk-phase densities. In this work we determined the coexisting densities by equating the homogeneous pressures and the chemical potentials of the

41

Table 3.2: Predicted binodal and spinodal densities at $T^* = 0.8$ from CPP simulations 3 and 3L and the LJ EOS.

	Binodal ρ^*		Spinodal ρ^*	
	vapor	liquid	vapor	liquid
CPP 3	0.00413 ± 0.00019	0.805 ± 0.003	0.0512 ± 0.0027	0.673 ± 0.005
CPP 3L	0.00356 ± 0.00053	0.802 ± 0.001	0.0467 ± 0.0023	0.660 ± 0.005
LJ EOS	0.00608	0.800	0.0654	0.654

two phases predicted from simulation (because the external field disrupts bulk regions of constant density). The vapor-liquid coexisting (binodal) densities determined from CPP simulations 3 and 3L and the LJ EOS are shown in Table 3.2. Increasing the cutoff radius or using an inhomogeneous LRC may improve results.

The spinodal densities can be estimated by finding the minimum and maximum of the van der Waals loop in the homogeneous pressure profile predicted using Eq. 3.23 [50, 51]. We show the resulting spinodal densities from simulations 3 and 3L compared to the LJ EOS in Table 3.2. The CPP method allows one to obtain information about the metastable or unstable regions of the system that is difficult or impossible to determine experimentally. However, a potential problem with the use of Eq. 3.23 in the two-phase region is that one cannot eliminate or significantly decrease the inhomogeneity in the two-phase region by increasing the length of the simulation cell. If density gradients in this region are too large, the pressure tensor correction for the inhomogeneity of the system could be less reliable. We also note that it is difficult to validate spinodal densities using the LJ EOS because the EOS was not fit with data in the metastable or unstable regions. Vapor binodal and spinodal densities were also somewhat sensitive to the number of Fourier cosine terms used to fit the profiles.
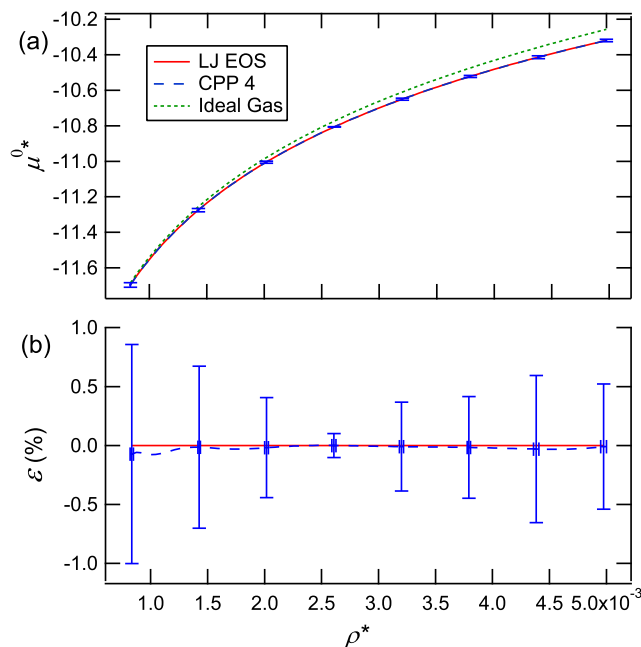
Figure 3.9: (a) Homogeneous chemical potential *vs* density for vapor-phase CPP simulation 4, which shows slight non-ideal gas behavior. (b) Relative error as compared to the LJ EOS. Density error bars for the CPP method are not shown in (a) but are identical to those shown in (b).

Figure 3.8 also shows that for this simulation set-up, random errors in the CPP method become significant at very low densities. This problem is easily overcome by performing a separate CPP simulation exclusively at vapor conditions as described below.

3.7.2.2 Single-phase systems

If one is interested only in the vapor or liquid regions (a single phase) of a subcritical fluid, a CPP simulation can be performed only at these conditions. The effect of an external potential on a single-phase subcritical fluid is similar to that for the supercritical case. Figure 3.9 shows the results of vapor-phase CPP simulation 4. The results show departure from ideal gas behavior. The maximum magnitude of relative error for this simulation was 0.077%. The agreement between CPP and the LJ EOS is better than the size of the error bars would suggest. For this simulation, there appears to be a cancellation of errors when the pressure
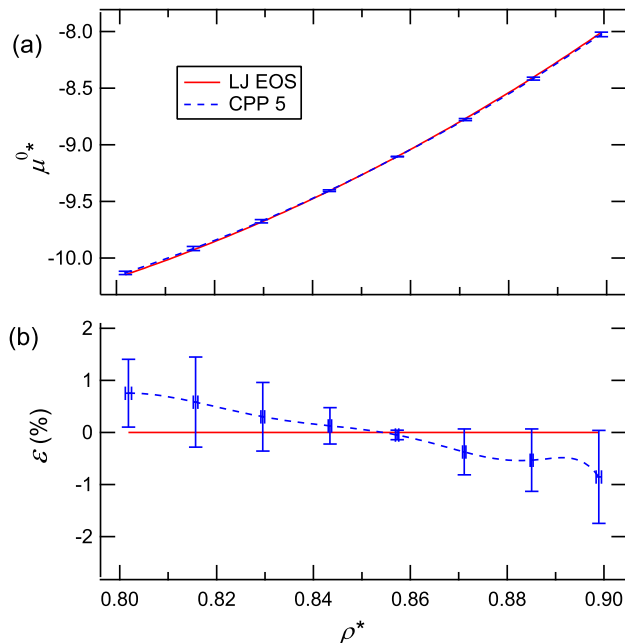
Figure 3.10: (a) Homogeneous chemical potential *vs* density for liquid-phase CPP simulation 5. (b) Relative error as compared to the LJ EOS. Density error bars for the CPP method are not shown in (a) but are identical to those shown in (b).

tensor correction is used. This may be because errors in the fits of the density and pressure tensor are correlated in this instance.

Figure 3.10 shows the results of liquid-phase CPP simulation 5. At this temperature, the density at the liquid-solid coexistence point is liquid $\rho^* = 0.881$ [75], so part of the results represent a metastable liquid region. The maximum magnitude of relative error for this simulation was 0.86%. There also appears to be a slight systematic disagreement between the results for this CPP simulation and the Kolafa and Nezbeda EOS.

3.8 Conclusion

A new method, called chemical potential perturbation (CPP), has been developed to predict the chemical potential in periodic molecular simulations. The CPP method applies a spatially varying external potential to the simulation, causing the density to depend upon position

in the simulation cell. Following equilibration the homogeneous (uniform or bulk) chemical potential as a function of density can be determined relative to some reference state after correcting for the effects of the inhomogeneity of the system. If desired, the homogeneous pressure and Helmholtz energy can also be predicted by the new method, as well as binodal and spinodal densities of a two-phase fluid.

Three different methods of approximating the inhomogeneous correction were compared. The VdW method uses the van der Waals density gradient theory to approximate the inhomogeneous Helmholtz energy density. The pressure tensor method uses the local pressure tensor to approximate the homogeneous pressure. The TZ method uses the Triezenberg-Zwanzig definition of surface tension to approximate the inhomogeneous Helmholtz energy density. The pressure tensor method is the most accurate, followed by the TZ method. The VdW method is not as accurate but results show the correct trend. Increasing the simulation cell length may decrease the inhomogeneity of the system, but the use of a correction allows one to obtain satisfactory results using a much shorter simulation cell or work with natural two-phase systems. Due to the ease of calculation and accuracy, the pressure tensor method is the preferred method for obtaining homogeneous properties in this work.

The CPP method was tested using a pure-component Lennard-Jones (LJ) fluid at vapor, liquid, two-phase, and supercritical conditions and results were compared to an LJ equation of state. The efficiency of the CPP method was also compared to that for Widom's method under the tested conditions. Both Widom's method and the CPP method work for low densities, and the CPP method also works for high densities where Widom's method starts to fail.

Chapter 4

Extension to lattice sum treatment of intermolecular potentials

4.1   Introduction

In order to increase the efficiency of molecular simulations, the intermolecular potential is usually truncated at some radial distance, and interactions beyond the cutoff are handled using a long-range correction (LRC) method. As described in Chapter 3, for a homogeneous (uniform) Lennard-Jones (LJ) fluid, standard tail corrections [69], which assume the radial distribution function is unity for $r \geq r_{\mathrm{cut}}$, are applied to the energy and pressure terms at the end of the simulation. These standard LRCs to energy and pressure depend on the average density of the system. Because the fluid is uniform, long-range forces cancel by symmetry, so no LRC force is applied to particles during the simulation.

For the inhomogeneous (non-uniform) fluid, however, the LRCs of energy, pressure tensor, and force depend on the density profile of the fluid, and corrections may need to be applied at every timestep. In Chapter 3, we observed satisfactory results for the LJ fluid by increasing the cutoff radius to $r_{\mathrm{cut}} = 5.5\sigma$ and neglecting the long-range force, instead applying a local tail correction for chemical potential [71] at the end of the simulation.

When simulating systems of one-dimensional density variations, an alternative LRC approach for the LJ fluid is to use slab-based methods, which account for inhomogeneity in one direction but still assume that the radial distribution function is unity for $r \geq r_{\mathrm{cut}}$. Chapela *et al.* and Blokhuis *et al.* approximated the long-range correction to surface tension by fitting

the average density profile (at the end of the simulation) using a hyperbolic tangent profile [77, 78]. However, their approach neglects the long-range energies or forces needed to obtain the proper density profile of the untruncated potential. Guo and Lu developed a slab-based method to predict long-range corrections for local thermodynamic properties such as energy, pressure, and surface tension [71]. Their approach partitions the long-range corrections into local and nonlocal terms. The local terms were applied during the course of the simulation using the local density (computed using slabs) and the nonlocal terms were often neglected. In this manner, their final density profile was closer to that of the untruncated potential. Lofti *et al.* developed a similar method using cylindrical instead of spherical coordinates [79, 80]. However, their approach neglected part of the long-range correction, which was later added by Janeček [76, 81]. Janeček's slab-based method allows one to obtain surface tension independent of cutoff radius for $r_{\text{cut}} \geq 2.5\sigma$. However, Janeček's method fails to properly account for periodic boundary conditions. This difficulty can be observed for homogeneous (uniform) simulations in which Janeček's method does not reduce to standard LRCs [82].

The Coulombic r^{-1} potential does not decay with distance as rapidly as the LJ potential and requires a more sophisticated treatment of the intermolecular potential; simply truncating the Coulombic potential can lead to artifacts [83–85]. This also means that slab-based methods should not be used for the Coulombic potential. A commonly used approach for Coulombic interactions is the lattice (Ewald) sum method, which has also been used for LJ dispersion interactions [86–89]. In this work, we extend the CPP method to a lattice sum treatment of intermolecular potentials for both Coulombic and LJ interactions. Conventional lattice sums naturally account for inhomogeneous densities in determining system energy and particle forces, but local values of the pressure tensor are not normally determined. Obtaining local properties from the lattice sum method is not as common as obtaining properties averaged over the entire volume of the system, but has been accomplished previously [90–94].

Choice of contour is also an important consideration in the CPP method. The IK contour was used in Chapter 3 to validate the CPP method for pure-component fluids. However, as described below, one must use the Harasima (H) [43] contour with the lattice sum method for reasons of computational efficiency. Some caution must be exercised when using the H contour though. The normal component of the pressure tensor is well-defined (to within a constant) as given by mechanical equilibrium [42]. For a planar interface, simulations show that the H contour violates this condition when used for the normal pressure [95, 96]. However, both gradient theory (Appendix A) and simulation results (below) show that the homogeneous pressure given by Eq. 3.23 is independent of the choice of contour (at least to within the order of truncation error) as long as the same contour (IK or H) is used for *both* components of the pressure tensor (normal and tangential).

In this chapter we show how to obtain the chemical potential using the CPP method with an Ewald lattice sum and the H contour. We validate the proposed methods by predicting the chemical potentials for both the LJ fluid and extended simple point-charge (SPC/E) water [97] and compare the results to respective equations of state. We also show preliminary results for LJ solids.

4.2   The H contour function

The H contour distributes the pair-wise pressure equally between the two point locations of the molecules of the interacting pair. This can be expressed as

$$\tau_{ijn}^{H}(z) = \frac{L_z}{2} \left[\delta \left(z - z_i \right) + \delta \left(z - z_j \right) \right] , \tag{4.1}$$

where δ is the Dirac delta function. In practice, $\mathbf{P}(z)$ is calculated with the H contour using a finite number of slabs, and each slab that contains one of the interacting molecules is given half the pressure from a given pair interaction. In Harasima's original formulation [43], he used a hybrid approach: the equivalent of Eq. 4.1 for P_T and the IK contour (Eq. 3.13) for

P_{N}. In this chapter, however, we use Eq. 4.1 contour for both P_{N} and P_{T}, and term this the H contour, which is also known as the IK1 convention in other works [95, 96, 98].

4.2.1 Obtaining homogeneous properties

A gradient expansion procedure can be used for the H contour pressure terms similar to that given for the IK contour in Chapter 3. As far as we know, this has not been published previously in the literature. As shown in Appendix A, a gradient expansion of $\mathbf{P}(z)$ using the H contour predicts that

$$P_{\mathrm{N}}^{\mathrm{H}}(z) = P^0(z) + k\left[-\tfrac{3}{2}\rho''(z)\,\rho(z)\right] + \mathcal{O}\left(\nabla^4\rho\right), \tag{4.2}$$

and

$$P_{\mathrm{T}}^{\mathrm{H}}(z) = P^0(z) + \tfrac{1}{3}k\left[-\tfrac{3}{2}\rho''(z)\,\rho(z)\right] + \mathcal{O}\left(\nabla^4\rho\right). \tag{4.3}$$

Combining Eqs. 4.2 and 4.3 shows that Eq. 3.23 is also valid when the H contour is used for both P_{N} and P_{T}. This means that either the IK or the H contour can be used in the CPP method to obtain homogeneous properties. This is important because as we explain below, the lattice sum method normally requires that the H contour be used. We note that Eq. 3.23 does not hold for Harasima's original hybrid formulation [43] of using Eq. 3.13 for P_{N} and Eq. 4.1 for P_{T}.

4.2.2 Local mechanical stability

Even though Eq. 3.23 holds for both the IK and H contours, some caution must be exercised when using the H contour (Eq. 4.1) to calculate P_{N} alone. For our system, mechanical stability is given by Eqs. 3.16 and 3.19. As shown by simulations, using the H contour for P_{N} violates this restriction [95, 96].

Violation of mechanical stability when using the H contour for P_N is also predicted by gradient theory. For large particle separation, the asymptotic value of the direct correlation function is $-u(s)/k_B T$. If we assume that $C^0(s, \rho) = -g^{(2)}(s, \rho_{avg}) u(s)/k_B T$ and that $g^{(2)}(s, \rho_{avg}) = 0$ when $s < \sigma$ and $g^{(2)}(s, \rho_{avg}) = 1$ when $s > \sigma$, then integration by parts of Eq. 3.22 yields Eq. 3.5, or $k = c(\rho)$ [34]. Assuming $k = c(\rho)$, substituting Eqs. 3.4 and 3.7 into Eq. 3.20 gives Eq. 3.19. This means that with these approximations, $P_N(z)$ calculated using the IK contour satisfies the condition for mechanical stability given in Eq. 3.19. For the H contour however, substituting Eqs. 3.4 and 3.7 into Eq. 4.2 does not give Eq. 3.19.

However, both gradient theory (Appendix A) and simulation results (below) support our conclusion that the homogeneous pressure given by Eq. 3.23 is independent of the choice of contour (at least to within the order of truncation error) as long as the same contour (IK or H) is used for *both* components of the pressure tensor (normal and tangential). Informally, one can think of this as a difference in pressure tensor components in which cancellation of error occurs. This is important because the H contour is more computationally efficient than the IK contour, especially when used with the lattice sum method. However, as shown below we also noticed that the IK contour has slightly less error than the H contour for a given simulation cell length. With this in mind, we used a hybrid approach: the IK contour for the short-range portion of the pressure tensor and the H contour for the long-range portion. The approach is described in detail below.

4.3 Obtaining local properties from a lattice sum

Here we briefly review the lattice sum method, which has been developed for both Coulombic and LJ dispersion interactions [86–89]. We focus on the local Coulombic pressure tensor, but a similar method can be used to obtain the local Coulombic internal energy (including self-interaction terms), as well as these quantities for the LJ potential.
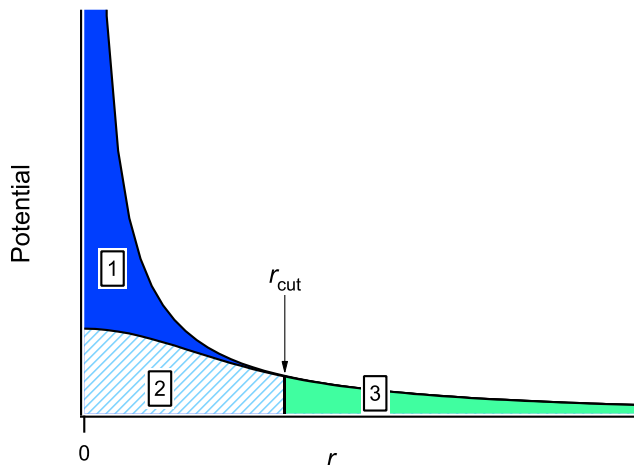
Figure 4.1: Conceptual division of the intermolecular potential in the lattice sum method.

As illustrated in Figure 4.1, the lattice sum method divides the intermolecular potential (r^{-1} in this case) into different regions. The real-space portion of a lattice sum calculates region 1 using a damped version of the full intermolecular potential. The reciprocal-space portion of a lattice sum includes regions 2 and 3, as well as self-interactions which must be removed. The division of calculation effort between the real and reciprocal parts can be tuned using a constant called α (see below).

Furthermore, we use a multi-timestep (MTS) algorithm [5, 87] in which the molecular interactions are divided into short- and long-range parts, and short-range interactions are updated more often than long-range ones. The short-range part of the potential is the full interaction out to $r = r_{\mathrm{cut}}$, naturally includes regions 1 and 2, and is not affected by the presence and use of a lattice sum. The long-range part is equal to the reciprocal-space portion of a lattice sum minus region 2. This correction to the reciprocal sum is calculated in real space, but is carried out less frequently than the full short-range interaction just mentioned.

Because the short-range portion of the pressure tensor is calculated using the full potential and the virial equation (Eq. 3.12), either the IK or H contour is available to obtain local values needed for the CPP method. In this work, we used the IK contour for the short-range

portion of the pressure tensor (regions 1 and 2) and the H contour for the long-range portion. To compute the long-range part, we calculated the region 2 correction using the H contour and subtracted it from the reciprocal-space part (which also uses the H contour). This means that the H contour is used only for interactions $r \geq r_{\text{cut}}$. One could alternatively use the H contour for all regions.

For the reciprocal portion of the pressure tensor, local values are not traditionally calculated and one obtains the volume-averaged pressure tensor (for Coulombic interactions) as [94]

$$\mathbf{P}^{\text{recip}} = \frac{1}{2\,V^2\,\varepsilon_0} \sum_{\mathbf{h} \neq 0} \Gamma(h)\,\chi(\mathbf{h}) \left[\mathbf{I} - 2\left(\frac{1}{4\alpha^2} + \frac{1}{h^2} \right) \mathbf{h}\,\mathbf{h}^{\mathrm{T}} \right] , \tag{4.4}$$

where $\mathbf{h}$ are the reciprocal lattice vectors, $h = |\mathbf{h}|$, ε_0 is the vacuum permittivity, and α is the constant that controls how the potential is divided between real and reciprocal space. $\Gamma(h)$ are Fourier coefficients given as

$$\Gamma(h) = h^{-2}\,e^{-h^2/4\alpha^2} . \tag{4.5}$$

For the volume-averaged pressure tensor, the quantity $\chi(\mathbf{h})$ can be defined as

$$
\begin{aligned}
\chi(\mathbf{h}) &= \sum_{i,j} q_i\,q_j\,e^{\mathbf{i}\,\mathbf{h}\cdot\mathbf{r}_{ijn}} \\
&= S(\mathbf{h})\,S(-\mathbf{h}),
\end{aligned}
\tag{4.6}
$$

where $\mathbf{r}_i$ is the position of the ith charge site q_i, $\mathbf{i}$ is the imaginary number, and $S(\mathbf{h})$ is the structure factor:

$$S(\mathbf{h}) = \sum_i q_i\,e^{\mathbf{i}\,\mathbf{h}\cdot\mathbf{r}_i} . \tag{4.7}$$

In this manner, one can reduce the expensive double sum in Eq. 4.6 to the single sum in Eq. 4.7.

In order to obtain the local pressure tensor $\mathbf{P}^{\mathrm{recip}}(z)$, one can replace $\chi(\mathbf{h})$ in Eq. 4.6 with a localized version. In the case of the H contour, this is [90, 92–94]

$$
\begin{aligned}
\chi(\mathbf{h}, z) &= \sum_{i,j} q_i q_j e^{\mathbf{i}\,\mathbf{h}\cdot\mathbf{r}_{ijn}} \tau_{ijn}^{\mathrm{H}}(z) \\
&= \sum_{i,j} q_i q_j e^{\mathbf{i}\,\mathbf{h}\cdot\mathbf{r}_{ijn}} \frac{L_z}{2} \left[\delta\left(z - z_i\right) + \delta\left(z - z_j\right)\right] \\
&= \tfrac{1}{2} S(-\mathbf{h}) S^{\mathrm{H}}(\mathbf{h}, z) + \tfrac{1}{2} S(\mathbf{h}) S^{\mathrm{H}}(-\mathbf{h}, z) \\
&= \mathrm{Re}\left[S(-\mathbf{h})\, S^{\mathrm{H}}(\mathbf{h}, z)\right] ,
\end{aligned}
\tag{4.8}
$$

where function $\mathrm{Re}(x)$ extracts the real part of x. $S^{\mathrm{H}}(\mathbf{h}, z)$ is defined as

$$
S^{\mathrm{H}}(\mathbf{h}, z) = L_z \sum_i q_i\, e^{\mathbf{i}\,\mathbf{h}\cdot\mathbf{r}_i} \delta\left(z - z_i\right) .
\tag{4.9}
$$

Using the H contour, one can reduce the double sum in Eq. 4.8 to the single sums in Eqs. 4.7 and 4.9, consistent with a traditional lattice sum. Thus this method of obtaining local properties requires little additional computational effort or storage over a traditional lattice (Ewald) sum.

If one wishes to use the IK contour to obtain local properties, the modification to $\chi(\mathbf{h})$ is

$$
\chi(\mathbf{h}, z) = \sum_{i,j} q_i q_j e^{\mathbf{i}\,\mathbf{h}\cdot\mathbf{r}_{ijn}} \tau_{ijn}^{\mathrm{IK}}(z) .
\tag{4.10}
$$

Unfortunately, Eq. 4.10 cannot be separated in the same way as Eq. 4.8 and therefore requires a double loop over molecules instead of the single loop that is used in standard lattice sum routines. This double loop is prohibitively expensive, so the IK contour is normally not used

with a lattice sum. We note however that the method of planes can use single-site forces to obtain the IK version of P_{N} in an efficient manner with a lattice sum [98]. It is also trivial to calculate the IK version of P_{N} (to within a constant) using Eq. 6.16. Unfortunately neither of these solutions are available for P_{T}.

4.4   Optimizing the CPP method

The CPP method uses Eq. 3.23 to approximate the homogeneous pressure, with the truncation error of this approximation given as $\mathcal{O}\left(\nabla^4\rho\right)$. This means that lowering the density gradients of the system will increase the accuracy of this approximation. We describe two ways to accomplish this.

First, for supercritical and single-phase conditions, one can simply increase the length of the simulation cell, recognizing that this also increases computational cost (unless the width and height are decreased at the same time).

Second, one can change the form of the external potential to reduce density gradients. The CPP method as originally proposed in Chapter 3 uses an external potential of the form given in Eq. 3.35. For some simulations, using this form of U^{ext} may produce sharp changes in density, which in turn decreases the accuracy of the inhomogeneous correction term. One can generalize Eq. 3.35 to a Fourier cosine series as

$$U^{\mathrm{ext}}(z) = \sum_{n=1}^{n_{\mathrm{max}}} A_n \cos\left(\frac{2\pi\, n\, z}{L_z}\right),\qquad(4.11)$$

where n_{max} is the number of terms in the Fourier series and A_n are the Fourier coefficients.

For supercritical or single-phase simulations, one can use Eq. 4.11 to adjust the form of $U^{\mathrm{ext}}(z)$ and obtain any desired density profile, including a sinusoidal density profile. This can be accomplished iteratively by using Eq. 3.35 and a CPP simulation to obtain a preliminary curve of $\rho(z)$ *vs* $U^{\mathrm{ext}}(z)$, and then using this information to predict the form of the external potential that gives the desired sinusoidal density profile, and then running another CPP
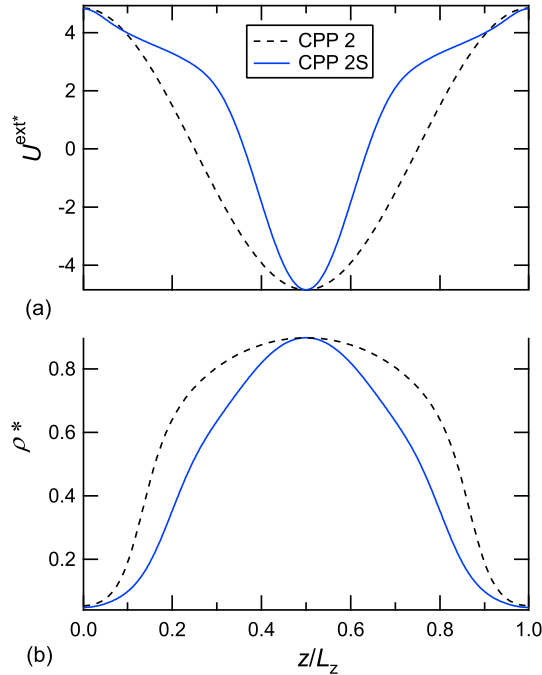
Figure 4.2: (a) Different forms of external potential and (b) resulting density profiles.

simulation with the updated external potential. This process can be repeated until one obtains the desired density profile. We found that one or two iterations were sufficient to significantly reduce density gradients. For example, Figure 4.2 compares the CPP 2 and 2S simulations (described below). The CPP 2 simulation used Eq. 3.35, while the 2S simulation used Eq. 4.11, reducing density gradients by about $40\,\%$ after one iteration as compared to the CPP 2 simulation.

4.5   Internal energy, enthalpy, and entropy

We note that the CPP method allows one to predict the full set of thermodynamic functions. For instance, the internal energy density $\phi^0(\rho, T)$ is related to the Helmholtz energy density $\psi^0(\rho, T)$ as

$$\phi^0(\rho, T) = -T^2 \left[\frac{\partial \left(\psi^0(\rho, T)/T \right)}{\partial T} \right]_\rho . \tag{4.12}$$

However, Eq. 4.12 requires temperature derivatives of ψ^0, but CPP simulations are run at constant temperature. Several CPP simulations could be run at different temperatures to obtain this formation. Here, we show an alternative route to ϕ^0 that avoids derivatives with respect to temperature.

One can calculate the total internal energy density $\phi^{\text{tot}}(z)$ using an expression similar to the one given for the pressure tensor (Eq. 3.12) as

$$\phi^{\text{tot}}(z) = \phi^{\text{ig}}(z) + \frac{1}{V} \sum_i \sum_{j<i} u_{ijn}\, \tau_{ijn}(z)\,, \tag{4.13}$$

where $\phi^{\text{ig}}(z)$ is the local ideal gas internal energy density.

As was done for $\mathbf{P}$ and μ, we partition the total internal energy density $\phi^{\text{tot}}(z)$ into homogeneous and inhomogeneous parts:

$$\phi^{\text{tot}}(z) = \phi^0(z) + \phi^{\text{IH}}(z)\,. \tag{4.14}$$

As before, one must approximate the inhomogeneous term ϕ^{IH} to obtain the desired homogeneous term ϕ^0. As shown in Appendix B, a Taylor series expansion of Eq. 4.13 in density gradients predicts

$$\phi^0(z) = \phi^{\text{tot}}(z) - \tfrac{1}{2}\left[P_{\text{N}}(z) - P_{\text{T}}(z)\right] + \mathcal{O}\left(\nabla^4 \rho\right)\,. \tag{4.15}$$

With $\phi^0(z)$ given by Eq. 4.15, the homogeneous enthalpy density $\eta^0(z)$ can be calculated as

$$\eta^0(z) = \phi^0(z) + P^0(z)\,, \tag{4.16}$$

and the homogeneous entropy density $\zeta^0(z)$ can likewise be calculated as

$$\zeta^0(z) = \frac{\eta^0(z) - \mu^0(z)\rho(z)}{T}\,. \tag{4.17}$$

56

Eqs. 4.15-4.17 avoid the need for temperature derivatives and allow these properties to be obtained for several densities simultaneously using a single CPP simulation; several homogeneous simulations run at different densities would be required to obtain similar results.

4.6   Simulation details

In order to test the proposed methods, we used pure-component simulations of an LJ fluid [5] as well as of SPC/E water [97]. The CPP method can be used for two-phase systems as described in Chapter 3. However, the results for two-phase systems are harder to validate than for supercritical conditions because a natural two-phase system contains densities in the metastable and unstable areas where equations of state (EOS) are not validated. We therefore simulated the fluids at supercritical conditions and applied a large external potential to more easily validate the results using an EOS.

In order to estimate the bias in the CPP method for the LJ simulations, we used the Kolafa and Nezbeda EOS [72] with the same LJ ideal gas expression given in Chapter 3. Simulated water results are compared to an equation of state for SPC/E water [99]. This EOS gives chemical potential in excess of an ideal gas. For simplicity, the density-dependent part of the SPC/E ideal gas chemical potential was included and all chemical potentials for SPC/E are given relative to that of the average system density ρ_{avg}.

The molecular dynamics (MD) method was used to generate equilibrium averages. The equations of motion included an integral-control (Nosé-Hoover) thermostat and were integrated using a 4th-order Gear predictor-corrector scheme [69]. The size of the timestep was selected for each simulation to generate a root-mean-square displacement of molecules of 0.003σ per timestep for the LJ fluid. The timestep for SPC/E water was 0.610 fs. A Verlet neighbor list was used to speed up computations [69]. Samples for density and pressure profiles were taken every 8 timesteps and were collected using 401 equally spaced slabs normal to the z direction. This setup is similar to that used in Chapter 3.

Resulting pressure and density profiles were each fit using a Fourier cosine series, as this automatically satisfies the periodicity and symmetry of the system. Additionally, limiting the number of terms in the Fourier cosine series worked well to screen out noise and smooth the data.

Random errors were estimated using the block method. Each simulation was divided into 10 blocks, which were used to calculate 95% confidence intervals of the data using the Student's t-distribution. Simulation results are generally plotted as continuous curves, while error bars are plotted for several points along the curves in order to give the reader a sense of the random errors in the simulations. In the CPP method, both the measured density and the pressure, chemical potential, *etc.* vary at a given cell position. Thus a plot of μ, P, or ϕ *vs* ρ requires error bars in both directions. For simplicity the error bars in density are not shown in the figures below. The average 95% confidence intervals in density were $\pm 5 \times 10^{-4}$ (reduced units) for the LJ fluid simulations (5% of the lowest density in the LJ simulations in this chapter). For the SPC/E water simulation, the average 95% confidence intervals in density were $\pm 3\,\mathrm{kg/m^3}$ (14% of the lowest density in this simulation).

The CPP method gives differences in chemical potentials as a function of density. Another method such as Widom's or an EOS is needed to determine the unknown constant (or reference) μ^{tot}. In this work, μ^{tot} was determined by shifting the $\mu^0(z)$ curve vertically until it matched the equation of state at ρ_{avg}. Because μ^0 is fixed at this point, the apparent error at this point will be zero. Alternatively, we could have determined μ^{tot} by performing Widom insertions in one slice of the CPP simulation or in a separate homogeneous simulation at one density contained in the CPP simulation.

Table 4.1: Parameters for the pure-component LJ simulations shown in Chapter 4.

Name	N	$\frac{L_z}{L_x=L_y}$	T^*	$\rho^*_{\min}$	ρ^*_{avg}	$\rho^*_{\max}$	$\triangle U^*_{\max}$	timesteps
1IK	8×10^3	1	2.0	0.010	0.400	0.809	14.0	5×10^5
1H	8×10^3	1	2.0	0.010	0.400	0.809	14.0	5×10^5
2	2×10^3	2	1.5	0.053	0.598	0.898	9.67	5×10^6
2S	2×10^3	2	1.5	0.048	0.475	0.898	9.67	5×10^6

4.7   Simulation results and discussion

4.7.1   Lennard-Jones fluid simulations

Table 4.1 shows the parameters for the LJ simulations presented in this chapter. The 1IK and 1H simulations respectively used the IK and H contours with a very large cutoff ($r_{\text{cut}} = 13.6\sigma$) and no additional LRCs. The CPP 2 and 2S simulations used the hybrid pressure tensor approach (the IK contour for short-range and the H contour for long-range) and the lattice
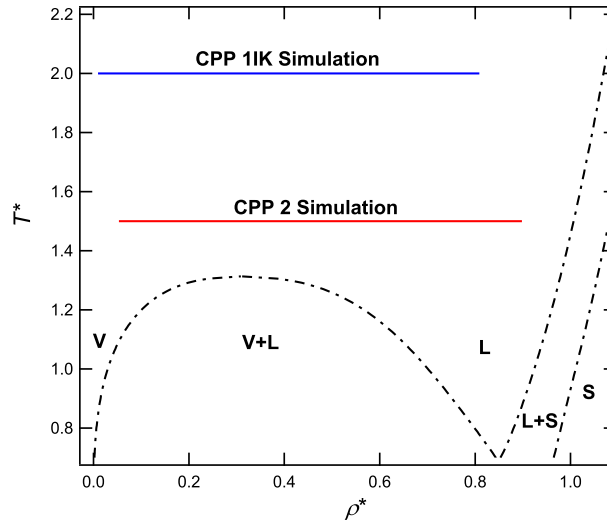
Figure 4.3: Density range in the CPP 1IK and 2 simulations (solid lines) along with LJ phase boundaries (dotted lines). The CPP method allows one to predict chemical potentials for a wide range of densities simultaneously using a single simulation.
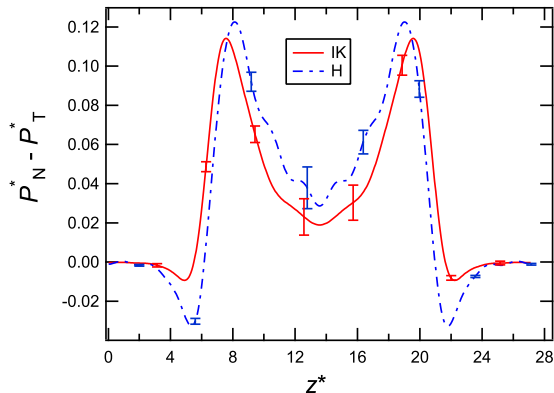
Figure 4.4: Plot of the local surface tension $P_N(z) - P_T(z)$ using the IK and H contours.

sum method for both Coulombic and LJ interactions. The 2S simulation (where S stands for *smooth*) differs from the CPP 2 simulation in its use of a more complex form of external potential (Eq. 4.11) to reduce density gradients in the simulation (see Figure 4.2). Because parts of this work are published in separate papers, the names of simulations for each chapter are independent. For example, the CPP 2 simulation in this chapter is not the same as that of Chapter 3. In order to illustrate the range of densities in the 1IK and 2 simulations, Figure 4.3 shows the range of densities superimposed on LJ phase boundaries [73, 75].

For periodic simulations with planar symmetry, the overall surface tension γ is related to the pressure tensor according to Eq. 3.28. In a similar manner, one can define a local surface tension as $P_N(z) - P_T(z)$. Figure 4.4 compares the local surface tension in the 1IK and 1H simulations. For this system, there is a noticeable difference in how the surface tension is distributed locally. We note that because different simulations were used for each contour, the overall (or average) surface tension is not exactly the same for both simulations.

One can use Eq. 3.16 to check if the normal pressure calculated using different contours satisfies the condition for local mechanical stability. Figure 4.5 shows the left-hand side (LHS) $dP_N(z)/dz$ of Eq. 3.16 minus the right-hand side (RHS) $\rho(z) f^{\text{ext}}(z)$ for both contours. As shown in Figure 4.5, the magnitude of the maximum error in dP_N/dz for the IK contour was 5.0×10^{-3} (reduced units), while for the H contour it was 0.063 (13 times as high as
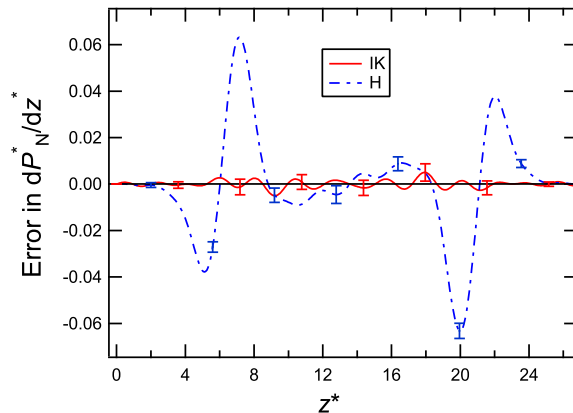
Figure 4.5: Plot of the LHS of Eq. 3.16 minus the RHS for both the IK and H contours. The IK contour produces less error than the H contour.

the IK contour). This suggests that the IK contour satisfies and the H contour violates the restriction given in Eq. 3.16 as expected [95, 96].

In contrast, as shown in Figure 4.6, the homogeneous pressure can be obtained using either the IK or the H contour and the pressure tensor difference method (Eq. 3.23). For the IK contour, the magnitude of the maximum deviation in P^0 from the LJ EOS was 0.012, while for the H contour it was 0.021 (1.8 times as high as the IK contour).

The CPP 2 simulation used the Ewald sum method, with a real-space cutoff of $r_{\text{cut}} = 4.0\sigma$ and a damping factor of $\alpha = 0.7024\,\sigma^{-1}$. For a simulation cell elongated in the z direction, it is necessary to increase the number of lattice vectors in this direction accordingly to maintain a spherical cutoff [91]. A lattice (or wavevector) cutoff of $h_{\text{cut}} = 4.366\,\sigma^{-1}$ was used.

With the CPP method, average properties vary only in one direction, so one can use a slab-based method to validate local properties obtained from the lattice sum method. The long-range portion of the local surface tension can be approximated using the H contour and a virial-type expression as [71, 77, 78]

$$P_{\text{N}}^{\text{LR}}(z) - P_{\text{T}}^{\text{LR}}(z) = \frac{\pi}{2}\rho(z) \int_{r_{\text{cut}}}^{\infty} dr \, \frac{d\,u(r)}{dr} \int_{-r}^{r} dz' \left[r^2 - 3\,(z')^2 \right] \rho\,(z + z') \,, \qquad (4.18)$$
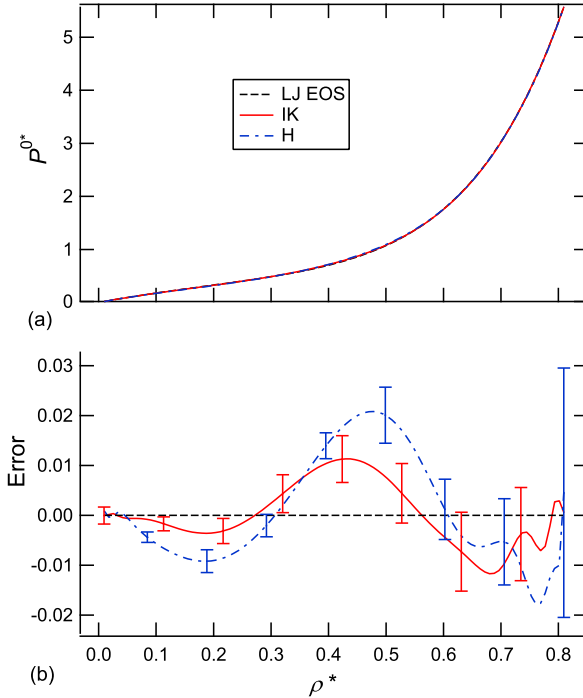
Figure 4.6: Plots of (a) P^0 calculated using Eq. 3.23 comparing the IK and H contours and (b) associated absolute errors in pressure as compared to the EOS.

where $u(r)$ is the LJ potential. Figure 4.7 shows the local long-range contribution to surface tension calculated using Eq. 4.18 and the average density profile from the CPP 2 simulation, as well as the same quantity calculated using the lattice sum method. The magnitude of the maximum difference between the two methods was 1.5×10^{-4}.

The CPP 2S simulation is similar to the CPP 2 simulation but used an alternative form of U^{ext} to reduce the density gradients of the simulation and the resulting truncation error in Eq. 3.23 (see Figure 4.2). The CPP 2S simulation used the Ewald sum method, with $r_{\text{cut}} = 4.0\sigma$, $\alpha = 0.7024\,\sigma^{-1}$, and $h_{\text{cut}} = 4.386\,\sigma^{-1}$. The average of the absolute value of the error in the CPP simulation 2S was 0.013, while for CPP simulation 2 it was 0.023 (1.8 times as high as simulation 2S) as shown in Figure 4.8.

We noticed with the CPP method, attempting to simulate very low and high densities in the same simulation gave relatively large error bars for low densities due to poor sampling statistics (*i.e.* there are fewer molecules at positions of low densities). This problem is
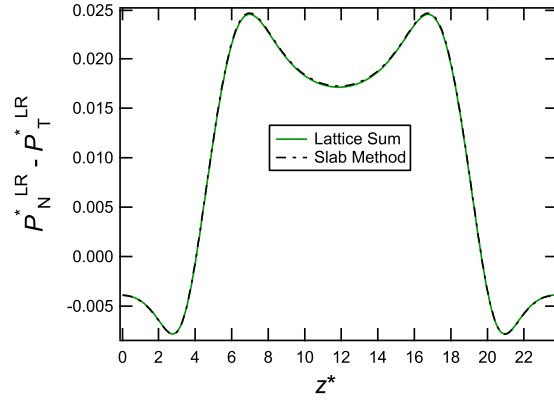
Figure 4.7: Local long-range contribution ($r > 4.0\sigma$) to the surface tension for the lattice sum method compared to that of the slab-based method for the LJ fluid.

easily overcome by performing an additional CPP simulation at a lower average density (see Chapter 3).
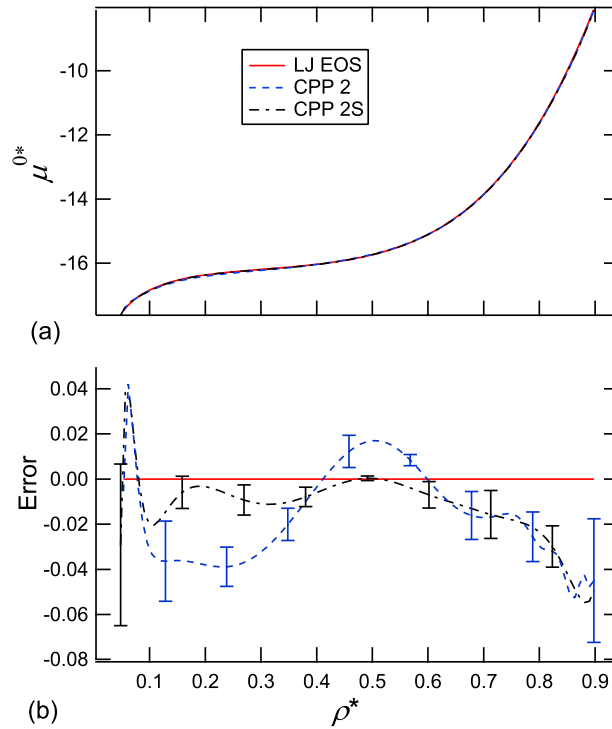
Figure 4.8: (a) Chemical potentials predicted using different forms of the external field and (b) associated absolute errors as compared to the EOS.
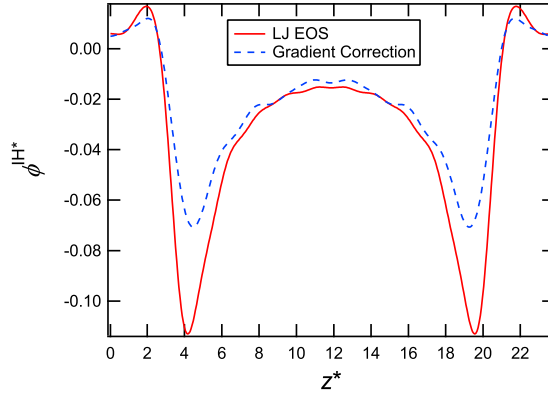
Figure 4.9: ϕ^{IH} *vs* position z for the CPP 2 simulation.

Figure 4.9 shows the inhomogeneous internal energy density ϕ^{IH} for the CPP 2 simulation using the gradient correction given in Eq. 4.15 as compared to the LJ EOS. The LJ EOS curve for ϕ^{IH} in Figure 4.9 is calculated using Eq. 4.14, with ϕ^0 given by the LJ EOS and ϕ^{tot} given by Eq. 4.13.

Figure 4.10 shows the predicted homogeneous internal energy density for the 2 and 2S simulations. For the CPP 2S simulation, the magnitude of the maximum deviation in ϕ^0 from the LJ EOS was 0.018, while for the CPP 2 simulation with the inhomogeneous correction it was 0.047 (2.6 times as high as the 2S simulation), and for CPP simulation 2 without the correction, it was 0.11, (6.3 times as high as the 2S simulation). The simplified gradient correction for ϕ^{IH} does reduce bias in the method, but is not as satisfactory as that for P^0 given in Eq. 3.23. This is due to the assumption that k (Eq. 3.22) is equal to k' (Eq. B.9). See Appendix B for more details. Using both the simplified gradient correction (Eq. 4.15) and reducing density gradients by changing the external potential (*i.e.* the 2S simulation) produce the best results. The CPP 2 and 2S simulations used a relatively small number of particles and a short simulation cell. Elongating the simulation cell in the z direction would further eliminate error in these simulations.
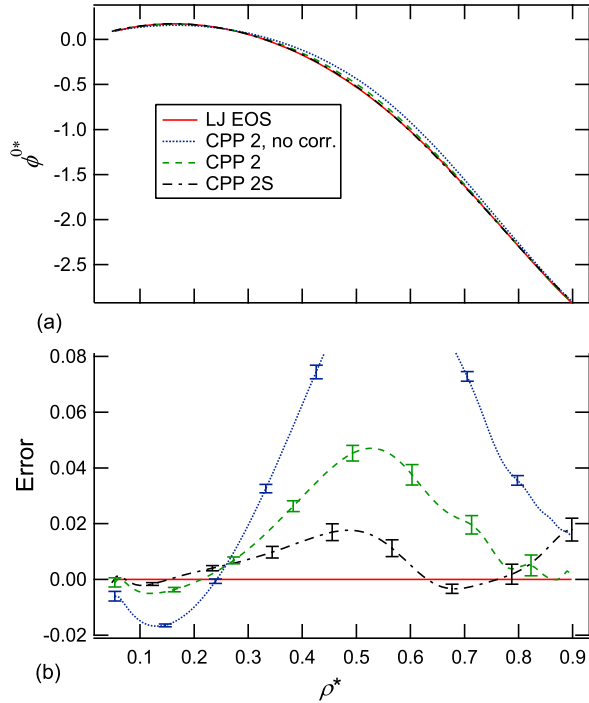
Figure 4.10: (a) Homogeneous internal energy density predicted using the CPP method and (b) associated absolute errors as compared to the LJ EOS. The CPP 2 results are shown both with and without an inhomogeneous correction (Eq. 4.15).

Table 4.2: Parameters for the LJ fluid-solid test simulation.

Name	N	$\frac{L_z}{L_x=L_y}$	T^*	ρ^*_{min}	ρ^*_{avg}	ρ^*_{max}	$\triangle U^*_{max}$	timesteps
3	10^4	10	1.5	0.015	0.817	1.199	30.0	10^6

4.7.2 Lennard-Jones solid

In this section we explore the use of the CPP method for solid systems and show preliminary results for the LJ potential. Table 4.2 shows the parameters for fluid-solid test simulation 3, run at supercritical conditions. This simulation was run at the same temperature as the 2 and 2S simulations (see Table 4.1) shown in the previous subsection), but used a much stronger external potential and higher average density. The Ewald sum method was used, with $r_{cut} = 4.0\sigma$, $\alpha = 0.7024\,\sigma^{-1}$, and $h_{cut} = 4.356\,\sigma^{-1}$.
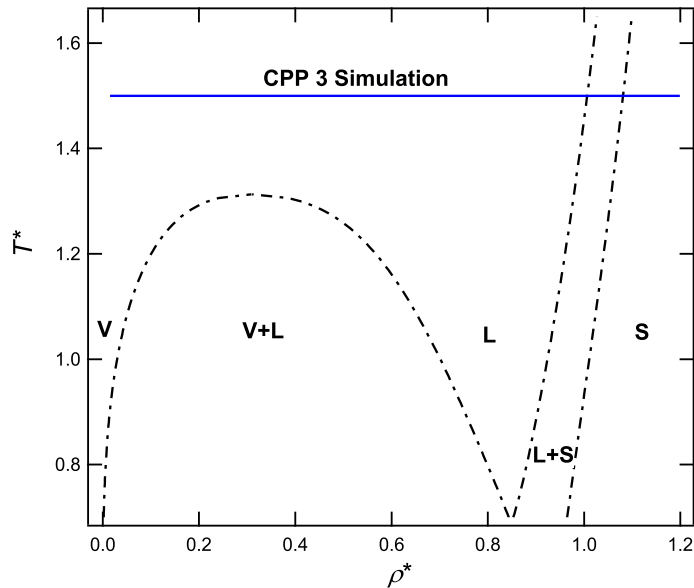
Figure 4.11: Range of state points in LJ fluid-solid simulation 3, along with LJ phase boundaries.
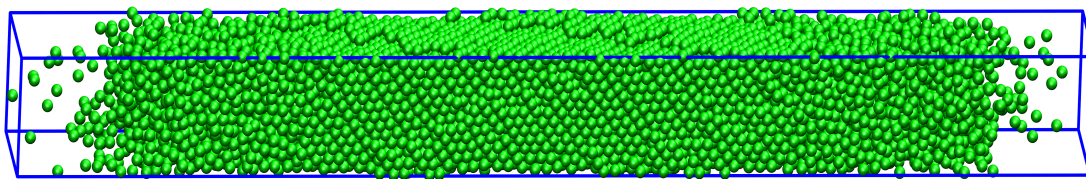
Figure 4.12: Snapshot of fluid-solid simulation 3, showing a wide range of densities.

Figure 4.11 shows the range of densities in CPP simulation 3 superimposed on LJ phase boundaries [73, 75]. Figure 4.12 shows a snapshot of simulation 3, produced using the VMD software program [33], with solid phase visible at the center of the simulation cell and fluid visible near the edges.

Some challenges arise when simulating solid systems with the CPP method. One frequently encounters interfaces and defects in the lattice, and the external potential also produces lattice strain in one direction, which combines with anisotropy of the solid to introduce additional complications. It appeared that the pressure tensor correction (Eq. 3.23) is less accurate for this solid, so no inhomogeneous correction was included in simulation 3. Instead,
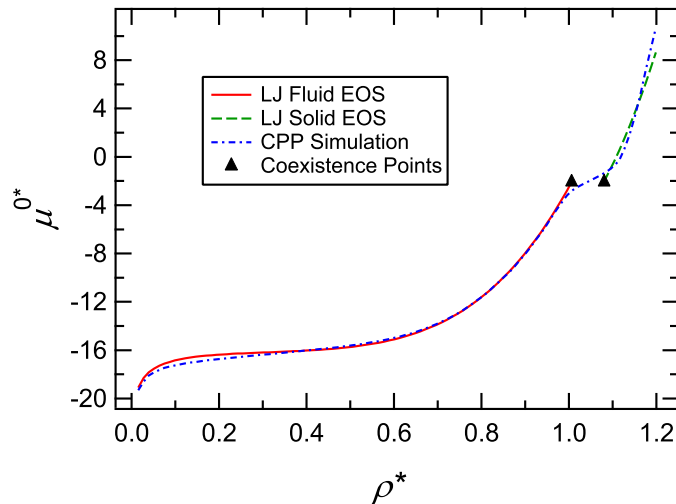
Figure 4.13: Homogeneous chemical potential *vs* density for fluid-solid simulation 3.

Table 4.3: Parameters for the SPC/E water simulation. Densities are given in kg/m³.

Name	N	$\frac{L_z}{L_x=L_y}$	$T\,(\mathrm{K})$	$\rho_{\min}$	ρ_{avg}	$\rho_{\max}$	$\triangle U_{\max}\,(\mathrm{kJ/mol})$	timesteps
SPC/E	2000	2	700	22	410	790	10.7	10^6

the simulation cell was elongated in the z direction, which reduced density gradients and the need for the inhomogeneous correction term.

Figure 4.13 shows results for simulation 3 compared to LJ equations of state for fluids [72] and solids [75], which suggest that the CPP method could be used to predict properties for solids. However, further development of the CPP method for solids was beyond the scope of this project.

4.7.3 SPC/E water simulation

Table 4.3 shows the parameters for the extended simple point-charge (SPC/E) water [97] simulation presented in this work. The SPC/E water model contains 3 molecular sites: one for each hydrogen atom and one for oxygen. The hydrogen sites have a fixed partial point charge of 0.4238 $|e|$, where $|e|$ is the magnitude of charge of an electron, while the
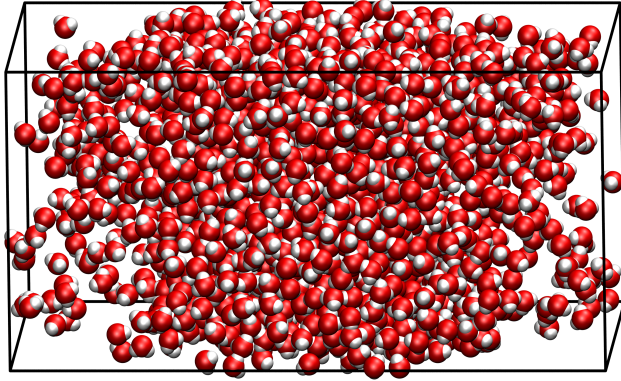
Figure 4.14: Snapshot of the SPC/E simulation.

oxygen site has both a partial point charge of $-0.8476\,|e|$ and a Lennard-Jones interaction of $\sigma = 0.31656\,\text{nm}$ and $\varepsilon/k_\text{B} = 78.197\,\text{K}$. The hydrogen sites are separated from the oxygen site using a rigid bond length of 0.1 nm, and the angle formed between the oxygen and hydrogen sites is 109.47 degrees. This model is considered a benchmark for water because the model captures the essential physics of water and yet is relatively computationally efficient and simple to implement.

The external potential acted on the molecular center of mass and was invariant to the orientation of the SPC/E molecule. We used a molecular version of the pressure tensor, with local properties using the IK or H contour also calculated using the molecular center of mass. The Ewald sum method was used for both Coulombic and LJ interactions, with $r_\text{cut} = 0.900$ nm, $\alpha = 0.0343$ nm^{-1}, and $h_\text{cut} = 0.265$ nm^{-1}. In order to reduce density gradients and increase the accuracy of this simulation, the form of the external potential was adjusted to produce a sinusoidal density profile as described above.

Figure 4.14 shows a snapshot of the SPC/E simulation, produced using the VMD software program [33]. Figure 4.15 shows the homogeneous pressure of SPC/E water predicted using the CPP method. For this CPP simulation, the magnitude of the maximum deviation in P^0 from the SPC/E EOS was 1.9 MPa. The surface tension of SPC/E water has previously been shown to depend somewhat on choice of Ewald parameters [94]. In this work we also
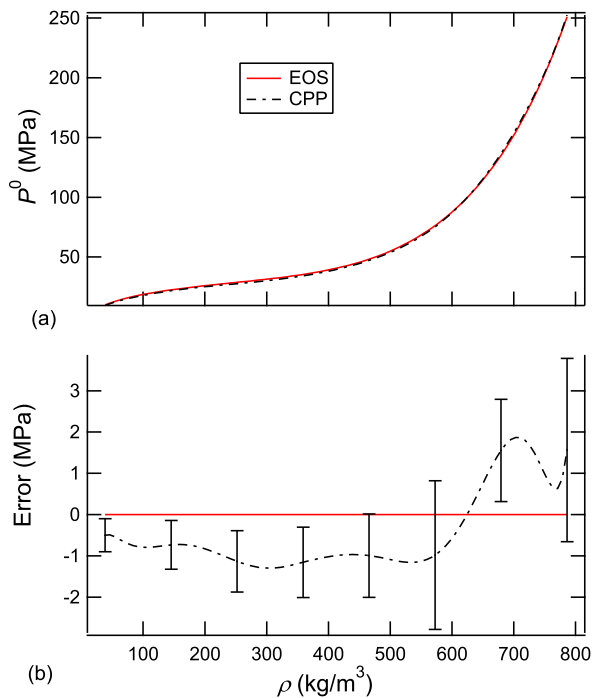
Figure 4.15: (a) Homogeneous pressure of SPC/E water at 700 K using the CPP method and (b) corresponding absolute error as compared to the EOS.

noticed that the values of homogeneous pressure for higher densities in the simulation were somewhat sensitive (by a few percent) to the choice of Ewald parameters.

As shown in Figure 4.16, the magnitude of the maximum deviation in μ^0 from the SPC/E EOS using the CPP method was 0.10 kJ/mol. We note that determining chemical potentials using particle insertion methods such as Widom's becomes increasingly troublesome for large, structured molecules and dense systems. For example, Widom's method fails to determine the chemical potential of liquid water ($\rho = 1000\,\text{kg/m}^3$) and a more sophisticated method such as Bennett's overlapping distribution method [10] must be used [100].

4.8   Conclusion

The CPP method has been extended to a lattice (Ewald) sum treatment of intermolecular potentials. For a planar interface, the homogeneous pressure and resulting chemical potential
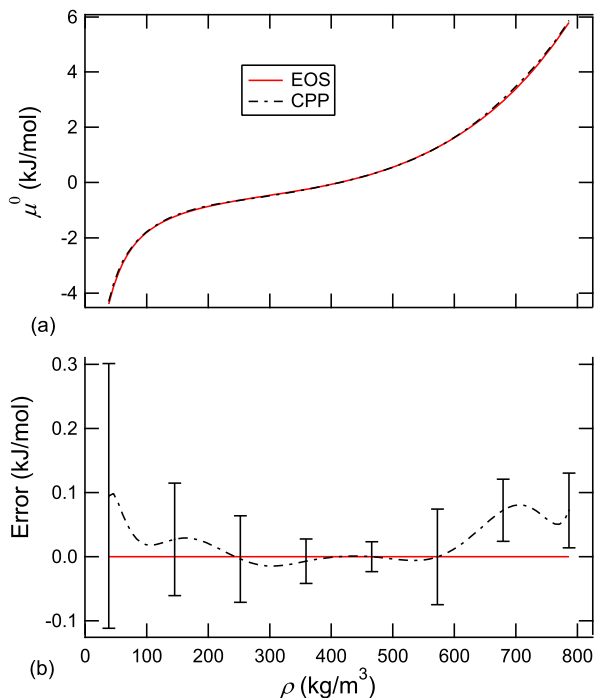
Figure 4.16: (a) Homogeneous chemical potential of SPC/E water at 700 K (relative to the chemical potential of the average system density) and (b) corresponding absolute error as compared to the EOS.

can be approximated with the CPP method using either the IK or the H contour, though the H contour shouldn't be used to obtain P_N alone. We have reviewed how to obtain local properties using the lattice sum method and have shown the H contour has much greater computational efficiency than the IK contour with the lattice sum method. The CPP method has been extended to obtain the internal energy with a simplified gradient correction term for internal energy. The simplified gradient correction for internal energy does reduce bias in the method but is not as satisfactory as that for pressure. One can adjust the form of the external potential to reduce density gradients and increase efficiency of the CPP method using a Fourier series expansion. The proposed methods are validated by simulating the LJ fluid and SPC/E water and results are compared to respective equations of state.

Chapter 5

A new lattice sum method for the LJ fluid

5.1 Introduction

As described in Chapter 4, the Ewald sum method can be used in conjunction with the LJ fluid. However, when simulating inhomogeneous LJ systems in which average properties vary only in one direction, using a full lattice sum is computationally inefficient because one must compute spatially varying properties for all three dimensions (instead of just one). Slab-based methods (see Chapter 4) have been developed to account for variations in one direction in a more efficient manner. However, as described below, certain difficulties arise when using traditional slab-based methods. In this chapter we give a more detailed description of the slab-based method and develop an improved method that combines some of the advantages of the lattice sum with those of the slab-based method.

5.2 Traditional slab-based method

One can express the total potential energy of the system U as a volume integral of the following form:

$$U = \frac{1}{2} \int \int u(r_{12}) \rho(\mathbf{r}_1) \rho(\mathbf{r}_2) d\mathbf{r}_1 \, d\mathbf{r}_2. \tag{5.1}$$

One can also partition U into short and long-range portions as

$$U = U^{\mathrm{SR}} + U^{\mathrm{LR}}, \tag{5.2}$$

where U^{SR} is the short-range potential energy given for $r \leq r_{\mathrm{cut}}$ by

$$U^{\mathrm{SR}} = \sum_{i,j<i} u(r_{ij}), \tag{5.3}$$

and U^{LR} is the long-range portion of the energy.

Slab-based method approximate the long-range portion of the energy with the assumption that the average density profile varies only in the z direction. Using this assumption and the H contour, one can express the long-range portion of the local potential energy $u^{\mathrm{LR}}(z)$ (per atom or molecular site) as

$$u^{\mathrm{LR}}(z) = \frac{1}{2} \int_{r_{\mathrm{cut}}}^{\infty} u(r_2)\rho(z_2)\, d\mathbf{r}_2. \tag{5.4}$$

For simplicity, for the remainder of this chapter $u(r)$ corresponds to the LJ potential and all quantities are given in reduced LJ units. Janeček showed that one can explicitly integrate Eq. 5.4 for two directions using cylindrical coordinates as [76]:

$$u^{\mathrm{LR}}(z) = \int_{-\infty}^{\infty} w\left(z - z_2\right) \rho(z_2)\, dz_2 \tag{5.5}$$

where

$$w(x) = \begin{cases} 4\pi \left[\frac{1}{5} r_{\mathrm{cut}}^{-10} - \frac{1}{2} r_{\mathrm{cut}}^{-4} \right] & \text{for } x \leq r_{\mathrm{cut}} \\ 4\pi \left[\frac{1}{5} x^{-10} - \frac{1}{2} x^{-4} \right] & \text{for } x > r_{\mathrm{cut}} \end{cases}. \tag{5.6}$$

Because the density profile of the system is not known *a priori*, Janeček's method performs the integral in Eq. 5.5 numerically for each timestep using slabs as

$$u^{\mathrm{LR}}(z) = \sum_{k=1}^{n_k} w\left(z - z_k\right) \rho(z_k)\, \Delta z, \tag{5.7}$$

where Δz is the slab width, n_k is the number of slabs, and z_k is the location of the kth slab. Corresponding expressions for the long-range force and pressure tensor (similar to Eqs. 5.6 and 5.7) are also found in Ref. [76].

A couple of problems arise when Janeček's method is used. First, because this method does not account for multiple periodic images, errors are produced in local forces, energy, and pressure tensor at the ends of the simulation cell. This is illustrated when the method is applied to a homogeneous system. In this case, Janeček's method erroneously gives a non-constant energy correction and a non-zero long-range force [82]. Also, using finite-size slabs to integrate over the z_2 direction can produce additional error unless Δz is sufficiently small. On the other hand, summing over several hundred slabs at each timestep can substantially slow down the simulation.

5.3 An improved formulation of the slab-based method

Here we show a new formulation of the slab-based method for the LJ fluid called the *slab-based (SB) Ewald* method that has some advantages over Janeček's method. The essential steps in the SB Ewald method are as follows. One uses a Fourier series to fit the density profile and then integrates in all 3 directions to obtain a closed-form solution for the long-range energy, force, and pressure tensor. It is then necessary only to sum over constant Fourier coefficients at each timestep. Unlike Janeček's method, this new method includes all periodic images out to infinity using a formally exact integration in the z direction.

5.3.1 Energy

Using spherical coordinates, one can express Eq. 5.4 as

$$u^{\mathrm{LR}}(z) = \pi \int_{r_{\mathrm{cut}}}^{\infty} dr\, u(r)\, r^2 \int_0^{\pi} d\theta\, \rho\left[z + r\, \cos(\theta)\right]\, \sin(\theta)\,. \tag{5.8}$$

Using the following identity [71],

$$\int_0^\pi \sin(\theta)\, d\theta = \frac{1}{r} \int_{-r}^r dz' \, , \tag{5.9}$$

one can switch the azimuth angle θ in Eq. 5.8 with z', resulting in

$$u^{\mathrm{LR}}(z) = \pi \int_{r_{\mathrm{cut}}}^\infty dr\, u(r)\, r \int_{-r}^r dz' \, \rho\left(z + z'\right) \, , \tag{5.10}$$

where $z' = z_2 - z$.

One can fit the density profile using a Fourier series as

$$\rho(z) = A_0 + 2 \sum_{n=1}^\infty \left[A_n \cos\left(h_n z\right) + B_n \sin\left(h_n z\right) \right] \, , \tag{5.11}$$

where A_n and B_n are the Fourier coefficients (defined below), L_z is the length of the simulation cell in the z direction, and $h_n = 2\pi\, n / L_z$. In practice, this sum is truncated after n_{max} terms.

Fourier coefficients are given as

$$A_n = \frac{1}{V} \sum_{j=1}^{N_{\mathrm{p}}} \cos\left(h_n z_j\right) \, , \tag{5.12}$$

and

$$B_n = \frac{1}{V} \sum_{j=1}^{N_{\mathrm{p}}} \sin\left(h_n z_j\right) \, , \tag{5.13}$$

where N_{p} is the total number of particles, z_j is the position of the jth particle in the z direction, and V is the system volume. We note that $A_0 = \rho_{\mathrm{avg}}$, the average density of the system.

Using this Fourier fit of density, a closed-form solution of Eq. 5.4 can be obtained as

$$u^{\mathrm{LR}}(z) = -\frac{8\pi\, \rho_{\mathrm{avg}}}{3\left(r_{\mathrm{cut}}\right)^3} + \sum_{n=1}^{n_{\mathrm{max}}} U_n \left[A_n \cos\left(h_n z\right) + B_n \sin\left(h_n z\right) \right] \, , \tag{5.14}$$

where

$$U_n = -16\pi\, h_n^3 \left[\frac{\pi}{48} - \mathrm{Si}_5\left(h_n\, r_{\mathrm{cut}}\right) \right] , \qquad (5.15)$$

and

$$\mathrm{Si}_m(x) = \int_0^x \frac{\sin(x)}{x^m}\, dx , \qquad (5.16)$$

where m is an odd integer. We describe how to conveniently evaluate $\mathrm{Si}_m(x)$ below. Here we have only included the LJ dispersion term because the long-range correction of LJ repulsion term is usually negligible, at least for $r_{\mathrm{cut}} \geq 2.5\sigma$. One can see that the first term on the right-hand side of Eq. 5.14 (*i.e.*, for $n = 0$) is equivalent to the dispersion standard tail correction for the average system density ρ_{avg}.

The coefficients U_n depend only on L_z and r_{cut} and can be evaluated just once at the beginning of the simulation (unless the dimensions of the simulation cell change). In this manner, one simply needs to calculate the Fourier coefficients for the density profile and sum over lattice vectors according to Eq. 5.14 at each timestep. Fourier coefficients for density can also be averaged over multiple timesteps if desired.

5.3.1.1 Per-atom energy

Eq. 5.14 gives the long-range energy at any location in the z direction. However, if one is only interested in obtaining per-atom quantities, one can save computational time by storing per-atom Fourier coefficients $A_{n,j}$ and $B_{n,j}$ for the jth atom when computing total Fourier coefficients (Eqs. 5.12 and 5.13). Per-atom Fourier coefficients are given as

$$A_{n,j} = \frac{1}{V} \cos\left(h\, z_j\right) , \qquad (5.17)$$

and

$$B_{n,j} = \frac{1}{V} \sin(h \, z_j) . \tag{5.18}$$

Using Eqs. 5.14, 5.17 and 5.18, one can show that

$$u^{\mathrm{LR}}(z_j) = u_j^{\mathrm{LR}} = -\frac{8\pi \, A_0 A_{0,j} V}{3 \, (r_{\mathrm{cut}})^3} + V \sum_{n=1}^{n_{\max}} U_n \left(A_n A_{n,j} + B_n B_{n,j} \right) . \tag{5.19}$$

Storing per-atom Fourier coefficients and using Eq. 5.19 avoids the need to recompute the sine and cosine terms in Eq. 5.14, which can be more computationally efficient.

5.3.1.2 Total system energy

The total long-range potential energy of the system U^{LR} can be obtained be multiplying Eq. 5.14 by $\rho(z)$ and integrating over volume according to Eq. 5.1. This gives

$$U^{\mathrm{LR}} = -\frac{8\pi \, \rho_{\mathrm{avg}} \, N_{\mathrm{p}}}{3 \, (r_{\mathrm{cut}})^3} + V \sum_{n=1}^{n_{\max}} U_n \left(A_n^2 + B_n^2 \right) . \tag{5.20}$$

5.3.2 Force

The long-range force f^{LR} in the z direction (per atom or molecular site) is given as

$$f^{\mathrm{LR}}(z) = 2\pi \int_{r_{\mathrm{cut}}}^{\infty} dr \, \frac{d\, u(r)}{dr} \int_{-r}^{r} dz' \, z' \, \rho(z + z') . \tag{5.21}$$

Similar to the procedure used for energy, integrating Eq. 5.21 using a Fourier fit of density gives

$$f^{\mathrm{LR}}(z) = \sum_{n=1}^{n_{\max}} F_n \left[-A_n \sin(h_n z) + B_n \cos(h_n z) \right] , \tag{5.22}$$

where

$$F_n = 192\pi \, h_n^4 \left[\frac{\pi}{288} - \mathrm{Si}_7 \left(h_n \, r_{\mathrm{cut}} \right) + \mathrm{Ci}_6 \left(h_n \, r_{\mathrm{cut}} \right) \right] , \tag{5.23}$$

76

and

$$\mathrm{Ci}_m(x) = \int_0^x \frac{\cos(x)}{x^m} \, dx \, , \tag{5.24}$$

where m is an even integer. We describe how to conveniently evaluate $\mathrm{Ci}_m(x)$ below.

Eq. 5.21 gives the long-range force at any location z in the simulation cell. However, in MD simulations, one is frequently interested only in per-atom forces, which are needed to run the simulation. These can be expressed as

$$f^{\mathrm{LR}}(z_j) = f_j^{\mathrm{LR}} = V \sum_{n=1}^{n_{\max}} F_n \left[-A_n B_{n,j} + B_n A_{n,j} \right] . \tag{5.25}$$

5.3.3 Pressure

For the normal component of the pressure tensor using the H contour, the long-range correction is

$$P_{\mathrm{N}}^{\mathrm{LR}}(z) = -\pi \, \rho(z) \int_{r_{\mathrm{cut}}}^{\infty} dr \, \frac{d \, u(r)}{dr} \int_{-r}^{r} dz' \, (z')^2 \, \rho \left(z + z' \right) . \tag{5.26}$$

Expressing $\rho(z)$ as a Fourier series and performing the integrations in Eq. 5.26 gives

$$P_{\mathrm{N}}^{\mathrm{LR}}(z) = -\frac{16\pi \, \rho_{\mathrm{avg}} \, \rho(z)}{3 \left(r_{\mathrm{cut}} \right)^3} + \rho(z) \sum_{n=1}^{n_{\max}} N_n \left[A_n \cos \left(h_n \, z \right) + B_n \sin \left(h_n \, z \right) \right] , \tag{5.27}$$

where

$$N_n = -96\pi \, h_n^3 \left[\frac{\pi}{72} - \mathrm{Si}_5 \left(h_n \, r_{\mathrm{cut}} \right) + 2 \, \mathrm{Si}_7 \left(h_n \, r_{\mathrm{cut}} \right) - 2 \, \mathrm{Ci}_6 \left(h_n \, r_{\mathrm{cut}} \right) \right] . \tag{5.28}$$

For the tangential component of the pressure tensor using the H contour, the long-range correction is

$$P_{\mathrm{T}}^{\mathrm{LR}}(z) = -\frac{\pi}{2}\,\rho(z) \int_{r_{\mathrm{cut}}}^{\infty} dr\,\frac{d\,u(r)}{dr} \int_{-r}^{r} dz'\,\left(r^2 - z'^2\right) \rho\left(z + z'\right) . \tag{5.29}$$

Integrating Eq. 5.29 gives

$$P_{\mathrm{T}}^{\mathrm{LR}}(z) = -\frac{16\pi\rho_{\mathrm{avg}}\,\rho(z)}{3\left(r_{\mathrm{cut}}\right)^3} + \rho(z) \sum_{n=1}^{n_{\mathrm{max}}} T_n \left[A_n \cos\left(h_n\,z\right) + B_n \sin\left(h_n\,z\right)\right] , \tag{5.30}$$

where

$$T_n = -96\pi\,h_n^3 \left[\frac{\pi}{288} - \mathrm{Si}_7\left(h_n\,r_{\mathrm{cut}}\right) + \mathrm{Ci}_6\left(h_n\,r_{\mathrm{cut}}\right)\right] . \tag{5.31}$$

Per-site and volume-averaged quantities for P^{N} and P^{T} can be obtained in a similar manner to that described above for energy. We note that the total long-range contribution to surface tension γ^{LR} is given by

$$\gamma^{\mathrm{LR}} = \frac{L_z}{2} \sum_{n=1}^{n_{\mathrm{max}}} \left(N_n - T_n\right)\left(A_n^2 + B_n^2\right) . \tag{5.32}$$

5.3.4 Evaluation of trigonometric integrals

Using the power series expansion of $\sin(x)$, one can evaluate $\mathrm{Si}_m(x)$ (for $x > 0$ and odd integer m only) as

$$\mathrm{Si}_m(x) = \sum_{k=0}^{\infty} \frac{(-1)^k\,x^{2k+2-m}}{(2k+1)!\,(2k+2-m)} . \tag{5.33}$$

Similarly, using the power series expansion of $\cos(x)$, one can evaluate $\mathrm{Ci}_m(x)$ (for $x > 0$ and even integer m only) as

$$\mathrm{Ci}_m(x) = \sum_{k=0}^{\infty} \frac{(-1)^k\,x^{2k+1-m}}{(2k)!\,(2k+1-m)} . \tag{5.34}$$

In practice, using 75 terms provided sufficient accuracy for $x \leq 30$. To prevent numerical instabilities, for $x > 30$ one can use asymptotic expansions instead. These expansions are

$$
\begin{aligned}
\mathrm{Si}_m(x) \quad = \quad & \frac{\sin\left(\frac{\pi}{2}m\right)}{(m-1)!}\frac{\pi}{2} - \frac{\cos(x)}{(m-1)!}\sum_{k=0}^{k_{\max}}(-1)^k\,(2k-1+m)!\,x^{-(2k+m)} \\
& - \frac{\sin(x)}{(m-1)!}\sum_{k=0}^{k_{\max}}(-1)^k\,(2k+m)!\,x^{-(2k+1+m)}\,,
\end{aligned}
\tag{5.35}
$$

and

$$
\begin{aligned}
\mathrm{Ci}_m(x) \quad = \quad & \frac{\cos\left(\frac{\pi}{2}m\right)}{(m-1)!}\frac{\pi}{2} - \frac{\sin(x)}{(m-1)!}\sum_{k=0}^{k_{\max}}(-1)^k\,(2k-1+m)!\,x^{-(2k+m)} \\
& - \frac{\cos(x)}{(m-1)!}\sum_{k=0}^{k_{\max}}(-1)^k\,(2k+m)!\,x^{-(2k+1+m)}\,,
\end{aligned}
\tag{5.36}
$$

Eqs. 5.35 and 5.36 can be obtained by a repeated integration by parts procedure. We used $k_{\max} = 10$.

5.4   Preliminary results

In order to test the proposed methods, we used the snapshot of an LJ fluid shown in Figure 5.1. The temperature of this system was $T^* = 2.0$ and the average density was $\rho^* = 0.4$. An external potential was applied to the simulation in the z direction.

   As shown in Figure 5.2, different long-range correction methods were tested by plotting the total system energy vs r_{cut} for one configuration (see Figure 5.1). Both the full Ewald sum and the SB Ewald used $h_{\mathrm{cut}} = 23.15\,\sigma^{-1}$, and the full Ewald sum also used $\alpha = 3.0\,\sigma^{-1}$. If we assume that the true U^{tot} of the system is given by the full Ewald sum and $r_{\mathrm{cut}}^* = 6.0$, then for $r_{\mathrm{cut}}^* = 2.5$, the magnitude of the error in the full Ewald sum (in reduced units) was 0.41 (0.011 % of the true value), while that of the SB Ewald sum was 3.5 (0.09 % of the true
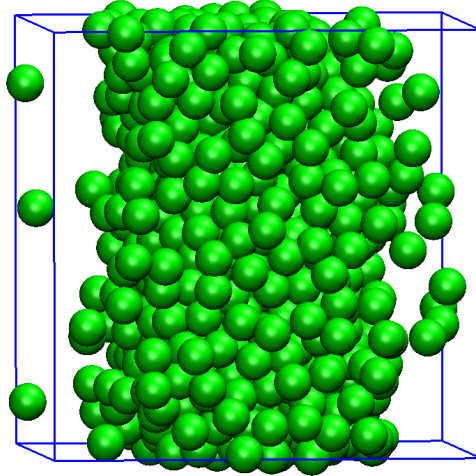
Figure 5.1: Snapshot of an LJ fluid used to test the SB-Ewald sum.

value). When using the standard LRC and $r_{cut}^* = 2.5$, the error was 75 (2.0 % of the true value), and for no long-range correction and the same cutoff, the error was 289 (7.6 % of the true value). We also note that using only the standard LRC for energy or no LRC neglects the long-range force needed to obtain the correct density profile. The SB Ewald sum allows one to use a much shorter r_{cut} than when using the standard LRC evaluated at the average system density. For lattice vector cutoff value used in this test, the traditional Ewald sum required 261652 lattice vectors, while the SB Ewald sum required only 50 lattice vectors.

We note that because the SB Ewald sum uses a sharp damping term and is only long-ranged, the rate of convergence of the SB Ewald sum *vs* number of lattice vectors is slower than that of the traditional Ewald sum, so for a given accuracy the SB Ewald sum will require a larger h_{cut} than the traditional Ewald sum. However, we still expect the SB Ewald sum method to be faster than the traditional Ewald sum for reasonable accuracy values. One could also modify the SB Ewald sum to use smooth damping and therefore increase the rate of convergence (similar to the traditional Ewald sum). One could also increase the speed of the SB Ewald sum by using fast Fourier transform (FFTs) methods such as the particle-particle particle mesh (P3M) method [101].
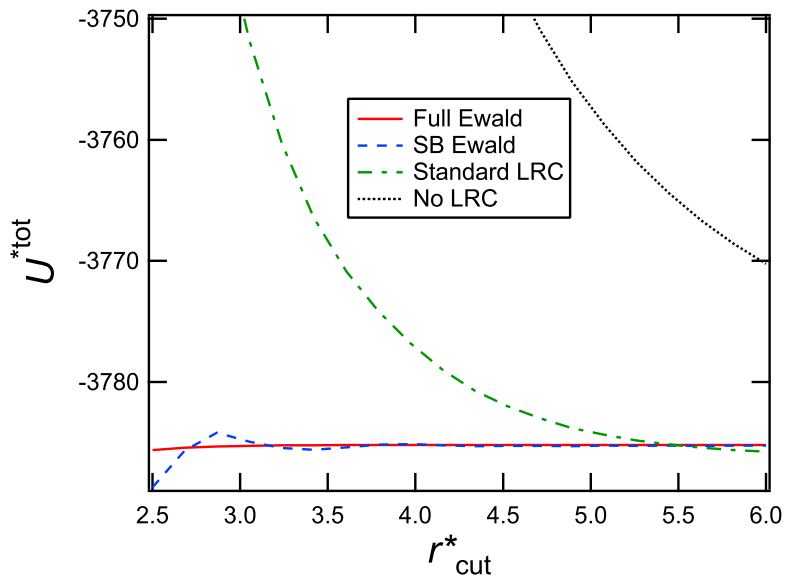
Figure 5.2: Total system energy for the configuration shown in Figure 5.1 *vs* cutoff using different long-range correction methods.

5.5 Conclusion

In this chapter, a new Ewald sum method called SB Ewald has been developed for LJ dispersion interactions, which is more efficient than the full lattice sum when the average density of the system varies only in one direction. The SB Ewald sum computes the long-range energy, force, and pressure tensor. The SB Ewald sum can readily be extended to LJ mixtures and multi-site molecules that use dispersion interactions, such as long-chain alkanes, as well as other intermolecular potentials of the form $A\,r^{-n}$, where $n > 3$ and A is a constant.

Chapter 6

Multi-component mixtures

6.1 Introduction

In this chapter we extend the CPP method to species chemical potential prediction for multi-component mixtures. For mixtures, chemical potentials are frequently expressed using activity coefficients with a pure-component reference state for each species. In this manner, activity coefficients essentially give a dimensionless chemical potential in excess of a reference state.

Several methods exist to obtain activity coefficients from molecular simulations. For example, one can use osmotic molecular dynamics (OMD) [28–30], Kirkwood-Buff (KB) solution theory [102, 103], or particle insertion methods such Widom's [7, 8, 104] described previously in Chapter 3. For ionic systems however, using Widom's method to determine the chemical potential is even more complicated because inserting a single ion violates electroneutrality [105].

The CPP method for multi-component systems is similar to the pure-component case but can use separate external potentials for each species in the simulation. In this manner, one can obtain activity coefficients for each species for a wide range of composition points in a single simulation. For example, Figure 6.1 shows a snapshot of CPP simulation 1L (described below), a binary Lennard-Jones mixture in which $\sigma_2 = 2\sigma_1$. As shown in Figure 6.2, the external field on species 1 forces the type 1 particles towards the center of the simulation cell, while the field on species 2 forces the type 2 particles away from the center. We note
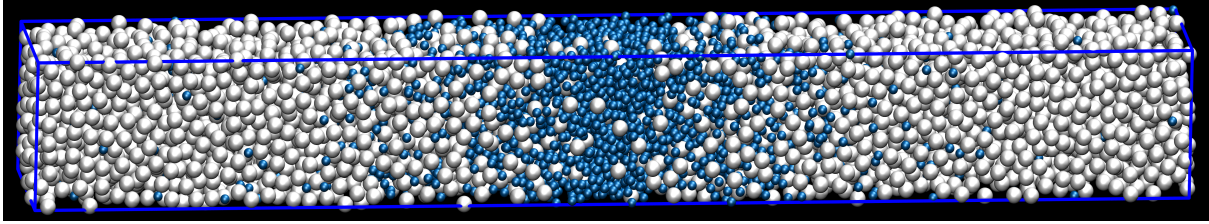
Figure 6.1: Snapshot of CPP simulation 1L. Species 1 particles (concentrated near the center of the cell) are half the size of species 2 particles.

that results for LJ binary mixtures in this chapter are given in reduced LJ units using the LJ parameters of species 1.

In this chapter, we develop the working equations for the CPP method applied to multi-component mixtures. The inhomogeneous correction methods given in Chapter 3 are also extended to mixtures, though a full implementation of these methods was beyond the scope of this work. Because activity coefficients are normally given at constant pressure, we discuss methods of reducing and correcting for pressure variation that arises due to the external potentials applied to the system. We also describe a method to reduce equilibrium time. We present preliminary results for several different binary LJ mixtures and compare to data from OMD, KB, and Widom's methods reported previously in literature.

6.2   Development of the CPP method for multi-component systems

For a system at equilibrium, the total chemical potential $\mu_i^{\text{tot}}(\mathbf{r})$ for each species i is equal at all locations inside the simulation cell. For a system in which average properties vary only in the z direction, this can be expressed as

$$\mu_i^{\text{tot}}(z) = \mu_i^{\text{tot}}(z_{\text{ref}}),\tag{6.1}$$

where z_{ref} refers to a reference location in the simulation (for example, where there is pure species i).
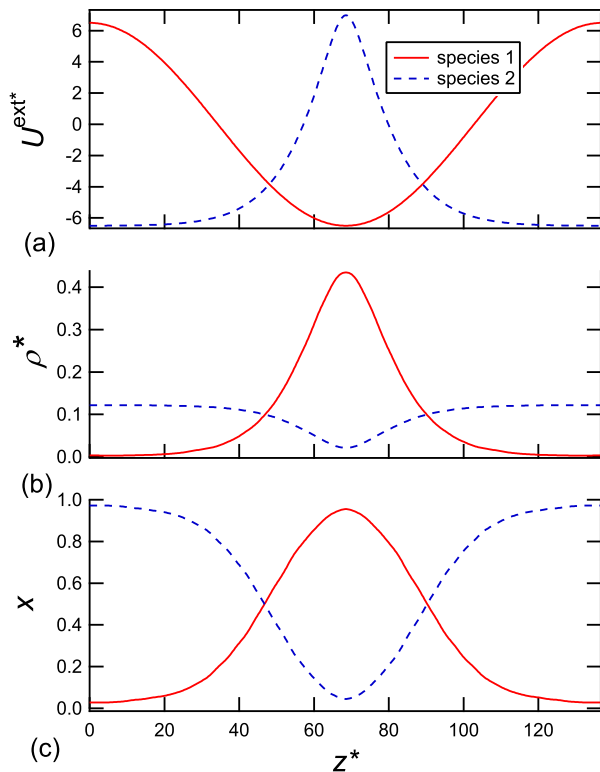
Figure 6.2: (a) External potential applied to species and resulting (b) density profiles and (c) mole fractions.

Similar to the pure-component case, the total chemical potential can be partitioned as

$$\mu_i^{\text{tot}}(z) = U_i^{\text{ext}}(z) + \mu_i^0(z) + \mu_i^{\text{IH}}(z), \tag{6.2}$$

where $U_i^{\text{ext}}(z)$ is the periodic external potential acting on species i, $\mu_i^0(z)$ is the homogeneous chemical potential, and $\mu_i^{\text{IH}}(z)$ is the excess chemical potential due to the inhomogeneity of the system [106]. An expression similar to Eq. 6.2 can also be written for z_{ref}. Solving Eq. 6.2 for the desired $\mu_i^0(z)$ gives

$$\mu_i^0(z) = -U_i^{\text{ext}}(z) - \mu_i^{\text{IH}}(z) + \mu_i^{\text{tot}}(z). \tag{6.3}$$

One can also separate $\mu_i^0(z)$ into both a standard-state chemical potential (independent of composition) and a composition-dependent part:

$$\mu_i^0(z) = g_i + R_\mathrm{g}\, T \, \ln[x_i(z)\, \gamma_i(z)]\,, \tag{6.4}$$

where g_i is the pure-component Gibbs energy used as a reference state, R_g is the universal gas constant, T is the system temperature, x_i is the mole fraction of species i, and γ_i is the activity coefficient. Here we assume that the system temperature and pressure are constant. We discuss the case of pressure variation below.

Subtracting Eq. 6.3 written for z_ref from Eq. 6.3 written for z, combining the result with Eq. 6.4, and solving for $\ln\gamma_i(z)$ gives

$$\ln\gamma_i(z) = \frac{\mu_i^0(z) - \mu_i^0(z_\mathrm{ref})}{R_\mathrm{g}\, T} + \ln\left[\frac{x_i(z_\mathrm{ref})}{x_i(z)}\right] + \ln\gamma_i(z_\mathrm{ref})\,. \tag{6.5}$$

In the CPP method, the mole fractions x_i are measured from the simulation. If the composition at z_ref is nearly pure species i, then $\ln\gamma_i(z_\mathrm{ref})$ is nearly zero and can be neglected, and one only needs to determine $\mu_i^0(z)$ to obtain $\ln\gamma_i(z)$ using Eq. 6.5.

Combining Eqs. 6.3 and 6.5 gives

$$
\begin{aligned}
\ln\gamma_i(z) \;=\; & \frac{U_i^\mathrm{ext}(z_\mathrm{ref}) - U_i^\mathrm{ext}(z)}{R_\mathrm{g}\, T} + \ln\left[\frac{x_i(z_\mathrm{ref})}{x_i(z)}\right] \\
& + \frac{\mu_i^\mathrm{IH}(z_\mathrm{ref}) - \mu_i^\mathrm{IH}(z)}{R_\mathrm{g}\, T} + \ln\gamma_i(z_\mathrm{ref})\,.
\end{aligned}
\tag{6.6}
$$

In the CPP method, $U_i^\mathrm{ext}(z)$ is fixed, so given $\mu_i^\mathrm{IH}(z)$, one can obtain $\ln\gamma_i(z)$ using Eq. 6.6. We note that using z_ref has allowed us to eliminate the standard-state chemical potentials g_i (*i.e.*, we are measuring a difference in activity coefficients).

6.2.1   Obtaining homogeneous properties

Obtaining homogeneous properties from multi-component mixtures is similar to the pure-component case described in Chapter 3. In fact, all 3 inhomogeneous correction methods

given in Chapter 3 can be extended to mixtures as described below. However, a full implementation of the inhomogeneous correction methods for mixtures was beyond the scope of the project.

For example, the van der Vaals density gradient theory predicts the inhomogeneous chemical potential is equal to

$$\mu_i^{\text{IH}} = -\sum_j \nabla \cdot (c_{ij} \nabla \rho_j) + \tfrac{1}{2} \sum_{j,k} \frac{\partial c_{jk}}{\partial \rho_i} \nabla \rho_j \cdot \nabla \rho_k \,, \tag{6.7}$$

where c_{ij} are the influence parameters and ρ_i is the local density of species i. The influence parameters may be approximated using the direct correlation functions of the homogeneous fluid [34, 106].

Eq. 6.7 shows that decreasing the density gradients will decrease the inhomogeneous term μ_i^{IH}. Therefore, the simplest method to obtain $\ln \gamma_i(z)$ from Eq. 6.6 is to increase the length of the simulation cell in the z direction until μ_i^{IH} can be neglected. One can alternatively approximate $\mu_i^{\text{IH}}(z)$ using Eq. 6.7 and $\ln \gamma_i(z)$ from Eq. 6.6. Similar to the pure-component case, one can also use the Triezenberg-Zwanzig equation for multi-component mixtures [34].

One can also use the pressure tensor method to approximate the homogeneous pressure and resulting chemical potential for mixtures. For multi-component systems, one can divide the total pressure tensor $\mathbf{P}$ into contributions from each individual species as

$$\mathbf{P} = \sum_i \mathbf{P}_i \,. \tag{6.8}$$

For the IK contour, a gradient expansion in density gradients [34] (see Appendix C) predicts that

$$P_i^0(z) = \frac{3}{2} P_{\text{T},i}(z) - \frac{1}{2} P_{\text{N},i}(z) \,. \tag{6.9}$$

This is is similar to the pure-component case given in Eq. 3.23. In addition, mechanical stability requires that [34, 48]

$$\nabla \cdot \mathbf{P}_i = -\rho_i \nabla U_i^{\text{ext}} + \mathbf{B}_i \,, \tag{6.10}$$

where $\mathbf{B}_i$ is termed the asymmetric force and is subject to

$$\sum_i \mathbf{B}_i = 0 \,. \tag{6.11}$$

For our 1-D system, mechanical stability becomes

$$\frac{dP_{\text{N},i}(z)}{dz} = \rho_i(z) \, f_i^{\text{ext}}(z) + B_{\text{N},i}(z) \,, \tag{6.12}$$

where $f_i^{\text{ext}}(z) = -dU_i^{\text{ext}}(z)/dz$ is the external force acting on species i and $B_{\text{N},i}(z)$ is the normal component of asymmetric force.

Gradient theory also predicts that [48]

$$\frac{dP_i^0(z)}{dz} - B_{\text{N},i}(z) = \rho_i(z) \frac{d\mu_i^0(z)}{dz} \,. \tag{6.13}$$

Dividing both sides of Eq. 6.14 by $\rho_i(z)$ and integrating over z from z_{ref} to z gives

$$\mu_i^0(z) = \int_{z_{\text{ref}}}^z \frac{1}{\rho_i(z)} \frac{dP_i^0(z)}{dz} dz - \int_{z_{\text{ref}}}^z \frac{B_{\text{N},i}(z)}{\rho_i(z)} dz + \mu_i^0(z_{\text{ref}}) \,. \tag{6.14}$$

We note that summing Eq. 6.14 over all species and using Eqs. 6.8 and 6.11 satisfies the Gibbs-Duhem equation:

$$\frac{dP^0(z)}{dz} = \sum_i \rho_i(z) \frac{d\mu_i^0(z)}{dz} \,, \tag{6.15}$$

confirming that Eq. 6.14 is thermodynamically valid. One can therefore obtain $P_i^0(z)$ from the local pressure tensor using Eq. 6.9, $\mu_i^0(z)$ from Eq. 6.14, and $\ln \gamma_i(z)$ using Eq. 6.5.

$B_{\mathrm{N},i}(z)$ can be obtained from a virial-type expression as given by Davis [34] or from Eq. 6.12, in which case the IK contour should be used for $P_{\mathrm{N},i}(z)$ (as described in Chapter 4) because Eq. 6.12 is based on mechanical stability.

6.2.2 Controlling pressure variation

Activity coefficients are normally given as a function of composition for a constant pressure. Experimentally, activity coefficients also show a weak dependence on pressure, which is usually ignored. However, due to the external potential in CPP simulations, very large variations in pressure are possible, making it necessary to correct for or reduce the variation in pressure.

Pressure variation across the simulation cell can be reduced by adjusting the external potential of one species to maintain constant normal pressure. For a system of N_{c} species, this can be accomplished by using the first $N_{\mathrm{c}} - 1$ component's fields to fix the system composition and the remaining field to control the system pressure.

For multi-component systems, combining Eqs. 6.11 and 6.12 shows the total normal pressure is related to the external force according to

$$\frac{dP_{\mathrm{N}}(z)}{dz} = \sum_{i=1}^{N_{\mathrm{c}}} f_i^{\mathrm{ext}}(z)\rho_i(z) \,. \tag{6.16}$$

Setting Eq. 6.16 equal to zero and solving for the external force on species N gives

$$f_{N_{\mathrm{c}}}^{\mathrm{ext}}(z) = -\frac{1}{\rho_{N_{\mathrm{c}}}(z)} \left[\sum_{i=1}^{N_{\mathrm{c}}-1} f_i^{\mathrm{ext}}(z)\rho_i(z) \right] \,. \tag{6.17}$$

As shown in Figure 6.2, species 1 uses a sinusoidal external potential, while the external potential of species 2 is adjusted to maintain constant normal pressure.

However, the homogeneous pressure depends on both P_{N} and P_{T} as shown by Eq. 3.23. As shown below, if $P_{\mathrm{T}}(z)$ varies due to surface tension, then $P^0(z)$ can also vary even though

$P_N(z)$ is held constant. In this case and assuming no phase-splitting, increasing L_z will reduce surface tension and the resulting variation in $P^0(z)$ if $P_N(z)$ is constant.

One can also use partial molar volumes $\overline{V_i}$ to correct for pressure variations as

$$\frac{d\ln(\gamma_i)}{dP} = \frac{\overline{V_i}}{R_g T}, \tag{6.18}$$

although pressure variations make obtaining partial molar volumes from a single CPP simulation difficult. Instead, one can use the pure-component molar volume V_i as a first-order approximation for $\overline{V_i}$. When P and T are constant, one can obtain partial molar volumes using derivatives of the total molar volume with respect to composition.

6.2.3 Fast equilibration method

As mentioned previously, elongating the simulation cell in the z direction reduces inhomogeneity and pressure variations, assuming no phase-splitting and the normal pressure is held constant. However, equilibration for multi-component CPP simulations is much slower than the pure-component case because molecules must move by diffusion instead of convection. For large systems or systems greatly elongated in the z direction, starting from a uniform composition and allowing particles to diffuse until equilibrium is reached is very computationally inefficient. Though not done in this work, one could use a fast equilibration method to help overcomes these difficulties.

The basic idea of the fast equilibration method is to use the density profile obtained from a small system (one that equilibrates quickly) as the starting point for a larger system. First, a small system (for example, 1000 particles in a cubic simulation cell) is equilibrated and the resulting compositions are fit using a Fourier series. The Fourier series is used to adjust the starting position of molecules in a larger simulation (2000 particles with $L_z = 2\,L_x = 2\,L_y$). This simulation is equilibrated, and resulting compositions are again fit using a Fourier series. This method is repeated for intermediate system sizes until the desired system size

is reached. One could also use a shorter cutoff or a larger timestep during the early stage of the equilibration.

6.3   Simulation details

In order to test the proposed methods, we used several different binary LJ mixtures. Implementing the inhomogeneous correction methods for mixtures described previously was beyond the scope of this project. However, the effect of inhomogeneity can be estimated by increasing the length of the simulation cell in the z direction while holding the field strength and average density constant, which decreases inhomogeneity. We therefore used two different simulation geometries, one much longer in the z direction.

For simplicity, long-range corrections were also neglected. In this case it is inconvenient to use an Ewald sum because LJ binary mixture simulations reported previously in literature frequently used the Lorentz-Berthelot (LB) combining rule, while the Ewald sum method as described in Chapter 4 is more compatible with and commonly uses a geometric combining rule. An Ewald sum can be extended to include LB combining rules [89], but this requires significant extra computation and was beyond the scope of the project. However, one can estimate the effect of truncation of the potential by changing r_{cut}, so the two different simulation geometries also used different cutoff radii.

Table 6.1 gives parameters for the LJ binary mixtures shown in this work, where $T^* = k_{\text{B}} T / \varepsilon_1$ and $P^* = P \sigma_1^3 / \varepsilon_1$. The strength of the external potential for species 1 is given in Table 6.1, while the external force for species 2 was given by Eq. 6.17, using an average density profile updated every 1000 timesteps in order to run the simulation, and averaged over the entire course of the simulation for property prediction.

As described previously, each mixture listed in Table 6.1 was run using two different geometries, *long* and *big.* The long (L) geometry used a simulation cell greatly elongated in the z direction, with $L_z = 8\,L_x = 8\,L_y$, and was run for 10^6 timesteps (not including

Table 6.1: Parameters for the binary LJ mixture simulations.

Name	T^*	P^*	σ_2/σ_1	$\varepsilon_2/\varepsilon_1$	$\triangle U^*_{\max}$
1	3	2.5	2	1	13.0
2	2	0.52	2	1	8.0
3	2	1.755	1	2	2.2
4	2	1.2	1.5	2	4.6
5	2	0.5	2	2	10.0

equilibration). The big (B) geometry used $L_z = 2\,L_x = 2\,L_y$, and was run for 5×10^5 timesteps (not including equilibration). All simulations used 8000 particles (half species 1 and half species 2) and $r_{\mathrm{cut}} = L_x/2$. An NPT ensemble was used to obtain the average system pressure given in Table 6.1 using a standard LRC for pressure based on the average composition of the system. Resulting density profiles were fit for each species using a Fourier series and were used to predict activity coefficients for the range of composition in the simulation. Activity coefficient results for $x_i < 0.1$ were truncated due to noise in the data and then fit using the Wilson equation to ensure the data satisfied the Gibbs-Duhem equation. For species 1, $z_{\mathrm{ref}} = L_z/2$, while for species 2, $z_{\mathrm{ref}} = 0$ (see Figure 6.2c). For all simulations it is assumed that $\ln \gamma_i(z_{\mathrm{ref}}) = 0$ because $x_i(z_{\mathrm{ref}})$ was small (*i.e.* nearly pure species i), except for mixture 3, in which $\ln \gamma_1(z_{\mathrm{ref}}) = 0.04$ because $x_1(z_{\mathrm{ref}})$ was comparatively large.

6.4 Preliminary simulation results and discussion

Preliminary results for the LJ binary mixtures are compared to results obtained using OMD and Kirkwood-Buff (KB) methods [30] as well as results using Widom's method [104]. In theory, one can also use a pure-component EOS, but it is necessary to use approximate
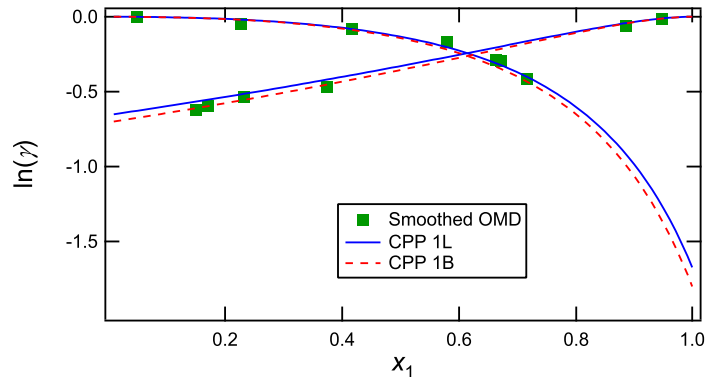
Figure 6.3: CPP results for LJ binary mixture 1.

mixing rules such as the VdW one-fluid theory [73]. We attempted to use the VdW one-fluid mixing rules with the LJ EOS, but results didn't agree with the OMD and KB results, perhaps because the binary LJ systems studied here are very non-ideal.

In order to better compare results from the OMD, KB, and Widom methods to those of the CPP method, we calculate the root-mean-square (RMS) error using all of the results given previously in literature (OMD, KB, or Widom) *vs* CPP results for the same composition points for each mixture.

Figure 6.3 shows the results of mixture 1, in which the LJ size parameter for species 2 is twice that of species 1 (see Table 6.1 and Figure 6.1). For mixture 1L, the RMS error of the CPP method compared to the OMD method was 0.039, and for mixture 1B it was 0.032. Part of this error is due to disagreement between CPP and OMD for γ_1 at $x_1 = 0.671$ as seen in Figure 6.3.

Mixture 2 is similar to mixture 1 but is at lower pressure and temperature. Figure 6.4 compares CPP results with those from the KB and OMD methods. For mixture 2L, the RMS error was 0.054, and for mixture 2B it was 0.052. Comparing Figures 6.3 and 6.4 shows that activity coefficients for this mixture aren't too sensitive to changes in temperature and pressure.

Figure 6.5 shows the results of mixture 3, in which the LJ energy parameter for species 2 is twice that of species 1. For mixture 3L, the RMS error was 0.0623, while for mixture
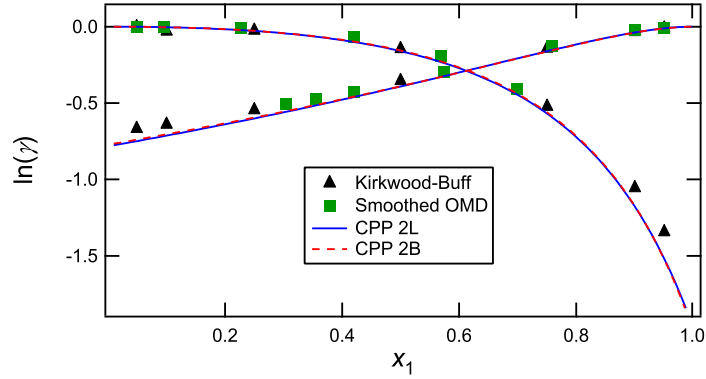
Figure 6.4: CPP results for LJ binary mixture 2.
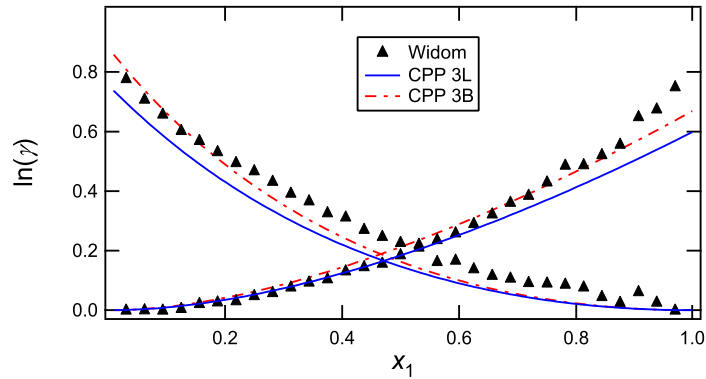
Figure 6.5: CPP results for LJ binary mixture 3.

3B it was 0.0393. For this mixture, $\ln \gamma_i(z)$ is also positive, unlike the previous mixtures. The 3B simulation produces less error than the 3L simulation, which could suggest that the shorter cutoff radius in the 3L simulation is not adequate or that the 3L simulation has not yet fully reached equilibrium.

Figure 6.6 shows the results of mixture 4, in which the both LJ parameters for species 2 are larger than that of species 1. For mixture 4L, the RMS error was 0.062, while for mixture 4B it was 0.0387, which is comparable to mixture 3, but results but also seem to show more of a systematic bias. Similar to mixture 3, the 4B simulation gives less error than the 4L simulation.
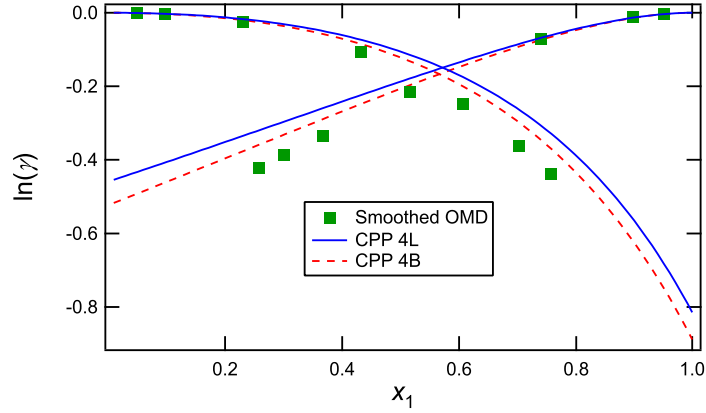
Figure 6.6: CPP results for LJ binary mixture 4.
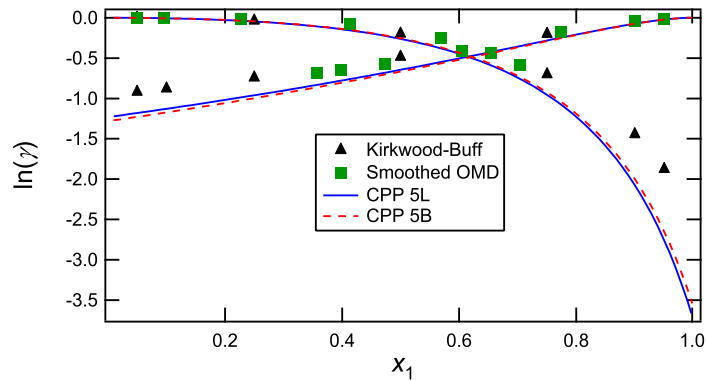
Figure 6.7: CPP results for LJ binary mixture 5.

Figure 6.7 shows the results of mixture 5, in which the both LJ parameters for species 2 are double that of species 1. For mixture 5L, the RMS error was 0.27, which for mixture 5B, it was 0.24. The RMS error for this mixture is much higher than the previous mixtures, and CPP results also seem to show a systematic bias.

Plotting P_N, P_T, and P^0 for mixture 5 shows that the normal pressure is fairly constant, but P_T and P^0 varies significantly with position z due to surface tension. The maximum range of variation for P_N was 0.0074, while for P_T it was 0.059 (7.9 times as high as P_N), and for P^0 it was 0.088 (12 times as high as P_N). This means that the activity coefficients for this simulation are not given at constant pressure, which is a possible source of error in the CPP results.
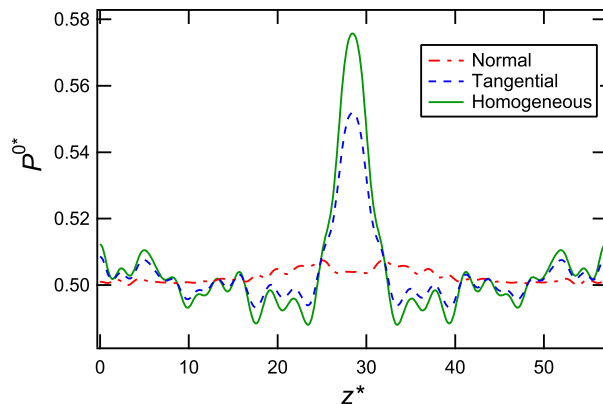
Figure 6.8: Pressure variation for mixture 5B.

As described above, partial molar volumes are needed to correct for pressure variations in activity coefficients but are difficult to obtain using CPP simulations. However, a first-order correction for pressure variation can be obtained by using the pure-component molar volume instead. We used the LJ EOS to obtain the pure-component volume as a function of pressure and computed the pressure correction. However, this correction turned out be be small.

Another potential sources of error is neglecting the inhomogeneous corrections. However, comparing the 5L and 5B simulations shows that elongating the system in the z direction has little effect. Neglecting long-range corrections could also affect results, but the 5B simulation uses a much larger cutoff radius than the 5L simulation with little effect on the results. We also used the VdW one-fluid mixing rules to confirm that no state points in mixture 5 were part of a liquid-vapor two-phase region, so the source of the disagreement between the CPP method and OMD remains unclear. Including a more sophisticated inhomogeneous or long-range correction may help. Alternatively, instead of using a single simulation to obtain the full composition range (pure species 1 to pure species 2), one could use multiple simulations to greatly reduce inhomogeneity. For all five mixtures, the "big" geometry produced less error than the "long" geometry. This could mean that the shorter cutoff radius in the "long" geometry is not adequate or that the simulations using the "long" geometry have not yet fully reached equilibrium.

6.5   Conclusion

In this chapter, we extend the CPP method for multi-component systems. A separate external field is applied to each species allowing one to obtain activity coefficients for each species over a wide range of compositions in a single simulation. Methods for approximating the inhomogeneous correction term are given. Constant normal pressure is maintained by adjusting the external potential of one of the species. Preliminary results for five different LJ binary mixtures show the correct trend when compared to data reported previously in literature, but some CPP results also have a systematic bias. We tried including a first-order correction for pressure variation, varying the length of the system, and varying the cutoff radius, but this did not completely resolve the bias. Including a more sophisticated inhomogeneous or long-range correction may help.

Chapter 7

Predicting critical parameters

In this chapter we review existing methods to predict fluid critical properties using molecular simulations and suggest a few ways in which the CPP method could be used to predict critical points. We also show preliminary results for the LJ fluid. A full implementation of the methods presented in this chapter was beyond the scope of the project. However, this topic is included in order to assist potential future researchers.

7.1   Introduction

The critical point of a fluid gives important thermodynamic information about the fluid. For example, the law of corresponding states allows one to use a reference fluid to predict thermodynamic properties for another fluid using the reduced temperature $T_\mathrm{r} = T/T_\mathrm{c}$ and reduced pressure $P_\mathrm{r} = P/P_\mathrm{c}$, where T_c is the critical temperature and P_c is the critical pressure. Many equations of state also use reduced temperatures and pressures for property prediction.

Several methods have been developed to predict critical points using molecular simulations. Most commonly, coexisting (binodal) densities of the fluid are predicted for temperatures close to the critical point and then scaling laws are used to extrapolate to the critical temperature and density (*i.e.* where the vapor and liquid binodal densities become equal).

Binodal densities can be determined by several different methods. For example, one can use the GEMC method, which avoids the formation of an interface between the two

phases. The NPT-plus-test-particle method [107, 108] and corresponding NVT-plus-test-particle method [109, 110] use molecular simulations with a particle insertion method such as Widom's [7, 8] to determine chemical potential *vs* pressure curves for both liquid and vapor phases. The coexisting densities correspond to where these curves intersect.

One can also directly simulate liquid-vapor phase equilibria using two-phase molecular simulations by simply simulating using an average system density corresponding to the two-phase region and allowing the system to phase-split and equilibrate [80, 94]. Bulk vapor and liquid densities are averaged to obtain the binodal densities. Unlike GEMC, two-phase molecular simulations form an interface between the liquid and vapor phases.

Normally it is difficult to maintain a stable interface as one approaches the critical point, but a more sophisticated two-phase method has been developed by Fern *et al.* [111] and Patel *et al.* [112]. In this method, it is not necessary to form a well-defined vapor-liquid interface. Instead, single-phase liquid and vapor simulations are used in conjunction with two-phase simulations as a self-consistency check, which allows one to estimate binodal densities very close to the critical point.

The multiple histogram re-weighting (MHR) method [113, 114] can also be used to determine coexisting densities. This method uses the fact that a single simulation can give information about nearby state points. Histograms from multiple simulations are combined to enhance statistics [115]. In order to predict phase coexistence properties, histograms for various liquid and vapor states are combined. It is also necessary to bridge between liquid and vapor states, which can be accomplished by performing an additional simulation near the critical point [116].

7.2   Finite-size scaling

Certain difficulties arise when one attempts to simulate fluids very close to the critical point. As one approaches the critical point, the correlation length diverges, which also means that

the length scale of the fluctuations of the fluid goes to infinity. Because molecular simulations are of finite size, all fluctuations greater than the size of the simulation cell are suppressed, which can bias the results. These fluctuations also make it difficult to form a stable interface close to the critical point [5]. Similarly, when the GEMC method is used, the two phases may frequently swap back and forth between the two simulation cells [5].

One method to reduce finite-size effects is to use universal scaling laws and critical exponents. For temperatures close to the critical point, the difference in coexisting densities is expected to scale as

$$\rho_{\mathrm{l}} - \rho_{\mathrm{v}} = A \left(T - T_{\mathrm{c}} \right)^{\beta} , \qquad (7.1)$$

where ρ_l is the liquid binodal density, ρ_v is the vapor liquid density, A is an adjustable parameter determined from the fit of the data, and β is the universal critical exponent [117]. For three-dimensional systems, where $\beta \simeq 0.32$ [112]. In addition, the law of rectilinear diameters [118] can also be used:

$$\tfrac{1}{2} \left(\rho_{\mathrm{l}} + \rho_{\mathrm{v}} \right) = \rho_{\mathrm{c}} + B \left(T - T_{\mathrm{c}} \right) , \qquad (7.2)$$

where B is an adjustable parameter determined from the fit of the data, and ρ_{c} is the critical density. In this manner, coexisting densities at different temperatures below the critical point (where finite-size effects are expected to be small) are determined from simulation and then fit using Eqs. 7.1 and 7.2. One then extrapolates to the critical point using the fit.

One can also use systems of different sizes to estimate the infinite-size critical point. The apparent critical temperature $T_{\mathrm{c}}(L)$ is expected to vary with system size as [116, 119–122]

$$T_{\mathrm{c}}(L) - T_c(\infty) \sim L^{-(\theta+1)/\nu} , \qquad (7.3)$$

where $T_{\mathrm{c}}(L)$ is the apparent critical temperature of the finite-size system, $T_c(\infty)$ is the true critical point of the infinite-size system, L is system length, and $\theta = 0.54$ and $\nu = 0.629$

are scaling constants [122]. The critical density of the finite-size system scales in a similar manner as

$$\rho_{\mathrm{c}}(L) - \rho_{\mathrm{c}}(\infty) \sim L^{-(d-1/\nu)}, \tag{7.4}$$

where d is the number of spatial dimensions of the simulation. In this work, $d = 3$. The critical pressure of the finite size system also scales as

$$P_{\mathrm{c}}(L) - P_{c}(\infty) \sim L^{-(d-1/\nu)}. \tag{7.5}$$

By measuring the apparent critical parameters for several different system sizes, one can use the above scaling relationships to extrapolate to the infinite-size critical point. It is interesting to note that for some works, the finite-size critical temperature was higher than infinite-size, while for other works it was lower. For example, Potoff and Panagiotopoulos found $T_{\mathrm{c}}(L_{\mathrm{s}}) < T_{c}(\infty)$ by about 1% [116], where L_{s} is the size of the smallest system, while Caillol found $T_{\mathrm{c}}(L_{\mathrm{s}}) > T_{c}(\infty)$ by about 7% [74] (using approximately the same size for the smallest system studied). This could be due to the use of different simulation techniques or long-range correction methods.

7.3 Using the CPP method to predict critical parameters

The CPP method allows one to obtain accurate pressure and chemical potential curves for a wide range of densities in a single simulation. In essence, the CPP method can predict homogeneous pressure and temperature isotherms for both supercritical and subcritical conditions. For the subcritical case, these isotherms show van der Waals loops. Binodal and spinodal densities can be determined thermodynamically from the isotherms as described in Chapter 3.

In the CPP method, an external potential is applied to the system which helps form a stable density profile for simulations below and at the critical temperature. Even above the critical temperature, the external field can produce a stable artificial interface (*i.e.* equilibrium density gradients). With this in mind, the CPP method seems ideally suited to predict critical properties. No insertions are needed (unlike the NPT-plus-test-particle method). Normally when predicting critical points, the formation of an interface is undesirable and the GEMC method is preferred, but unlike other methods, the CPP method can use the interfacial region of a two-phase system.

However, using the CPP method may also have some potential disadvantages that need to be overcome. For example, it is necessary to use an external potential strong enough to maintain a stable density profile. If the field is too weak, the interface may move around in the simulation. However, if the field is too strong, high density gradients make the inhomogeneous correction term less reliable. Using a strong external potential also creates a wide range of densities in the simulation away from the desired critical density, so one may need to use a large simulation cell to obtain accurate pressure and chemical potential derivatives, which would decrease computational efficiency.

We describe below how the CPP method can be used to predict critical points using binodal densities, spinodal densities, and pressure isotherms.

7.3.1   Binodal densities

As shown in Chapter 3, binodal densities ρ_v and ρ_l can be determined with the CPP method from the conditions $P^0(\rho_v) = P^0(\rho_l)$ and $\mu^0(\rho_v) = \mu^0(\rho_l)$. Alternatively, one can determine binodal densities using the Maxwell equal-area construction method [37]. In the CPP method, binodal densities cannot be determined by simply averaging bulk liquid and vapor densities because the external field disrupts these bulk regions. After determining binodal densities as a function of temperature, one can then use the scaling laws given in Eqs. 7.4

and 7.2. This is very similar to the NPT-plus-test-particle method, but no particle insertions are necessary when using the CPP method.

Finite-size effects when using the CPP method are expected to be comparable to those of other simulation methods and may even be smaller because the applied external field in the CPP method suppresses fluctuations in at least one direction. One can also use the CPP method to determine the apparent critical point for different simulation sizes and then use the finite-size scaling approach given in Eqs. 7.3-7.5.

7.3.2 Spinodal densities

Pressure isotherms of pure-component fluids below the critical temperature exhibit a van der Waals loop, which can be used to determine stability of the fluid. Regions of the fluid where $\left(\frac{\partial P}{\partial V}\right)_T < 0$ are thermodynamically unstable and can spontaneously phase-split. The spinodal vapor and liquid densities are found where $\left(\frac{\partial P}{\partial V}\right)_T = 0$. The critical point can then be determined by using scaling laws with the difference in spinodal densities as the order parameter. The LJ EOS [72] suggests that spinodal densities follow similar scaling laws as the binodal densities:

$$\rho_{\mathrm{sl}} - \rho_{\mathrm{sv}} = C \left(T - T_{\mathrm{c}}\right)^{\beta} , \tag{7.6}$$

where $\rho_{s,l}$ is the liquid spinodal density, $\rho_{s,v}$ is the vapor spinodal density, and C is a constant determined from the fit.

Spinodal densities also seem to follow a modified law of rectilinear diameters as

$$\tfrac{1}{2} \left(\rho_{\mathrm{sl}} + \rho_{\mathrm{sv}}\right) = \rho_{\mathrm{c}} + D \left(T - T_{\mathrm{c}}\right) , \tag{7.7}$$

where D is a constant determined from the fit of the data.

Previous results show that vapor binodal and spinodal densities are difficult to determine accurately for temperatures well-below the critical point using the CPP method (see Chapter

3) because a sharp interface is formed and the truncation error in the approximation of the homogeneous pressure depends on the density gradient. However, close to the critical temperature, the inhomogeneity of the system decreases and the gradient correction term should be more accurate (assuming a reasonable external potential is used).

It is important to realize that the van der Waals loop corresponds to the chemical potential and pressure of the *homogeneous* fluid. In other words, the pressure and chemical potential shown by the van der Waals loop are those of the fluid with uniform average density. However, it is not usually possible to simulate a fluid in the unstable density region and obtain a system of uniform density because the fluid will spontaneously split into different phases forming bubbles, droplets, *etc.* For this reason, the complete van der Waals loop is not experimentally observed.

Here we give two exceptions. First, for a planar interface, the density profile transitions from vapor to liquid, passing through metastable and unstable conditions over a finite distance. As seen in Chapter 3, the homogeneous pressure and resulting chemical potential at these conditions can be approximated using Eq. 3.23, and the results give the van der Waals loop. In this manner spinodal points (maxima and minima of the van der Waals loop) are accessible inside a finite two-phase interface [50, 51]. Second, it is not thermodynamically favorable for simulations of very small systems to phase-split. One can therefore obtain a van der Waals loop by using a small system size and performing several quasi-uniform density simulations at unstable and metastable conditions. Because the density of the fluid stays nearly uniform, the full VdW loop can be mapped out [5]. Similarly, density gradient theory relies on an analytical equation of state (containing a van der Waals loop) to predict the surface tension and density profile of a liquid-vapor interface. If no van der Waals loop were present and the pressure is assumed constant throughout the interface, an incorrect step-like density profile with no surface tension results [37].

It is interesting to note that when developing equations of state, authors frequently discard data from the metastable and unstable regions [73, 99]. We also note that Binder

has also suggested that the van der Waals loop is merely a mean-field artifact and that the spinodal points are ill-defined [123]. However, his simulations included two phases (bubbles and droplets) [123]. His conclusions are not valid because the fluid in his simulations was not homogeneous; in order to observe the van der Waals loop, either the system must truly be homogeneous (uniform average density), or one must use a gradient correction like the pressure tensor method (Eq. 3.23). Simply measuring the *average* chemical potential or pressure of the system is not adequate to obtain *homogeneous* properties.

7.3.3   Pressure isotherms

As shown in Figure 7.1 (created using the LJ EOS [72]), the critical point of a fluid is given by the conditions $\left(\frac{\partial P}{\partial V}\right)_T = \left(\frac{\partial^2 P}{\partial V^2}\right)_T = 0$. Similar conditions also hold for the chemical potential. The simplest way to predict critical properties using the CPP method is to adjust the temperature of the simulation until these conditions are met in the predicted pressure isotherm.

Using binodal or spinodal densities requires that one perform simulations at temperatures lower than the critical temperature and extrapolate to the critical temperature. However, pressure isotherms also allow one to *interpolate* to the critical point using the locus of minimum points in $dP/d\rho$ as shown in Figure 7.1b.

Alternatively, one can calculate the bulk modulus K_T using pressure isotherms for temperatures both lower and higher than the critical temperature and use universal scaling laws and critical exponents for K_T [117]. The bulk modulus K_T can be defined as

$$K_T = \rho \left(\frac{\partial P}{\partial \rho}\right)_T .$$

(7.8)
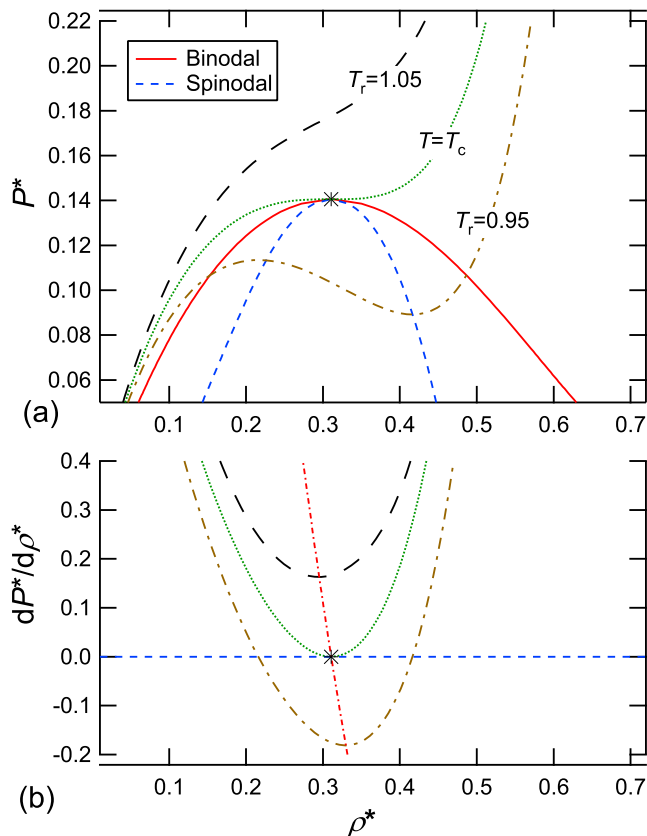
Figure 7.1: (a) Pressure isotherms *vs* density and (b) derivative of pressure with respect to density *vs* density for various temperatures for the LJ fluid.

7.4 Long-range corrections

For the LJ fluid, several LRC methods are available. For example, one can use a large cutoff, the local standard LRC for pressure [71] (Chapter 3), an Ewald sum (Chapter 4), or an SB Ewald sum (Chapter 5).

The critical parameters of a fluid are very sensitive to the truncation of the intermolecular potential, particularly if no LRCs are used [70]. This fact is not surprising, as truncating the potential makes the particles less attracted to each other and therefore less likely to separate into different phases. Phase behavior always involves a delicate balance between intermolecular attraction and repulsion, which is particularly apparent near the critical point.

MC simulations normally truncate the intermolecular *potential*, while MD simulations normally truncate intermolecular *forces*. This corresponds to the use of the spherically-truncated (ST) potential for MC simulations and the spherically-truncated and shifted (STS) potential for MD simulations [70]. When using the same cutoff and no LRCs, the critical temperature of ST potential is significantly closer to the critical temperature of the untruncated potential than when using the STS potential [115].

The effect of truncation on the critical temperature can be estimated using by using the standard LRC for pressure. When the long-range force can be neglected ($r_{\text{cut}} \gtrsim 5.5\sigma$), the long-range correction to the homogeneous pressure for the STS potential can be approximated by a local term as [71]

$$P^{\text{LR}}(\rho) = -\frac{16\pi\rho^2}{9} \left[3 \left(\frac{1}{r_{\text{cut}}} \right)^3 - 2 \left(\frac{1}{r_{\text{cut}}} \right)^9 \right]. \tag{7.9}$$

Using the relationship $d\mu = dP/\rho$, we obtain

$$\mu^{\text{LR}}(\rho) = -\frac{32\pi\rho}{9} \left[3 \left(\frac{1}{r_{\text{cut}}} \right)^3 - 2 \left(\frac{1}{r_{\text{cut}}} \right)^9 \right], \tag{7.10}$$

Taking the derivative of Eq. 7.10 gives

$$\frac{d\mu^{\text{LR}}}{d\rho} = -\frac{32\pi}{9} \left[3 \left(\frac{1}{r_{\text{cut}}} \right)^3 - 2 \left(\frac{1}{r_{\text{cut}}} \right)^9 \right], \tag{7.11}$$

which gives a constant that depends directly on r_{cut}. One can estimate the apparent critical temperature $T_{\text{c}}^{\text{app}}$ for a given cutoff using an EOS and solving the following equation for $T_{\text{c}}^{\text{app}}$:

$$\frac{d\mu^{\text{EOS}}(T_{\text{c}}^{\text{app}}, \rho_{\text{c}})}{d\rho} - \frac{d\mu^{\text{LR}}}{d\rho} = 0, \tag{7.12}$$

which shows that $T_{\text{c}}^{\text{app}}$ decreases with decreasing r_{cut} if no LRCs are applied [73, 124].

7.5 Preliminary results and discussion

In order to test the proposed methods, we simulated the LJ fluid using the Large-scale Atomic/Molecular Massively Parallel Simulator (LAMMPS) [125], a molecular dynamics code developed by Sandia National Labs. Two different CPP simulations were used, and sample input files are included in Appendix D. The first simulation was run at $T^* = 1.312$, while the second simulation was run at $T^* = 1.320$. Both simulations used $N = 32000$ atoms, $L_z = 32\,L_x = 32\,L_y$, $r_{\mathrm{cut}} = 6.0\,\sigma$, $\triangle U^*_{\mathrm{max}} = 0.5$, and were run on 64 processors for 3×10^7 timesteps after equilibration. For simplicity, the H contour was used to calculate the pressure tensor. The local LRC for homogeneous pressure given in Eq. 7.9 was also applied at the end of the simulations.

For the first simulation at $T^* = 1.312$, the minimum point in $dP/d\rho$ (see Figure 7.1b) was at $\rho^* = 0.315$ and $dP^*/d\rho^* = -0.0134$. For the second simulation at $T^* = 1.32$, the minimum point in $dP/d\rho$ was at $\rho^* = 0.307$ and $dP^*/d\rho^* = -0.00533$. Using a simple linear extrapolation of this data, the predicted critical temperature and critical density of the LJ fluid are $T^*_{\mathrm{c}} = 1.325$ and $\rho^*_{\mathrm{c}} = 0.301$.

Table 7.1 compares critical parameters for the LJ fluid given by different works. In Table 7.1, the last digit in parenthesis refers to the uncertainty in the measurement. For example, 1.316(3) means 1.316 ± 0.003. Figure 7.2 shows a plot of T_{c} *vs* ρ_{c} for the LJ fluid using the data in Table 7.1 and also the preliminary results from the CPP method. We note that Ref. [126] used $r_{\mathrm{cut}} = 5\sigma$ and Ref. [111] used $r_{\mathrm{cut}} = 6\sigma$ without any LRCs, which lowers the apparent critical temperature as described previously, so we have excluded these points from Figure 7.2.

The critical temperature predicted using the CPP method is within the uncertainty of Caillol's results [74], but the predicted critical density is not. For this preliminary test using the CPP method, the critical parameters were sensitive to the number of Fourier terms used to fit the pressure and density profiles. Using longer simulations to reduce noise in the data and including more data at different temperatures could help. If we assume that

Table 7.1: Comparison of LJ critical parameters from different works.

Reference	T_c	ρ_c	P_c	Method
[124]	1.316(3)	0.304(6)		GEMC
[108]	1.310	0.314	0.126	NPT-plus-test-particle
[126]	1.281(5)	0.32(1)		GEMC
[74]	1.326(2)	0.316(2)	0.111(2)	GCMC, MHR
[116]	1.3120(7)	0.316(1)	0.12796(6)	GCMC, MHR
[127]	1.311(2)	0.316(2)		GCMC, MHR
[110]	1.3207(4)	0.316(1)	0.1288(5)	NVT-plus-test-particle
[115]	1.3145(2)	0.316(1)		GCMC, MHR
[63]	1.309	0.297		integral equation theory
[122]	1.3123(6)	0.3174(6)		GCMC, MHR
[122]	1.3120(7)	0.3174(6)		GCMC, MHR
[122]	1.313(1)	0.317(1)		GCMC, MHR
[111]	1.293	0.313		2-phase MD

the density at the minimum point in $dP/d\rho$ is weakly dependent on temperature (over this temperature range) and use the average of the densities at the minimum point in $dP/d\rho$ for the two CPP simulations to estimate ρ_c instead of the linear extrapolation, a more reasonable critical density of $\rho_c^* = 0.311$ is obtained, as shown in Figure 7.2. Adjusting the form of the external potential to reduce density gradients and using a finite-size scaling technique could also improve results.
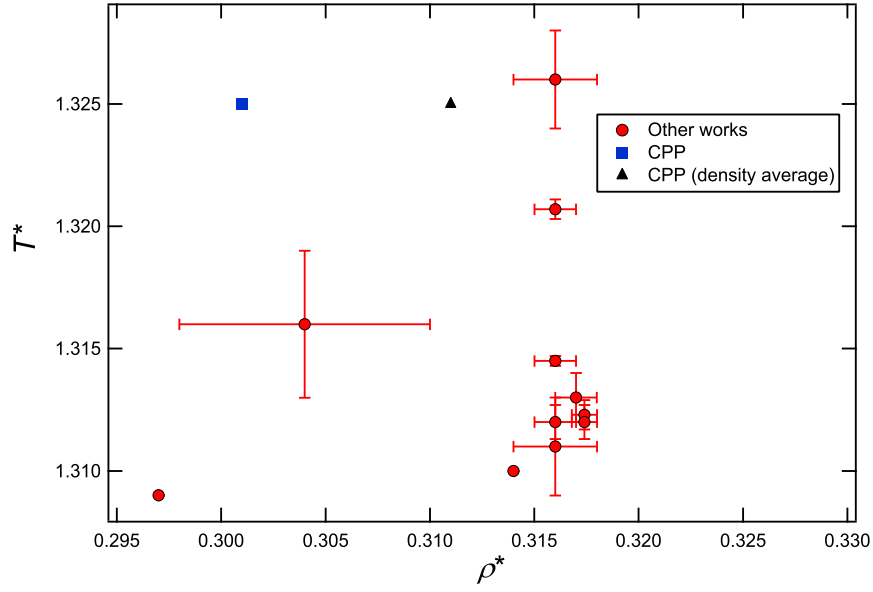
Figure 7.2: Plot of LJ critical points from the different works listed in Table 7.1 and from preliminary results using the CPP method.

7.6   Conclusion

In this chapter, we review existing methods to predict critical points using molecular simulations, which normally predict binodal densities for different temperatures and then extrapolate to the critical point. We also suggest a few ways of using the CPP method to predict fluid critical parameters using binodal densities, spinodal densities, and pressure isotherms. The effects of finite-size systems and truncation on the critical parameters are also discussed and preliminary results are given for the LJ fluid.

Chapter 8

Conclusion

8.1 Summary of results

A new method, called chemical potential perturbation (CPP), has been developed to predict the chemical potential as a function of composition in periodic molecular simulations. The CPP method applies a spatially varying external force field to the simulation, causing the density or composition to depend upon position in the simulation cell. Following equilibration, the homogeneous (uniform or bulk) chemical potential as a function of density can be determined relative to some reference state after correcting for the effects of the inhomogeneity of the system. Some advantages of the CPP method are that it allows one to predict chemical potential for a wide range of composition points using a single simulation and it works for dense fluids and structured molecules where other prediction methods become inefficient.

This work has a broad range of application, including topics beyond chemical potential such as surface tension, phase-equilibria, solids, binodal densities and van der Waals loops, local thermodynamic properties, Ewald sums, critical points, and inhomogeneous systems in general.

The external potential in the CPP method produces an inhomogeneous system and therefore surface tension, regardless of temperature. For supercritical conditions, this inhomogeneity behaves similar to a liquid-vapor interface. One can correct for this inhomogeneity and obtain properties for the whole range of densities in the inhomogeneous simulation.

For pure-component systems, three different methods of approximating the inhomogeneous correction are developed. The first method uses the van der Waals density gradient theory, the second method uses the local pressure tensor, and the third method uses the Triezenberg–Zwanzig definition of surface tension. These inhomogeneous corrections allow one to relate a homogeneous system to an inhomogeneous one. For example, at the liquid-vapor interface, the density transitions smoothly between bulk liquid and vapor and passes through thermodynamically metastable and unstable fluid conditions. The inhomogeneous correction term allows one to peer into this region and obtain binodal densities and the full van der Waals loop as if the system were homogeneous. This information is impossible to obtain experimentally.

The CPP method is also extended to an Ewald lattice sum treatment of intermolecular potentials. We discuss the problem of ambiguity in some local (position-dependent) thermodynamic properties. For example, when computing the local pressure tensor for the inhomogeneous correction term, one can use the Irving-Kirkwood (IK) or Harasima (H) contours of distributing the pressure. These two contours are compared, and for a planar interface, it is shown that the homogeneous pressure and resulting chemical potential can be approximated with the CPP method using either the IK or the H contour, though with the lattice sum method the H contour has much greater computational efficiency. A new lattice sum method for the Lennard-Jones fluid called SB Ewald is also presented, which is more computationally efficient than the traditional LJ lattice sum when the average density of the system varies only in one direction. The SB Ewald sum method can be used with the CPP method and also for predicting the surface tension of the LJ fluid.

We note that due to this project, a method of obtaining per-atom energy and pressure was implemented into LAMMPS [125] for both the Ewald sum and particle-particle particle mesh (P3M) methods [101]. These modifications are not only useful for the prediction of chemical potential using the CPP method, but also for the prediction of material properties such as thermal conductivity.

Finally, the CPP method is extended to activity coefficient prediction of multi-component fluids. For multi-component systems, a separate external potential is applied to each species, and constant normal component pressure is maintained by adjusting the external field of one of the species. Preliminary results are presented for several different binary Lennard-Jones (LJ) mixtures. The application of the CPP method to the prediction of fluid critical parameters is also discussed.

8.2   Future work

The CPP method could be greatly extended beyond the scope of this project. Only preliminary results were given for solids in Chapter 4 and mixtures in Chapter 6. Thus, one could further develop the CPP method for solids and also for mixtures, including ionic mixtures and liquid-liquid systems. In Chapter 5, preliminary results were given for the SB Ewald sum method, which we plan to develop further in a future paper. Chapter 7 describes how the CPP method could be used to predict critical points.

Another application of the CPP method is in the development of intermolecular potential models. One could use the CPP method to obtain pressure *vs* density curves or other thermodynamic data from the proposed model and then modify the model parameters until data from the model matches data from experiments. Similarly, given an intermolecular potential model, one could also obtain an equation of state for this model by using a few CPP simulations at different temperatures and fitting this data to an analytical equation of state.

In this work, relatively small and simple models (LJ and SPC/E water) were used to validate the CPP method. One could extend the CPP method to large, structured molecules such as long-chain alkanes, perhaps using an atomic pressure tensor instead of the molecular pressure tensor used for SPC/E water in Chapter 4. For long molecules that may span many slabs (normal to the z direction), local properties such as density and pressure tensor could

be obtained by using the position of individual molecular sites (*i.e.*, atoms) instead of the molecular center of mass, and the position-dependent external potential could also act on molecular sites instead of molecular center of mass.

The TZ inhomogeneous correction method was presented in Chapter 3. It would be interesting to apply the TZ method to a two-phase system and compare the resulting VdW loop with that given by the pressure tensor method. The TZ method as given in Chapter 3 also approximated the inhomogeneous direct correlation function using the homogeneous direction correlation function. Perhaps using the TZ method with the exact inhomogeneous direct correlation function would improve results.

In the CPP method, an external potential causes the composition to vary with position. Alternatively, one could vary temperature instead of composition. This could be accomplished by modifying the thermostat to obtain a temperature profile and then applying an external potential to maintain constant density. The chemical potential of the system would then be related to the applied field. In a similar manner, one could vary both density and temperature to obtain an extremely wide range of state points in a single simulation. Varying both T and ρ could be even more useful than the original CPP method when predicting fluid critical points.

Bibliography

[1] G. Job and F. Herrmann, Eur. J. Phys. **27**, 353 (2006).

[2] R. Baierlein, Am. J. Phys. **69**, 423 (2001).

[3] S. G. Moore and D. R. Wheeler, J. Chem Phys. **134**, 114514 (2011).

[4] S. G. Moore and D. R. Wheeler, J. Chem. Phys. **136**, 164503 (2012).

[5] D. Frenkel and B. Smit, *Understanding molecular simulation: from algorithms to applications* (Academic Press, San Diego, 2002).

[6] R. L. Rowley, *Statistical mechanics for thermophysical property calculations* (Prentice Hall, Englewood Cliffs, NJ, 1994).

[7] B. Widom, J. Chem. Phys. **39**, 2808 (1963).

[8] B. Widom, J. Phys. Chem. **86**, 869 (1982).

[9] B. Widom, J. Stat. Phys. **19**, 563 (1978).

[10] C. H. Bennett, J. Comput. Phys. **22**, 245 (1976).

[11] K. S. Shing and K. E. Gubbins, Mol. Phys. **46**, 1109 (1982).

[12] G. C. Boulougouris, Mol. Phys. **96**, 905 (1999).

[13] P. Jedlovszky and M. Mezei, J. Am. Chem. Soc. **122**, 5125 (2000).

[14] L. B. Partay, P. Jedlovszky, P. N. M. Hoang, S. Picaud, and M. Mezei, J. Phys. Chem. C **111**, 9407 (2007).

[15] G. L. Deitrick, L. E. Scriven, and H. T. Davis, J. Chem. Phys. **90**, 2370 (1989).

[16] G. L. Deitrick, L. E. Scriven, and H. T. Davis, Mol. Simulat. **8**, 239 (1992).

[17] R. Delgado-Buscalioni, G. De Fabritiis, and P. V. Coveney, J. Chem. Phys. **123**, 9 (2005).

[18] K. K. Mon and R. B. Griffiths, Phys. Rev. A **31**, 956 (1985).

[19] K. Ding and J. P. Valleau, J. Chem. Phys. **98**, 3306 (1993).

[20] K. S. Shing and K. E. Gubbins, Mol. Phys. **43**, 717 (1981).

[21] J. Kolafa and I. Nezbeda, Mol. Simulat. **5**, 391 (1991).

[22] P. Attard, J. Chem. Phys. **98**, 2225 (1993).

[23] D. A. Kofke and P. T. Cummings, Mol. Phys. **92**, 973 (1997).

[24] A. Z. Panagiotopoulos, Mol. Phys. **61**, 813 (1987).

[25] A. Z. Panagiotopoulos, N. Quirke, M. Stapleton, and D. J. Tildesley, Mol. Phys. **63**, 527 (1988).

[26] R. L. Rowley, T. D. Shupe, and M. W. Schuck, Mol. Phys. **82**, 841 (1994).

[27] M. Henrichsen and R. L. Rowley, Fluid Phase Equilibria **137**, 75 (1997).

[28] T. R. Pollock, P. Crozier, and R. L. Rowley, Fluid Phase Equilib. **217**, 89 (2004).

[29] P. S. Crozier and R. L. Rowley, Fluid Phase Equilibria **193**, 53 (2002).

[30] R. L. Rowley, M. W. Schuck, and J. C. Perry, Mol. Phys. **86**, 125 (1995).

[31] J. D. Weeks, D. Chandler, and H. C. Andersen, J. Chem. Phys. **54**, 5237 (1971).

[32] J. G. Powles, B. Holtz, and W. A. B. Evans, J. Chem. Phys. **101**, 7804 (1994).

[33] W. Humphrey, A. Dalke, and K. Schulten, J. Mol. Graphics **14**, 33 (1996).

[34] H. T. Davis, *Statistical mechanics of phases, interfaces, and thin films* (VCH, New York, 1996).

[35] J. D. van der Waals, Z. Phys. Chem., Stoechiom. Verwandtschaftsl. **13**, 657 (1894).

[36] J. S. Rowlinson, J. Stat. Phys. **20**, 197 (1979).

[37] J. S. Rowlinson and B. Widom, *Molecular theory of capillarity* (Clarendon, Oxford, 1982).

[38] J. W. Cahn and J. E. Hilliard, J. Chem. Phys. **28**, 258 (1958).

[39] A. J. M. Yang, P. D. Fleming, and J. H. Gibbs, J. Chem. Phys. **64**, 3732 (1976).

[40] D. Duque, J. C. Pamies, and L. F. Vega, J. Chem. Phys. **121**, 11395 (2004).

[41] J. H. Irving and J. G. Kirkwood, J. Chem. Phys. **18**, 817 (1950).

[42] P. Schofield and J. R. Henderson, Proc. R. Soc. London, Ser. A **379**, 231 (1982).

[43] A. Harasima, Adv. Chem. Phys. **1**, 203 (1958).

[44] J. G. Kirkwood and F. P. Buff, J. Chem. Phys. **17**, 338 (1949).

[45] J. P. R. B. Walton, D. J. Tildesley, J. S. Rowlinson, and J. R. Henderson, Mol. Phys. **48**, 1357 (1983).

[46] J. P. R. B. Walton, Mol. Phys. **58**, 1013 (1986).

[47] F. Goujon, P. Malfreyt, J. M. Simon, A. Boutin, B. Rousseau, and A. H. Fuchs, J. Chem. Phys. **121**, 12559 (2004).

[48] B. S. Carey, L. E. Scriven, and H. T. Davis, J. Chem. Phys. **69**, 5040 (1978).

[49] H. T. Davis and L. E. Scriven, Adv. Chem. Phys. **49**, 357 (1982).

[50] A. R. Imre, G. Mayer, G. Hazi, R. Rozas, and T. Kraska, J. Chem. Phys. **128**, 114708 (2008).

[51] T. Kraska, F. Romer, and A. R. Imre, J. Phys. Chem. B **113**, 4688 (2009).

[52] S. M. Oversteegen, P. A. Barneveld, F. A. M. Leermakers, and J. Lyklema, Langmuir **15**, 8609 (1999).

[53] F. P. Buff, J. Chem. Phys. **23**, 419 (1955).

[54] D. Lamoen and N. H. March, Phys. Chem. Liq. **38**, 495 (2000).

[55] R. A. Lovett, Ph.D. thesis, University of Rochester (1965).

[56] D. G. Triezenberg and R. Zwanzig, Phys. Rev. Lett. **28**, 1183 (1972).

[57] R. Lovett, P. W. DeHaven, J. James J. Vieceli, and F. P. Buff, J. Chem. Phys. **58**, 1880 (1973).

[58] J. R. Henderson, Mol. Phys. **39**, 709 (1980).

[59] J. Stecki and S. Toxvaerd, J. Chem. Phys. **103**, 9763 (1995).

[60] J. Stecki, J. Chem. Phys. **109**, 5002 (1998).

[61] J. Stecki and S. Toxvaerd, J. Chem. Phys. **117**, 2860 (2002).

[62] I. Omelyan, A. Kovalenko, and F. Hirata, Chem. Phys. Lett. **397**, 368 (2004).

[63] I. Omelyan, F. Hirata, and A. Kovalenko, Phys. Chem. Chem. Phys. **7**, 4132 (2005).

[64] C. Ebner, W. F. Saam, and D. Stroud, Phys. Rev. A **14**, 2264 (1976).

[65] L. S. Ornstein and F. Zernike, Proc. Roy. Acad. Sci., Amsterdam **17**, 793 (1914).

[66] J. K. Percus and G. J. Yevick, Phys. Rev. **110**, 1 (1958).

[67] M. J. Gillan, Mol. Phys. **38**, 1781 (1979).

[68] L. L. Lee, *Molecular thermodynamics of nonideal fluids* (Butterworths, Boston, 1988).

[69] M. Allen and D. Tildesley, *Computer simulation of liquids* (Oxford Science, 1989).

[70] A. Trokhymchuk and J. Alejandre, J. Chem. Phys. **111**, 8510 (1999).

[71] M. X. Guo and B. C. Y. Lu, J. Chem. Phys. **106**, 3688 (1997).

[72] J. Kolafa and I. Nezbeda, Fluid Phase Equilibria **100**, 1 (1994).

[73] J. K. Johnson, J. A. Zollweg, and K. E. Gubbins, Mol. Phys. **78**, 591 (1993).

[74] J. M. Caillol, J. Chem. Phys. **109**, 4885 (1998).

[75] M. A. van der Hoef, J. Chem. Phys. **113**, 8142 (2000).

[76] J. Janecek, J. Phys. Chem. B **110**, 6264 (2006).

[77] G. A. Chapela, G. Saville, S. M. Thompson, and J. S. Rowlinson, J. Chem. Soc. Farad. T. 2 **73**, 1133 (1977).

[78] E. M. Blokhuis, D. Bedeaux, C. D. Holocomb, and J. A. Zollweg, Mol. Phys. **85**, 665 (1995).

[79] A. Lotfi, J. Vrabec, and J. Fischer, Molecular Simulation **5**, 233 (1990).

[80] M. Mecke, J. Winkelmann, and J. Fischer, J. Chem. Phys. **107**, 9264 (1997).

[81] J. Janecek, J. Chem. Phys. **131**, 124513 (2009).

[82] L. G. MacDowell and F. J. Blas, J. Chem. Phys. **131**, 074705 (2009).

[83] D. J. Adams, J. Chem. Phys. **78**, 2585 (1983).

[84] B. A. Luty, I. G. Tironi, and W. F. van Gunsteren, J. Chem. Phys. **103**, 3014 (1995).

[85] D. M. York, W. T. Yang, H. Lee, T. Darden, and L. G. Pedersen, J. Amer. Chem. Soc. **117**, 5001 (1995).

[86] N. Karasawa and W. A. Goddard, J. Chem. Phys. **93**, 7320 (1989).

[87] D. R. Wheeler and R. L. Rowley, Mol. Phys. **94**, 555 (1998).

[88] J. Lopez-Lemus and J. Alejandre, Mol. Phys. **100**, 2983 (2002).

[89] P. J. in't Veld, A. E. Ismail, and G. S. Grest, J. Chem. Phys. **127**, 144711 (2007).

[90] D. M. Heyes, Phys. Rev. B **49**, 755 (1994).

[91] J. Alejandre, D. J. Tildesley, and G. A. Chapela, J. Chem. Phys. **102**, 4574 (1995).

[92] J. Sonne, F. Y. Hansen, and G. H. Peters, J. Chem. Phys. **122**, 124903 (2005).

[93] A. Ghoufi, F. Goujon, V. Lachet, and P. Malfreyt, J. Chem. Phys. **128**, 154716 (2008).

[94] J. Wang and X. C. Zeng, J. Theor. Comput. Chem. **8**, 733 (2009).

[95] F. Varnik, J. Baschnagel, and K. Binder, J. Chem. Phys. **113**, 4444 (2000).

[96] V. Simmons and J. B. Hubbard, J. Chem. Phys. **120**, 2893 (2004).

[97] H. J. C. Berendsen, J. R. Grigera, and T. P. Straatsma, J. Chem. Phys. **91**, 6269 (1987).

[98] B. D. Todd, D. J. Evans, and P. J. Daivis, Phys. Rev. E **52**, 1627 (1995).

[99] A. Plugatyr and I. M. Svishchev, Fluid Phase Equilibria **277**, 145 (2009).

[100] N. D. Lu, J. K. Singh, and D. A. Kofke, J. Chem. Phys. **118**, 2977 (2003).

[101] R. Hockney and J. Eastwood, *Computer simulation using particles* (McGraw-Hill, New York, 1981).

[102] J. G. Kirkwood and F. P. Buff, J. Chem. Phys. **19**, 774 (1951).

[103] J. W. Nichols, S. G. Moore, and D. R. Wheeler, Phys. Rev. E **80**, 051203 (2009).

[104] D. Paschek, A. Geiger, J. Fischer, and G. Sadowski, Z. Phys. Chem. **222**, 687 (2008).

[105] E. Sanz and C. Vega, J. Chem. Phys. **126** (2007).

[106] P. D. Fleming, A. J. M. Yang, and J. H. Gibbs, J. Chem. Phys. **65**, 7 (1976).

[107] D. Moller and J. Fischer, Mol. Phys. **69**, 463 (1990).

[108] A. Lotfi, J. Vrabec, and J. Fischer, Mol. Phys. **76**, 1319 (1992).

[109] I. Szalai, J. Liszi, and D. Boda, Chem. Phys. Lett. **246**, 214 (1995).

[110] H. Okumura and F. Yonezawa, J. Phys. Soc. Jpn. **70**, 1990 (2001).

[111] J. T. Fern, D. J. Keffer, and W. V. Steele, J. Phys. Chem. B **111**, 3469 (2007).

[112] S. Patel, W. V. Wilding, and R. L. Rowley, J. Chem. Phys. **134** (2011).

[113] A. M. Ferrenberg and R. H. Swendsen, Phys. Rev. Lett. **61**, 2635 (1988).

[114] A. M. Ferrenberg and R. H. Swendsen, Phys. Rev. Lett. **63**, 1195 (1989).

[115] W. Shi and J. Johnson, Fluid Phase Equilibria **187**, 171 (2001).

[116] J. J. Potoff and A. Z. Panagiotopoulos, J. Chem. Phys. **109**, 10914 (1998).

[117] H. E. Stanley, *Introduction to phase transitions and critical phenomena* (Oxford University Press, New York, 1971).

[118] J. S. Rowlinson, *Liquids and liquid mixtures* (Butterworths Scientific, London, 1982).

[119] N. B. Wilding and A. D. Bruce, J. Phys.: Condens. Matter **4**, 3087 (1992).

[120] N. B. Wilding, Phys. Rev. E **52**, 602 (1995).

[121] N. B. Wilding, J. Phys.: Condens. Matter **9**, 585 (1997).

[122] J. Perez-Pellitero, P. Ungerer, G. Orkoulas, and A. D. Mackie, J. Chem. Phys. **125** (2006).

[123] K. Binder, Mol. Phys. **108**, 1797 (2010).

[124] B. Smit, J. Chem. Phys. **96**, 8639 (1992).

[125] S. Plimpton, J. Comp. Phys. **117**, 1 (1995), URL `http://lammps.sandia.gov`.

[126] A. Z. Panagiotopoulos, Int. J. Thermophys. **15**, 1057 (1994).

[127] J. J. Potoff and A. Z. Panagiotopoulos, J. Chem. Phys. **112**, 6411 (2000).

Appendix A

Gradient expansion of the pressure tensor using the H contour

Here we partition the local pressure tensor using the H contour into homogeneous and inhomogeneous terms using a Taylor series expansion in density gradient. We follow and adapt the method used for the IK contour given by Davis in Ref. [34].

For two spherical molecules, one at position $\mathbf{r}$ and the other at position $\mathbf{r}'$, we define $\mathbf{s} = \mathbf{r}' - \mathbf{r}$. The pressure tensor using the H contour can be written as [37]

$$\mathbf{P}(\mathbf{r}) = \rho(\mathbf{r})\, k_{\mathrm{B}}\, T\, \mathbf{I} - \tfrac{1}{2} \int \frac{\mathbf{ss}}{s} u'(s)\, \rho^{(2)}(\mathbf{r}, \mathbf{r} + \mathbf{s})\, d\mathbf{s}\,, \tag{A.1}$$

where $-u'(s)$ is the pairwise force and $\mathbf{I}$ is the unit tensor. For this and all subsequent equations, one can assume that adjacent vectors correspond to an outer product. The pair distribution function $\rho^{(2)}$ is given as

$$\rho^{(2)}(\mathbf{r}, \mathbf{r} + \mathbf{s}) = \rho(\mathbf{r})\, \rho(\mathbf{r} + \mathbf{s})\, g^{(2)}(\mathbf{r}, \mathbf{r} + \mathbf{s})\,, \tag{A.2}$$

where $g^{(2)}$ is the radial distribution function of the inhomogeneous fluid.

Expanding $\rho(\mathbf{r} + \mathbf{s})$ around $\rho(\mathbf{r})$ using a Taylor series gives:

$$\rho(\mathbf{r} + \mathbf{s}) = \sum_{i=0}^{\infty} \frac{(\mathbf{s} \cdot \nabla)^i}{i!} \rho(\mathbf{r})\,. \tag{A.3}$$

Combining Eqs. A.1, A.2, and A.3 yields

$$\mathbf{P}(\mathbf{r}) = \rho(\mathbf{r}) \, k_{\mathrm{B}} \, T \, \mathbf{I} - \frac{1}{2} \int \frac{\mathbf{ss}}{s} u'(s) \, \rho(\mathbf{r}) \sum_{i=0}^{\infty} \left[\frac{(\mathbf{s} \cdot \nabla)^i}{i!} \rho(\mathbf{r}) \, g^{(2)}(\mathbf{r}, \mathbf{r} + \mathbf{s}) \right] d\mathbf{s} \,. \tag{A.4}$$

We assume that the density profile is sufficiently slowly varying to allow truncation after 2nd-order terms in density gradient. In this manner, $g^{(2)}$ is weekly dependent on $\mathbf{r}$ and can be approximated by the radial distribution function of the homogeneous fluid at ρ_{avg}. In this manner, $g^{(2)}$ also depends only on the pair-wise separation distance s. The integrals in Eq. A.4 are then of the form

$$\mathbf{T}_m = \int \mathbf{s} \cdots \mathbf{s} \, f(s) \, d\mathbf{s} \,, \tag{A.5}$$

where $\mathbf{T}_m$ is an mth rank isotropic tensor, and $f(s)$ is an isotropic function of $\mathbf{s}$ [34]. If m is odd, then the integral given in Eq. A.5 is equal to zero [34].

Expanding the series to second order in density gradients and neglecting odd terms yields

$$\begin{aligned}
\mathbf{P}(\mathbf{r}) &= \rho(\mathbf{r}) \, k_{\mathrm{B}} \, T \, \mathbf{I} - \frac{1}{2} \int \frac{\mathbf{ss}}{s} u'(s) \, g^{(2)}(s) \, \rho(\mathbf{r}) \, \rho(\mathbf{r}) \, d\mathbf{s} \\
&\quad - \frac{1}{4} \int \frac{\mathbf{ss}}{s} u'(s) \, g^{(2)}(s) \, \rho(\mathbf{r}) \, \mathbf{ss} : \nabla \nabla \rho(\mathbf{r}) \, d\mathbf{s} \,,
\end{aligned} \tag{A.6}$$

where $g^{(2)}(s) = g^{(2)}(s, \rho_{\mathrm{avg}})$.

The homogeneous pressure can be defined as [6]

$$P^0(\mathbf{r}) = \rho(\mathbf{r}) \, k_{\mathrm{B}} \, T - \frac{1}{6} \, [\rho(\mathbf{r})]^2 \int s \, u'(s) \, g^{(2)}(s) \, d\mathbf{s} \,. \tag{A.7}$$

For $m = 2$, one can simplify the integral in Eq. A.5 to [34]

$$\mathbf{T}_2 = \frac{1}{3} \left[\int s^2 \, f(s) \, d\mathbf{s} \right] \mathbf{I} \,. \tag{A.8}$$

Eqs. A.8 and A.7 show that the first two terms in Eq. A.6 are equal to $P^0(\mathbf{r})\,\mathbf{I}$. Davis also showed the identity [34]

$$\mathbf{T}_4 : \mathbf{ab} = \tfrac{1}{15} \int s^4\, f(s)\, d\mathbf{s}\, [\mathbf{ab} + \mathbf{ba} + (\mathbf{a} \cdot \mathbf{b})\mathbf{I}] \, , \tag{A.9}$$

where $\mathbf{a}$ and $\mathbf{b}$ are arbitrary vectors. Combining Eqs. A.6, A.7, and A.9 yields

$$\mathbf{P}(\mathbf{r}) = P^0(\mathbf{r})\,\mathbf{I} + 2k\left[-\tfrac{1}{2}\rho(\mathbf{r})\,\nabla\nabla\rho(\mathbf{r}) - \tfrac{1}{4}\rho(\mathbf{r})\,\nabla^2\rho(\mathbf{r})\,\mathbf{I} \right] \, . \tag{A.10}$$

For our system, Eq. A.10 reduces to

$$P_{\mathrm{N}}(z) = P^0(z) + k\left[-\tfrac{3}{2}\rho''(z)\,\rho(z) \right] \, , \tag{A.11}$$

and

$$P_{\mathrm{T}}(z) = P^0(z) + \tfrac{1}{3}k\left[-\tfrac{3}{2}\rho''(z)\,\rho(z) \right] \, . \tag{A.12}$$

Combining Eqs. A.11 and A.12 and rearranging gives Eq. 3.23, showing that the H contour can be used in the CPP method to compute the homogeneous pressure and chemical potential.

Appendix B

Gradient expansion of the internal energy density using the IK contour

Here we expand the local internal energy density in terms of density gradient using the IK contour. We follow and adapt the method used for expanding the pressure tensor given by Davis in Ref. [34]. One can write an expression for the local internal energy density using the IK contour as:

$$\phi^{\text{tot}}(\mathbf{r}) = \phi^{\text{ig}}(\mathbf{r}) + \tfrac{1}{2} \int \int_0^1 u(s)\, \rho^{(2)}(\mathbf{r} - \eta\,\mathbf{s}, \mathbf{r} - \eta\,\mathbf{s} + \mathbf{s})\, d\eta\, d\mathbf{s}\,, \tag{B.1}$$

where $\phi^{\text{ig}}(\mathbf{r})$ is the ideal gas internal energy density. For a monatomic fluid, $\phi^{\text{ig}}(\mathbf{r}) = \tfrac{3}{2}\, \rho(\mathbf{r})\, k_{\text{B}}\, T$.

As shown by Davis, one can expand $\rho^{(2)}$ in Eq. B.1 as [34]

$$\rho^{(2)}(\mathbf{r} - \eta\,\mathbf{s}, \mathbf{r} - \eta\,\mathbf{s} + \mathbf{s}) = \sum_{i=0}^{\infty} \frac{(-\eta\mathbf{s} \cdot \nabla)^i}{i!} \rho^{(2)}(\mathbf{r}, \mathbf{r} + \mathbf{s})\,. \tag{B.2}$$

Combining Eqs. B.1 and B.2 and integrating over η gives [34]

$$\phi^{\text{tot}}(\mathbf{r}) = \phi^{\text{ig}}(\mathbf{r}) + \tfrac{1}{2} \int u(s) \sum_{i=0}^{\infty} \frac{(-\mathbf{s} \cdot \nabla)^i}{(i+1)!} \rho^{(2)}(\mathbf{r}, \mathbf{r} + \mathbf{s})\, d\mathbf{s}\,. \tag{B.3}$$

Combining Eqs. A.2, A.3, and B.3 gives

$$\phi^{\text{tot}}(\mathbf{r}) = \phi^{\text{ig}}(\mathbf{r}) + \tfrac{1}{2} \int u(s) \sum_{i=0}^{\infty} \frac{(-\mathbf{s} \cdot \nabla)^i}{(i+1)!} \left[g^{(2)}(\mathbf{r}, \mathbf{r} + \mathbf{s})\, \rho(\mathbf{r}) \sum_{i=0}^{\infty} \frac{(\mathbf{s} \cdot \nabla)^i}{i!} \rho(\mathbf{r}) \right] d\mathbf{s}\,. \tag{B.4}$$

Using a method similar to that given in Appendix A gives to second-order in density gradient:

$$
\begin{aligned}
\phi^{\text{tot}}(\mathbf{r}) \;=\; & \phi^{\text{ig}}(\mathbf{r}) + \tfrac{1}{2}\int u(s)\,g^{(2)}(s)\,\rho(\mathbf{r})\,\rho(\mathbf{r})\,d\mathbf{s} \\
& + \tfrac{1}{4}\int u(s)\,g^{(2)}(s)\,\rho(\mathbf{r})\,\mathbf{ss} : \nabla\nabla\rho(\mathbf{r})\,d\mathbf{s} \\
& - \tfrac{1}{4}\int u(s)\,g^{(2)}(s)\,\mathbf{s}\cdot\nabla\left\{\rho(\mathbf{r})\left[\mathbf{s}\cdot\nabla\rho(\mathbf{r})\right]\right\}\,d\mathbf{s} \\
& + \tfrac{1}{12}\int u(s)\,g^{(2)}(s)\,\mathbf{ss} : \nabla\nabla\left[\rho(\mathbf{r})\right]^2\,d\mathbf{s}\,,
\end{aligned}
\tag{B.5}
$$

where $g^{(2)}(s) = g^{(2)}(s,\rho_{\text{avg}})$.

The homogeneous internal energy density can be defined as [6]

$$
\phi^{0}(\mathbf{r}) = \phi^{\text{ig}}(\mathbf{r}) + \tfrac{1}{2}\left[\rho(\mathbf{r})\right]^2\int u(s)\,g^{(2)}(s)\,d\mathbf{s}\,.
\tag{B.6}
$$

Eq. A.8 shows that the first two terms in Eq. B.5 are equal to the homogeneous internal energy density given in Eq. B.6.

Using Eq. A.8, one can also show

$$
\mathbf{T}_2 : \mathbf{ab} = \tfrac{1}{3}\int s^2\,f(s)\,d\mathbf{s}\,(\mathbf{a}\cdot\mathbf{b})\,,
\tag{B.7}
$$

where $\mathbf{a}$ and $\mathbf{b}$ are arbitrary vectors.

Using Eqs. B.6 and B.7, one can simplify Eq. B.5 to

$$
\phi^{\text{tot}}(\mathbf{r}) = \phi^{0}(\mathbf{r}) + \tfrac{1}{3}k'\left[\tfrac{1}{2}\left[\nabla\rho(\mathbf{r})\right]^2 - \rho(\mathbf{r})\,\nabla^2\rho(\mathbf{r})\right]\,,
\tag{B.8}
$$

where

$$
k' = -\tfrac{1}{6}\int s^2\,u(s)\,g^{(2)}(s,\rho_{\text{avg}})\,d\mathbf{s}\,.
\tag{B.9}
$$

For our system,

$$\phi^{\text{tot}}(z) = \phi^0(z) + \tfrac{1}{3}k' \left[\tfrac{1}{2}\rho'(z)^2 - \rho''(z)\,\rho(z)\right] . \tag{B.10}$$

If we approximate $g^{(2)}(s)$ as 0 when $s < \sigma$ and as 1 when $s > \sigma$, then integration by parts of Eq. 3.22 yields Eq. B.9, or $k = k'$ [34]. Assuming that $k = k'$, combining Eqs. 3.21 and B.10 gives

$$\phi^0(z) = \phi^{\text{tot}}(z) + P^0(z) - P_{\text{T}}(z) . \tag{B.11}$$

Using the approximation for P^0 given in Eq. 3.23 gives

$$\phi^0(z) = \phi^{\text{tot}}(z) - \tfrac{1}{2}\left[P_{\text{N}}(z) - P_{\text{T}}(z)\right] . \tag{B.12}$$

The same relationship holds for the H contour.

Appendix C

Gradient expansion of the species pressure tensor

Using the IK contour, a gradient expansion in density gradients [34] predicts that

$$P_{\mathrm{N},i}(z) = P_i^0(z) + \sum_j c_{ij} \left[\frac{1}{2} \frac{d\rho_i}{dz} \frac{d\rho_j}{dz} - \frac{1}{2} \rho_i \frac{d^2\rho_j}{dz^2} - \frac{1}{2} \rho_j \frac{d^2\rho_i}{dz^2} \right], \tag{C.1}$$

and

$$P_{\mathrm{T},i}(z) = P_i^0(z) + \sum_j c_{ij} \left[\frac{1}{6} \frac{d\rho_i}{dz} \frac{d\rho_j}{dz} - \frac{1}{6} \rho_i \frac{d^2\rho_j}{dz^2} - \frac{1}{6} \rho_j \frac{d^2\rho_i}{dz^2} \right]. \tag{C.2}$$

Combining Eqs. C.1 and C.2 and solving for the homogeneous pressure gives an expression similar to Eq. 3.23:

$$P_i^0(z) = \frac{3}{2} P_{\mathrm{T},i}(z) - \frac{1}{2} P_{\mathrm{N},i}(z). \tag{C.3}$$

Appendix D

Sample LAMMPS input scripts

D.1 Initial configuration for the LJ fluid

The following is a sample input script used to generate initial configurations of the LJ fluid in LAMMPS.

variable   NM equal 32000 #Total number of molecules (must be multiple of 1000)

variable   SC equal 32 #Aspect ratio of the simulation cell

variable   NTS equal 2000 #Total number of timesteps

variable   TSET equal 1.312 #System temperature

variable   RCUT equal 6.0 #Cut-off radius

variable   yy equal (${NM}/${SC})^(1/3)

variable   zz equal ${yy}

variable   xx equal ${yy}*${SC}

units   lj

atom_style atomic

lattice   sc 0.4

region   box block 0 ${xx} 0 ${yy} 0 ${zz}

create_box 1 box

create_atoms 1 box

mass   1 1.0

velocity   all create ${TSET} 87287 rot yes dist gaussian

```
pair_style   lj/cut ${RCUT}

pair_coeff   1 1 1.0 1.0 ${RCUT}

neighbor     0.3 bin

neigh_modify every 20 delay 0 check no

fix          1 all nvt temp ${TSET} ${TSET} 10.0

restart      1000 file configXYZQ

thermo       1000

run          ${NTS}
```

D.2   CPP method

The following is a sample input script used to implement the CPP method for the LJ fluid in LAMMPS.

```
variable   NM equal 32000 #Total number of molecules (must be multiple of 1000)

variable   SC equal 32 #Aspect ratio of the simulation cell

variable   NTS equal 10000000 #Total number of timesteps

variable   NBLK equal 1 #Total number of blocks

variable   NJNK equal 100000 #Number of timesteps to discard at beginning of simulation

variable   Nevery equal 50 #Number of time-steps between property samples

variable   Nrepeat equal ${NTS}/${Nevery}/${NBLK} #Number of timesteps between
           property samples

variable   Nfreq equal ${NTS}/${NBLK} variable TSET equal 1.312 #System temperature

variable   RCUT equal 6.0 #Cut-off radius

variable   NBIN equal 400 #Number of bins in the x direction

variable   EL equal ly #Length of the simulation cell in the y and z directions

variable   AF equal 0.25 #Strength of external field

variable   dx equal 1/${NBIN} #Bin size
```

```
variable    forcex atom 2*PI*${AF}*sin(2*PI*x/lx)/lx

units       lj

atom_style  atomic

read_restart  configXYZQ

reset_timestep  0

pair_style   lj/cut ${RCUT}

pair_coeff   1 1 1.0 1.0 ${RCUT}

neighbor     0.3 bin

neigh_modify  every 20 delay 0 check no

fix          1 all nvt temp ${TSET} ${TSET} 10.0

fix          4 all addforce v_forcex 0.0 0.0 #Apply external potential

fix          dim all print 1 "${EL} ${TSET} ${SC} ${RCUT}" screen no file dim.txt

fix          fext all print 1 "${AF}" screen no file fext.txt

run          1

unfix        dim

unfix        fext

run          ${NJNK} reset_timestep 0

compute      atomstress all stress/atom

compute      atompe all pe/atom

compute      atomke all ke/atom

fix          2 all ave/spatial ${Nevery} ${Nrepeat} ${Nfreq} x center ${dx} density/number
             units reduced file denhist.txt #Density profile

fix          3 all ave/spatial ${Nevery} ${Nrepeat} ${Nfreq} x center ${dx} c_atomstress[1]
             c_atomstress[2] c_atomstress[3] c_atomke c_atompe units reduced file stnsn.txt
             #Pressure tensor profile

restart      1000 file configXYZQ

thermo       1000

run          ${NTS}
```